

1 MEASUREMENT OF ELECTROWEAK PRODUCTION OF
2 SAME-SIGN W BOSON PAIRS WITH ATLAS (WORKING
3 TITLE)

4 William Kennedy DiClemente

8 Presented to the Faculties of The University of Pennsylvania
9 in Partial Fulfillment of the Requirements for the Degree of Doctor of Philosophy
10 2019 Last compiled: January 31, 2019

¹¹
¹² I. Joseph Kroll, Professor, Physics
¹³ Supervisor of Dissertation

23 MEASUREMENT OF ELECTROWEAK PRODUCTION OF SAME-SIGN W BOSON PAIRS
24 WITH ATLAS (WORKING TITLE)

25 COPYRIGHT
26 2019
27 William Kennedy DiClemente

28 All rights reserved.

Acknowledgements

³⁰ I'd like to thanks the Ghosts of Penn Students Past for providing me with such an amazing thesis
³¹ template.

32

ABSTRACT

33 MEASUREMENT OF ELECTROWEAK PRODUCTION OF SAME-SIGN W BOSON PAIRS
34 WITH ATLAS (WORKING TITLE)

35

William Kennedy DiClemente

36

J. Kroll

37

This is the abstract text.

Contents

39	Acknowledgements	iii
40	Abstract	iv
41	Contents	v
42	List of Tables	ix
43	List of Figures	xii
44	Preface	xviii
45	1 Introduction	1
46	2 Theoretical Framework	2
47	2.1 Introduction to the Standard Model	2
48	2.2 Electroweak symmetry breaking and the Higgs boson	4
49	2.3 Diboson physics	7
50	3 LHC and the ATLAS Detector	8
51	3.1 The Large Hadron Collider	8
52	3.2 The ATLAS Detector	8
53	3.2.1 The Inner Detector	8
54	3.2.1.1 Pixel Detector	8
55	3.2.1.2 Semiconductor Tracker	8
56	3.2.1.3 Transition Radiation Tracker	8

57	3.2.2	The Calorimeters	9
58	3.2.2.1	Liquid Argon Calorimeters	9
59	3.2.2.2	Tile Calorimeters	9
60	3.2.3	The Muon Spectrometer	9
61	3.2.4	Particle reconstruction	10
62	3.2.4.1	Track reconstruction	10
63	3.2.4.2	Muon reconstruction	10
64	3.2.4.3	Electron reconstruction	10
65	3.2.4.4	Jet reconstruction	10
66	4	Alignment of the ATLAS Inner Detector	11
67	4.1	The alignment method	12
68	4.1.1	Alignment levels	15
69	4.1.2	Alignment coordinate systems	16
70	4.2	Early 2015 alignment of the ATLAS detector	18
71	4.2.1	June alignment procedure	19
72	4.2.2	Alignment results	20
73	4.2.2.1	Residual distributions from collisions	21
74	4.2.2.2	Track parameter resolution from cosmic rays	23
75	4.2.3	Error scaling	24
76	4.3	Level 2 alignment of the TRT	27
77	4.4	Momentum bias from sagitta deformations	28
78	4.4.1	Sagitta bias monitoring with electron E/p	30
79	4.4.1.1	Measuring $\langle E/p \rangle$	31
80	4.4.1.2	Results in 13 TeV data	33
81	5	Measurement of same-sign WW production at $\sqrt{s} = 13$ TeV with ATLAS	36
82	5.0.2	Theoretical overview of vector boson scattering	36
83	5.0.3	Same-sign $W^\pm W^\pm$ scattering	38
84	5.0.4	Overview of backgrounds	40
85	5.1	Data and Monte Carlo samples	42
86	5.1.1	Monte Carlo samples	42
87	5.2	Object and event selection	43

88	5.2.1 Object selection	43
89	5.2.1.1 Muon candidate selection	44
90	5.2.1.2 Electron candidate selection	46
91	5.2.1.3 Jet candidate selection	46
92	5.2.1.4 Treatment of overlapping objects	46
93	5.2.2 Signal event selection	48
94	5.3 Background estimations	50
95	5.3.1 Estimation of the WZ background	50
96	5.3.2 Estimation of the $V\gamma$ background	51
97	5.3.3 Estimation of backgrounds from charge misidentification	53
98	5.3.3.1 Validation of the charge misidentification estimate	56
99	5.3.4 Estimation of non-prompt backgrounds with the fake factor method	57
100	5.3.4.1 Overview of the default fake factor method	57
101	5.3.4.2 The fake factor with p_T^{cone}	58
102	5.3.4.3 Application of the fake factor	60
103	5.3.4.4 Systematic uncertainties	65
104	5.3.4.5 Results of the fake factor	65
105	5.3.4.6 Validation of the fake factor	67
106	5.3.5 Reduction of WZ background using custom overlap removal	70
107	5.4 Cross section measurement	73
108	5.4.1 Maximum likelihood fit	74
109	5.4.2 Definition of the fiducial volume	76
110	5.4.3 Cross section extraction	77
111	5.5 Summary of uncertainties	78
112	5.5.1 Experimental uncertainties	79
113	5.5.2 Theoretical uncertainties	80
114	5.5.2.1 Uncertainties from EWK-QCD interference	80
115	5.6 Results	81
116	6 Prospects for same-sign WW at the High Luminosity LHC	86
117	6.0.1 Analysis Overview	87
118	6.1 Theoretical motivation	87
119	6.1.1 Experimental sensitivity to longitudinal polarization	88

120	6.2 Monte Carlo samples	88
121	6.3 Background estimations	90
122	6.3.1 Truth-based isolation	91
123	6.4 Object and event selection	92
124	6.4.1 Object selection	92
125	6.4.2 Event selection	92
126	6.5 Selection optimization	93
127	6.5.1 Random grid search algorithm	93
128	6.5.2 Inputs to the optimization	95
129	6.5.3 Results of the optimization	96
130	6.6 Results	97
131	6.6.1 Event yields	97
132	6.6.2 Uncertainties	103
133	6.6.3 Cross section measurement	103
134	6.6.4 Longitudinal scattering significance	104
135	7 Conclusion	108
136	A Additional material on truth isolation	109
137	B Additional material on $W^\pm W^\pm jj$ measurement at $\sqrt{s} = 13\text{TeV}$	110
138	B.1 Impact of experimental uncertainty on MC background estimations	110
139	Bibliography	112

List of Tables

141	4.1	The four alignment levels for each of the detector subsystems. The total number of alignable structures and degrees of freedom (DoF) to be aligned are given for each level.	17
143	4.2	Summary of the highest level of alignment applied to each ID subsystem when deriving the June alignment.	20
145	4.3	Estimated value of the error scaling term b for each subdetector component with the June alignment.	27
147	5.1	Predicted cross sections for EQK and QCD production of diboson processes relevant to VBS at $\sqrt{s} = 8\text{TeV}$ using the SHERPA MC generator. Loose generator level cuts are applied on lepton $p_T > 5\text{ GeV}$, dilepton invariant mass $m_{ll} > 4\text{ GeV}$, and at least two jets with $m_{jj} > 10\text{ GeV}$	39
151	5.2	Summary of MC samples used in the analysis.	44
152	5.3	Muon selection criteria. All muons are required to pass the preselection (top), and then either the signal (middle) or loose (bottom) criteria is applied to the preselected electrons.	45
154	5.4	Electron selection criteria. All electrons are required to pass the preselection (top), and then either the signal (middle) or loose (bottom) criteria is applied to the preselected electrons.	47
157	5.5	Jet selection criteria. All jets are required to pass the above selection in order to be used in the analysis.	47
159	5.6	Summary of the overlap removal procedure used in the analysis. If the criteria in the “check” column is met, in the “result” column, the object on the left of the arrow is removed in favor of the object on the right.	48
162	5.7	Summary of trigger requirements for electrons and muons for $\sqrt{s} = 13\text{TeV}$ data collected in 2015 and 2016. At least one of the triggers must be satisfied.	49
164	5.8	The signal event selection.	50
165	5.9	Event yields in the WZ control region before normalization. All lepton flavor channels are combined.	51
167	5.10	Selection criteria for the $V\gamma$ control region.	52
168	5.11	Event yields in the $V\gamma$ control region. The $V\gamma$ scale factor of 1.77 is calculated by scaling up the $Z\gamma$ and $Z+\text{jets}$ backgrounds to account for the difference between the data and predicted total background.	53
171	5.12	Selection criteria for the same-sign inclusive validation region.	56

172	5.13 Event selection for the dijet region used for calculating the fake factor. The selected lepton can pass either the nominal (signal) or loose selections. In the case of the nominal leptons, the $p_T > 27$ GeV requirement is replaced with $p_T > 15$ GeV.	62
173		66
174		
175	5.14 Values of the fake factor in each p_T bin and for each individual systematic source.	66
176		
177	5.15 Estimated yields for the fake lepton background. The estimated yield is shown in the first column together with the statistical uncertainty followed by the systematic uncertainties from variations of the the fake factors within their statistical (stat.) and systematic (syst.) uncertainties. The labels f_e and f_μ indicate the fake factors for electrons and muons, respectively.	66
178		
179		
180		
181	5.16 Selection criteria for the same-sign top fakes validation region.	67
182		
183	5.17 Custom OR definition. Leptons must pass this selection in order to be counted for the trilepton veto.	73
184		
185	5.18 Definition of the fiducial volume.	76
186		
187	5.19 Impact of various systematic effects on the fiducial cross section measurement. The impact of a given source of uncertainty is computed by performing the fit with the corresponding nuisance parameter varied up or down by one standard deviation from its nominal value.	78
188		
189	5.20 List of sources of experimental uncertainties on the reconstruction of physics objects.	79
190		
191	5.21 Impact of experimental uncertainties for the $W^\pm W^\pm jj$ EWK processes in all channels.	80
192		
193	5.22 Impact of experimental uncertainties for the WZ process in all channels.	80
194		
195	5.23 The set of generator level cuts used for generating the interference samples with <code>MadGraph</code>	81
196		
197	5.24 Cross sections for each different $W^\pm W^\pm jj$ production mode (inclusive, EWK only, QCD only, and interference only) generated using <code>MadGraph</code> . The cross sections are calculated using a minimal set of generator level cuts from events where the W decays to a muon.	81
198		
199		
200		
201		
202	5.25 Table of the data and prediction event yields in the signal region before the fit. Numbers are shown for the six lepton flavor and charge channels and for all channels combined. Here the WZ background yields are normalized to the data in the WZ control region. The background estimations from the fake factor are included in the “Non-prompt” category, and backgrounds from $V\gamma$ production and electron charge misidentification are combined in the “ e/γ conversions” category. Finally, ZZ , VVV , and $t\bar{t}V$ backgrounds are combined in the “Other prompt” category.	82
203		
204		
205		
206		
207		
208		
209	5.26 Table of the data and prediction event yields in the signal region after the fit. Numbers are shown for the six lepton flavor and charge channels and for all channels combined. The background estimations from the fake factor are included in the “Non-prompt” category, and backgrounds from $V\gamma$ production and electron charge misidentification are combined in the “ e/γ conversions” category. Finally, ZZ , VVV , and $t\bar{t}V$ backgrounds are combined in the “Other prompt” category.	83
210		
211		
212		
213		
214	6.1 Summary of MC samples used in the analysis.	90
215		
216	6.2 Truth-based isolation requirements for electrons and muons.	91
217		
218	6.3 Summary of the signal event selection.	93
219		
220	6.4 Updates to the $W^\pm W^\pm jj$ event selection criteria after optimization. Cuts not listed remain unchanged from the default selection in Table 6.3.	97
221		
222	6.5 Signal and background event yields using the default event selection for an integrated luminosity of $\mathcal{L} = 3000 \text{ fb}^{-1}$. Events containing a fake or charge-flipped electron are removed from their respective sources and combined into a single entry each.	101
223		
224	6.6 Signal and background event yields using the optimized event selection for an integrated luminosity of $\mathcal{L} = 3000 \text{ fb}^{-1}$. Events containing a fake or charge-flipped electron are removed from their respective sources and combined into a single entry each.	101
225		

220	6.7 Summary of estimated experimental and rate uncertainties.	103
221	A.1 Event yields prior to applying any form of truth-based isolation criteria.	109
222	A.2 Event yields after applying a test version of the truth-based isolation.	109
223	B.1 Experimental systematics uncertainties for the $W^\pm W^\pm jj$ QCD processes in all channels.	110
224	B.2 Experimental systematics uncertainties for triboson process in all channels.	110
225	B.3 Experimental systematics uncertainties for $t\bar{t}V$ processes in all channels.	111
226	B.4 Experimental systematics uncertainties for the $W\gamma$ process in all channels.	111
227	B.5 Experimental systematics uncertainties for the $Z\gamma$ process in all channels.	111
228	B.6 Experimental systematics uncertainties for the ZZ process in all channels.	111

List of Figures

230 2.1	An illustration of the potential term $V(\phi)$ in the cases where $\mu^2 > 0$ (left) and $\mu^2 < 0$ (right). The right-hand plot shows the Higgs potential, or ‘‘Mexican hat potential’’, with the minimum at $ \phi = \sqrt{-\frac{\mu^2}{\lambda}}$ rather than at $ \phi = 0$ as in the left-hand plot.	5
233 3.1	General cut-away view of the ATLAS detector.	9
234 4.1	Graphical representation of the effect of a misaligned detector element. The reconstructed particle track (dashed arrow) differs from the actual trajectory of the particle (solid arrow) due to the shift in one of the detector elements. The cyan lines represent the track-to-hit residuals.	12
238 4.2	Graphical representation of the ID alignment chain.	15
239 4.3	A schematic representation of the Inner Detector in the longitudinal plane with the global coordinate system overlaid on top. The Pixel detector and IBL are shown in blue, the SCT in green, and the TRT in red. The local coordinates for each subdetector module are inset on the right.	18
243 4.4	The d_0 distributions with respect to the reconstructed primary vertex using the $\sqrt{s} = 13\text{TeV}$ collision data sample reconstructed using the June (black) and March (green) alignments. The data is compared to a MC simulation using a perfect detector geometry (red). The distributions are normalized to the same number of entries.	21
247 4.5	Local x (left) and local y (right) residual distributions of the IBL planar sensors using the $\sqrt{s} = 13\text{TeV}$ collision data sample reconstructed using the June (black) and March (green) alignments. The data is compared to a MC simulation using a perfect detector geometry (red). The distributions are normalized to the same number of entries.	22
251 4.6	The mean of the local x (left) and local y (right) residual distributions as a function of the global z position of each IBL module using the $\sqrt{s} = 13\text{TeV}$ collision data sample reconstructed using the June (black) and March (green) alignments. The data is compared to a MC simulation using a perfect detector geometry (red).	23
255 4.7	Local x (top) and local y (bottom) residual distributions for the Pixel barrel (excluding the IBL, left) and end-caps (right) using the $\sqrt{s} = 13\text{TeV}$ collision data sample reconstructed using the June (black) and March (green) alignments. The data is compared to a MC simulation using a perfect detector geometry (red). The distributions are normalized to the same number of entries.	24

260	4.8	Local x residual distributions for the SCT barrel (left) and end-caps (right) using the $\sqrt{s} = 13\text{TeV}$ collision data sample reconstructed using the June (black) and March (green) alignments. The data is compared to a MC simulation using a perfect detector geometry (red). The distributions are normalized to the same number of entries.	25
264	4.9	Residual distributions for the TRT barrel (left) and end-caps (right) using the $\sqrt{s} = 13\text{TeV}$ collision data sample reconstructed using the June (black) and March (green) alignments. The data is compared to a MC simulation using a perfect detector geometry (red). The distributions are normalized to the same number of entries.	25
268	4.10	Representation of splitting a single cosmic ray track passing through the entire detector (left) into two separate tracks (right).	26
270	4.11	Distribution of the difference in the impact parameter Δd_0 (left) and charge over transverse momentum $\Delta q/p_T$ (right) between the two cosmic ray split tracks. The June (black) and March (green) alignments are compared. The distributions are normalized to the same number of entries.	26
274	4.12	Pull distributions in local x (left) and y (right) for the IBL using the $\sqrt{s} = 13\text{TeV}$ collision data sample after applying the error scaling.	27
276	4.13	Residual means by straw layer in two TRT ϕ -sectors affected by a tilt misalignment. The tilts in each of the three modules are clearly visible in the red points representing the reconstructed data prior to alignment. After four iterations of L2 alignment, the residual means in the gray points are flat.	28
280	4.14	Two dimensional map of residuals in the first layer of the TRT barrel vs z and ϕ . Each bin represents the mean of a Gaussian fit to the TRT residuals in that bin. The map on the left is after the L3 (wire-by-wire) alignment of the TRT performed in 2010, and the map on the right is after the L2 alignment at the end of 2015. The z -axis for both plots use the same scale.	29
285	4.15	Representation of a curl distortion in the detector. The image shows a cutaway in the transverse plane. The deformation is represented by the red arrows, and the impact on the reconstructed positive (blue) and negative (green) tracks are shown. The dashed lines represent the true particle trajectories, and the solid lines represent the reconstructed trajectories.	30
290	4.16	Geometric definition of the sagitta s in relation to the length of the chord l and the radius r of a circular arc.	30
292	4.17	E/p distributions of electrons and positrons in two different $\eta\phi$ bins of the detector. The left hand plot is taken from a region with no momentum bias where $\langle E/p \rangle^+ = \langle E/p \rangle^-$, while the right hand plot shows an 8% disagreement in $\langle E/p \rangle$ between electrons and positrons.	32
296	4.18	Sagitta bias in the $\sqrt{s} = 13\text{TeV}$ data collected by ATLAS in 2016 as a function of η and ϕ for the prompt (left) and reprocessed (right) alignments using the E/p method.	34
298	4.19	Sagitta bias in the $\sqrt{s} = 13\text{TeV}$ data collected by ATLAS in 2016 projected along η for the prompt (gray) and reprocessed (blue) alignments using the E/p method.	34
300	4.20	Sagitta bias in the $\sqrt{s} = 13\text{TeV}$ data collected by ATLAS in 2017 as a function of η and ϕ in reconstructed electrons (left) and after two iterations of momentum corrections (right) from the E/p method.	34
303	4.21	Sagitta bias in the $\sqrt{s} = 13\text{TeV}$ data collected by ATLAS in 2017 projected along η in reconstructed electrons (gray) and after one (red) and two (blue) iterations of momentum corrections from the E/p method.	35

306	5.1	Cross sections in nanobarns for five different scattering processes of longitudinally polarized vector bosons as a function of center of mass energy \sqrt{s} . Without a SM Higgs boson (left), the cross sections grow unbounded with \sqrt{s} ; however with a 120 GeV Higgs boson (right), the cross sections no longer diverge.	37
310	5.2	Tree-level Feynman diagrams for VBS EWK $VVjj$ production including triple gauge couplings involving W and/or Z bosons (top left and top middle), quartic gauge coupling (top right), or the exchange of a Higgs boson (s -channel bottom left and t -channel bottom right). The labels are quarks (q), fermions (f), and gauge bosons ($V = W, Z$).	38
314	5.3	Tree-level Feynman diagrams for non-VBS EWK $VVjj$ production. The labels are quarks (q), fermions (f), and gauge bosons ($V = W, Z$).	38
316	5.4	Tree-level Feynman diagrams for QCD $VVjj$ production. The labels are quarks (q), fermions (f), and gauge bosons ($V = W, Z$).	39
318	5.5	Feynman diagrams for VBS EWK production of $W^\pm W^\pm jj$ events. The leftmost diagram contains a quartic gauge coupling vertex, and the rightmost diagram contains an exchange of a Higgs boson. TODO: Make diagrams consistent with others	40
321	5.6	$W^\pm W^\pm jj$ VBS event topology containing two leptons (1 and 2) with the same electric charge, two neutrinos, and two forward tagging jets (3 and 4) with large rapidity separation Δy	40
324	5.7	Generator level comparisons at $\sqrt{s} = 8\text{TeV}$ of dijet invariant mass (m_{jj} , left) and dijet rapidity (Δy_{jj} , right) in EWK (red) and QCD (blue) $W^\pm W^\pm jj$ events. Both data sets have been normalized to the same area.	41
327	5.8	ATLAS event display of a $pp \rightarrow W^+W^+ \rightarrow \mu^+\nu_\mu\mu^+\nu_\mu jj$ event. The muons are represented by the red lines travelling from the ID through the MS, and the forward jets are represented by the blue cones with yellow energy deposits in the calorimeters. The direction of the E_T^{miss} in the transverse plane is indicated by the gray dashed line in the inset image.	41
332	5.9	Leading lepton p_T (left) and η (right) distributions in the WZ control region before normalization. All lepton channels are combined.	52
334	5.10	Trilepton invariant mass m_{lll} distribution in the WZ control region before normalization. All lepton channels are combined.	52
336	5.11	Charge misidentification rates for electrons as a function of $ \eta $ and p_T . Rates are calculated from $Z \rightarrow e^+e^-$ MC after applying scale factors to approximate the charge mis-ID rates in data.	54
339	5.12	Dilepton invariant mass distribution m_{ll} for the ee channel in the same-sign inclusive VR.	56
340	5.13	p_T distributions for the leading (left) and subleading (right) electron for the ee channel in the same-sign inclusive VR. In these plots, the cut requiring m_{ee} to fall within the Z mass window has been inverted in order to test the modelling away from the Z peak.	57
343	5.14	Δp_T distributions for nominal (blue) and loose (red) muons in simulated $t\bar{t}$ events. Each muon has been matched to a truth-level jet. Both distributions are normalized to unit area.	59
346	5.15	Δp_T distributions for muons (top) and electrons (bottom) in simulated $t\bar{t}$ events. Each lepton has been matched to a truth-level jet, and that truth jet has had its p_T corrected to include all truth muons within a cone of $\Delta R < 0.4$. The nominal leptons are in black. Δp_T is calculated for the loose leptons using p_T (red) and $p_T + p_T^{\text{cone}}$ (blue).	61
350	5.16	Distributions of p_T^{cone}/p_T for nominal (black) and loose (red) muons in simulated $t\bar{t}$ events.	62
351	5.17	The measured fake factor as a function of muon $p_T + p_T^{\text{cone}}$. The error bars represent the statistical uncertainty only.	63

353	5.18	The measured fake factor as a function of electron $p_T + p_T^{\text{cone}}$ in the central ($ \eta < 1.37$, blue) and forward ($ \eta > 1.37$, red) regions of the detector. The error bars represent the statistical uncertainty only.	63
356	5.19	Graphical representation of the fake factor application using $p_T + p_T^{\text{cone}}$. The value of $p_T + p_T^{\text{cone}}$ for the loose lepton is used to “look up” the fake factor weight which is then applied to the event. The loose lepton’s p_T becomes $p_T + p_T^{\text{cone}}$ for the purpose of the fake background estimation.	64
360	5.20	Systematic variations in the fake factor as a function of muon $p_T + p_T^{\text{cone}}$. The individual fake factors obtained for each systematic variation are displayed with their statistical uncertainties.	67
363	5.21	Systematic variations in the fake factor as a function of electron $p_T + p_T^{\text{cone}}$ in the central ($ \eta < 1.37$, top) and forward ($ \eta > 1.37$, bottom) regions of the detector. The individual fake factors obtained for each systematic variation are displayed with their statistical uncertainties.	68
367	5.22	Distributions of the subleading lepton p_T in the same-sign top fakes VR for $\mu^\pm\mu^\pm$ events (top right), $e^\pm e^\pm$ events (top left), $\mu^\pm e^\pm$ events (bottom left), and all events combined (bottom right). All errors are statistical only.	69
370	5.23	Pseudorapidity (η) distributions of truth muons (top) and electrons (bottom) for Sherpa $W^\pm W^\pm jj$ and WZ MC samples. The blue vertical lines represent the allowed η range for each lepton flavor. The numbers correspond to the number of raw MC events that fall within and outside of the allowed η range for each MC sample.	71
374	5.24	Distributions of $p_{T,\text{ratio}}(\mu, j)$ for EWK and QCD $W^\pm W^\pm jj$ signal (black) and WZ background (teal) for truth-matched third muons in events that pass the trilepton veto. Both distributions are normalized to unit area. The associated efficiency curves are on the right where efficiency is defined as the percentage of total events that would pass a cut on $p_{T,\text{ratio}}(\mu, j)$ at a given value on the x -axis.	71
379	5.25	Distributions of $\Delta R(\mu, j)$ for EWK and QCD $W^\pm W^\pm jj$ signal (black) and WZ background (teal) for truth-matched third muons in events that pass the trilepton veto. Both distributions are normalized to unit area. The associated efficiency curves are on the right where efficiency is defined as the percentage of total events that would pass a cut on $\Delta R(\mu, j)$ at a given value on the x -axis.	72
384	5.26	Distributions of $p_{T,\text{ratio}}(e, j)$ for EWK and QCD $W^\pm W^\pm jj$ signal (black) and WZ background (teal) for truth-matched third electrons in events that pass the trilepton veto. Both distributions are normalized to unit area. The associated efficiency curves are on the right where efficiency is defined as the percentage of total events that would pass a cut on $p_{T,\text{ratio}}(e, j)$ at a given value on the x -axis.	72
389	5.27	Two-dimensional plots of $p_{T,\text{ratio}}(\mu, j)$ vs $\Delta R(\mu, j)$ for truth-matched third muons in events that pass the trilepton veto for EWK and QCD $W^\pm W^\pm jj$ signal (left) and WZ background (right). The blue overlay indicates the area in which the third leptons will pass the custom OR and result in the event failing the trilepton veto.	73
393	5.28	Visual representation of the different kinematic regions relevant to the cross section measurement. The acceptance factor \mathcal{A} converts from the truth level total phase space to the truth level fiducial region, and the efficiency correction \mathcal{C} translates the fiducial region in to the reconstruction level signal region.	77

397	5.29	The dijet invariant mass m_{jj} distributions for data and predicted signal and background in the signal region after the fit. The shaded band represents the statistical and systematic uncertainties added in quadrature. Note that the bins have been scaled such that they represent the number of events per 100 GeV in m_{jj} . The background estimations from the fake factor are included in the “Non-prompt” category, and backgrounds from $V\gamma$ production and electron charge misidentification are combined in the “ e/γ conversions” category. Finally, ZZ , VVV , and $t\bar{t}V$ backgrounds are combined in the “Other prompt” category.	83
405	5.30	The event yields for data and predicted signal and background in the WZ and low- m_{jj} control regions after the fit. The shaded band represents the statistical and systematic uncertainties added in quadrature. The background estimations from the fake factor are included in the “Non-prompt” category, and backgrounds from $V\gamma$ production and electron charge misidentification are combined in the “ e/γ conversions” category. Finally, ZZ , VVV , and $t\bar{t}V$ backgrounds are combined in the “Other prompt” category.	84
411	5.31	Comparison of the measured $W^\pm W^\pm jj$ EWK fiducial cross section with theoretical calculations from SHERPA v2.2.2 and POWHEG-BOX v2 . The light orange band represents the total experimental uncertainty on the measured value, and the dark orange hashed band is the statistical uncertainty. For the simulations, the light blue band represents the total theoretical uncertainty, and the dark blue hashed band are the scale uncertainties. The theory predictions do not include the interference between the EWK and QCD production.	85
418	6.1	Comparison of the leading (top) and subleading (bottom) lepton p_T distributions for purely longitudinal (LL, black) and mixed polarization (LT+TT, cyan) $W^\pm W^\pm jj$ events.	89
420	6.2	Comparison of the azimuthal dijet separation ($ \Delta\phi_{jj} $) for purely longitudinal (LL, black) and mixed polarization (LT+TT, cyan) $W^\pm W^\pm jj$ events.	90
422	6.3	A visual representation of a rectangular grid search algorithm. The signal events are the blue triangles, and the red circles are the background events. TODO: replace with own figure	94
425	6.4	A visual representation of a random grid search algorithm. The signal events are the blue triangles, and the red circles are the background events. TODO: replace with own figure	95
428	6.5	Leading lepton p_T distribution. The default and optimized cuts are represented by the red and green dashed lines, respectively. The $W^\pm W^\pm jj$ EWK signal (black points) is normalized to the same area as the sum of the backgrounds (colored histogram). TODO: Move to appendix or omit	98
432	6.6	Dilepton invariant mass distribution. The default and optimized cuts are represented by the red and green dashed lines, respectively. The $W^\pm W^\pm jj$ EWK signal (black points) is normalized to the same area as the sum of the backgrounds (colored histogram). TODO: Move to appendix or omit	98
436	6.7	Leading (top) and subleading (bottom) jet p_T distributions. The default and optimized cuts are represented by the red and green dashed lines, respectively. The $W^\pm W^\pm jj$ EWK signal (black points) is normalized to the same area as the sum of the backgrounds (colored histogram).	99
440	6.8	Dijet invariant mass distribution. The default and optimized cuts are represented by the red and green dashed lines, respectively. The $W^\pm W^\pm jj$ EWK signal (black points) is normalized to the same area as the sum of the backgrounds (colored histogram). TODO: Move to appendix or omit	100

444	6.9	Lepton-jet centrality distribution. The default and optimized cuts are represented by the red and green dashed lines, respectively. The $W^\pm W^\pm jj$ EWK signal (black points) is normalized to the same area as the sum of the backgrounds (colored histogram).	100
445	6.10	p_T distributions for the leading jet using the default (left) and optimized (right) event selections for all channels combined.	102
446	6.11	p_T distributions for the subleading jet using the default (left) and optimized (right) event selections for all channels combined.	102
447	6.12	p_T distributions for lepton-jet centrality ζ using the default (left) and optimized (right) event selections for all channels combined.	102
448	6.13	Projections of the statistical (black), theoretical (blue), systematic (yellow), and total (red) uncertainties on the measured cross section as a function of integrated luminosity using the optimized event selection.	104
449	6.14	Dijet azimuthal separation ($ \Delta\phi_{jj} $) for the low m_{jj} region ($520 < m_{jj} < 1100$ GeV, top) and the high m_{jj} region ($m_{jj} > 1100$ GeV, bottom). The purely longitudinal (LL, gray) is plotted separately from the mixed and transverse (LT+TT, cyan) polarizations.	106
450	6.15	Projections of the expected longitudinal scattering significance as a function of integrated luminosity when considering all sources of uncertainties (black) or only statistical uncertainties (red).	107
451			
452			
453			
454			
455			
456			
457			
458			
459			
460			
461			

Preface

463 This is the preface. It's optional, but it's nice to give some context for the reader and stuff.

Will K. DiClemente

Philadelphia, February 2019

465

CHAPTER 1

466

Introduction

467 The Standard Model (SM)¹ has been remarkably successful...

¹Here's a footnote.

CHAPTER 2

Theoretical Framework

470 This chapter outlines the theoretical groundwork for the rest of the thesis. An overview of the Stan-
 471 dard Model of particle physics (SM) is given in Section 2.1, followed by the electroweak symmetry
 472 breaking mechanism involving the Higgs boson in Section 2.2. Finally, Section 2.3 will go into some
 473 detail on the interests of diboson physics specifically.

474 **2.1 Introduction to the Standard Model**

475 The Standard Model of particle physics serves as a mathematical description of the fundamental
 476 particles of the universe and their interactions. It has been developed over the course of the past
 477 century, incorporating both predictions from theory and results from experiments. All in all, the SM
 478 has proven remarkably successful in accurately describing particle interactions seen in experiments.

479 The SM is a quantum field theory (QFT) [1, 2] in which the fundamental particles are represented
 480 as excited states of their corresponding fields. The spin- $\frac{1}{2}$ fermionic fields give rise to the quarks
 481 and leptons comprising ordinary matter, the spin-1 fields correspond to the electroweak bosons and
 482 the gluon which mediate the electroweak and strong forces, respectively, and finally the scalar Higgs
 483 field is responsible for electroweak symmetry breaking. The excitations and interactions of the fields
 484 are governed by the SM Lagrangian, which is invariant under local transformations of the group
 485 $SU(3) \times SU(2) \times U(1)$. **TODO: need more detail/refinement here**

486 The first quantum field theory to be developed is quantum electrodynamics (QED) [3], which
 487 describes the electromagnetic interaction. The theory predicts the existence of a $U(1)$ gauge field
 488 that interacts with the electrically charged fermions. This field corresponds to the photon. A key
 489 aspect of QED is that it is perturbative. The coupling constant $\alpha = e^2/4\pi$ is small, where e is

490 electrical charge of the field, allowing for the use of perturbation theory in calculations. In this case,
 491 calculations can be written as a power series in α , where successive higher order terms contribute
 492 less to the final result. **TODO: renormalizability here?**

493 The strong interaction—the theory of quarks and gluons—has also been described using QFT
 494 as quantum chromodynamics (QCD). The symmetry group for QCD is $SU(3)$, and its eight gen-
 495 erators correspond to the eight differently charged, massless gluons [4]. Unlike in QED, which has
 496 positive and negative charges, the strong force has three “colors”. Color charge combined with the
 497 non-Abelian nature of $SU(3)$, which allows the gluons to interact with each other, result in the
 498 most well-known property of QCD: color confinement. In order to increase the separation between
 499 two color-charged quarks, the amount of energy required increases until it becomes energetically
 500 favorable to pair-produce a new quark-antiquark pair, which then bind to the original quarks. The
 501 end result of this is that only color-neutral objects exist in isolation. What this means for the strong
 502 coupling constant α_s is that its value at the low energies where confinement occurs is large, on
 503 the order of $\alpha_s \sim 1$. The consequence of this is that perturbation theory cannot be used to accu-
 504 rately approximate interactions. While this appears at first to be a critical problem for predictions,
 505 fortunately it turns out that α_s “runs”, or decreases in magnitude at higher energy [5, 6]. This so-
 506 called “asymptotic freedom” allows QCD to be calculated perturbatively [7] at energies accessible
 507 by collider experiments including the LHC.

508 The last gauge field corresponds to the weak interaction. Ultimately, the weak $SU(2)$ and the
 509 electromagnetic $U(1)$ mix to form the $SU(2) \times U(1)$ *electroweak* (EWK) interaction [8, 9]. A more
 510 detailed description of the mixing will be discussed in conjunction with electroweak symmetry break-
 511 ing (EWSB) in Section 2.2; however, a summary of the resulting EWK interaction is presented here,
 512 at the risk of some repeated information to follow. There are three weak isospin bosons arising from
 513 the $SU(2)$ group (W_μ^1 , W_μ^2 , and W_μ^3) and one weak hypercharge boson from the $U(1)$ group (B_μ).
 514 The W_3 and B bosons mix according to the weak mixing angle θ_W to form the Z boson and the
 515 photon according to:

$$\begin{pmatrix} \gamma \\ Z \end{pmatrix} = \begin{pmatrix} \cos \theta_W & \sin \theta_W \\ -\sin \theta_W & \cos \theta_W \end{pmatrix} \begin{pmatrix} B_\mu \\ W_\mu^3 \end{pmatrix} \quad (2.1)$$

516 The value of θ_W is not predicted by the SM; it is one example of an experimental input to the
 517 theory, measured to be $\sin^2 \theta_W = 0.23153 \pm 0.00016$ [10]. The charged W^\pm bosons are a mixture of
 518 the remaining W_μ^1 and W_μ^2 bosons:

$$W^\pm = \frac{1}{\sqrt{2}}(W_\mu^1 \mp iW_\mu^2) \quad (2.2)$$

519 Unlike the photon (and the gluon of QCD), the W^\pm and Z bosons are massive. This means that
 520 even though SU(2) is non-Abelian, the range of interaction is short and confinement does not occur.
 521 Lastly, the EWK interaction is chiral, only coupling to the left-handed component of the fermion
 522 fields

523 One final field remains within the SM: the scalar Higgs field. It was originally proposed in the
 524 1960's to explain the masses of the W^\pm and Z bosons [11, 12, 13] and is the mechanism for the
 525 EWSB process. The predicted Higgs boson is a massive scalar boson, which was at last discovered
 526 by ATLAS and CMS in 2012 [44, 45] with a mass of 125 GeV.

527 2.2 Electroweak symmetry breaking and the Higgs boson

528 The results of electroweak mixing and the implications of the Higgs field have been introduced
 529 in the previous section. If the EWK theory were an unbroken symmetry, the associated W^\pm and
 530 Z bosons would be massless; however, when observed experimentally, they were found to be quite
 531 heavy [14, 15], at around 80 GeV and 91 GeV, respectively [16]. Here, a more detailed explanation
 532 of the Higgs mechanism and how it "spontaneously breaks" the EWK symmetry, resulting in the
 533 three massive bosons (W^\pm and Z) and one massless boson (photon), is presented.

534 To see how the Higgs mechanism results in the massive vector bosons and a massless photon,
 535 consider the following. Beginning with a complex scalar doublet ϕ defined as:

$$\phi = \begin{pmatrix} \phi^+ \\ \phi^0 \end{pmatrix} = \sqrt{\frac{1}{2}} \begin{pmatrix} \phi_1 + i\phi_2 \\ \phi_3 + i\phi_4 \end{pmatrix} \quad (2.3)$$

536 a Lagrangian \mathcal{L} can be written:

$$\mathcal{L} = (\mathcal{D}_\mu \phi)^\dagger (\mathcal{D}^\mu \phi) - \mu^2 \phi^\dagger \phi - \lambda(\phi^\dagger \phi)^2 \quad (2.4)$$

537 where $\lambda > 0$ and \mathcal{D}_μ is the covariant derivative. \mathcal{D}_μ is defined such that \mathcal{L} is invariant under a local
 538 SU(2) \times U(1) gauge transformation:

$$\mathcal{D}_\mu \phi = \left(\partial_\mu + \frac{ig}{2} \tau_a W_\mu^a + \frac{ig'}{2} B_\mu \right) \phi \quad (2.5)$$

539 where W_μ^a ($a = 1, 2, 3$) are the SU(2) fields with generators τ_a and coupling constant g , and B_μ is
 540 the U(1) field with coupling constant g' .

541 Isolating the potential term:

$$V(\phi) = \mu^2 \phi^\dagger \phi + \lambda(\phi^\dagger \phi)^2 \quad (2.6)$$

542 a choice must be made on the sign of μ^2 , and the case of interest is for $\mu^2 < 0$. This results in
 543 the famous “mexican hat potential” shown in Figure 2.1, which is minimized along the collection of
 544 points:

$$\phi^\dagger \phi = \frac{1}{2} (\phi_1^2 + \phi_2^2 + \phi_3^2 + \phi_4^2) = -\frac{\mu^2}{2\lambda} \quad (2.7)$$

545 This means that the minimum of the potential is not at $\phi = 0$ (as it would be in the case where
 546 $\mu^2 > 0$), but rather at a value:

$$v \equiv \sqrt{-\frac{\mu^2}{\lambda}} \quad (2.8)$$

547 With no loss of generality due to the SU(2) symmetry, $\phi_1 = \phi_2 = \phi_4 = 0$ can be set in Equation 2.8
 548 leaving $\phi_3^2 = v^2$. Finally, the *vacuum expectation value* (VEV) of the field can be written as:

$$\langle \phi \rangle = \sqrt{\frac{1}{2}} \begin{pmatrix} 0 \\ v \end{pmatrix} \quad (2.9)$$

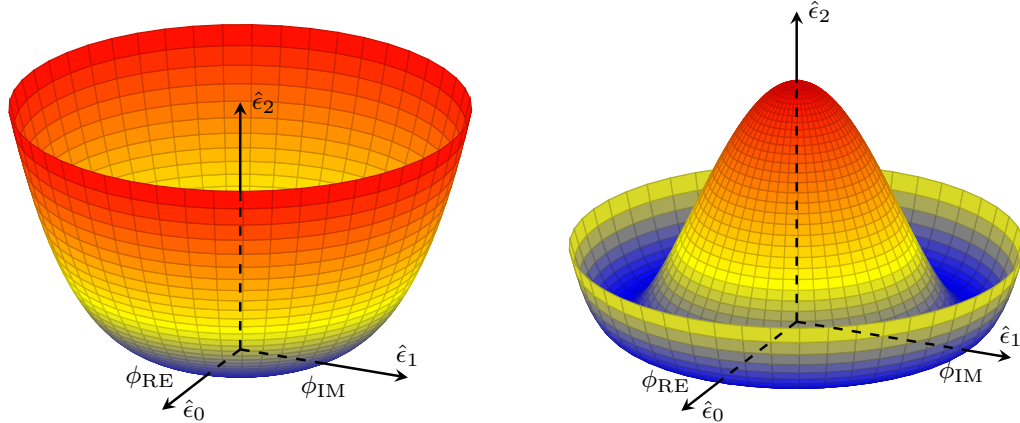


Figure 2.1: An illustration of the potential term $V(\phi)$ in the cases where $\mu^2 > 0$ (left) and $\mu^2 < 0$ (right). The right-hand plot shows the Higgs potential, or “Mexican hat potential”, with the minimum at $|\phi| = \sqrt{-\frac{\mu^2}{\lambda}}$ rather than at $|\phi| = 0$ as in the left-hand plot.

549 The VEV can be substituted back into the original Lagrangian in Equation 2.4, and, following
 550 quite a bit of math, a collection of mass terms can be identified:

$$\mathcal{L} \subset \mathcal{L}_M \equiv \frac{1}{8} v^2 g^2 \left[(W_\mu^1)^2 + (W_\mu^2)^2 \right] + \frac{1}{8} v^2 \left[g^2 (W_\mu^3)^2 - 2gg' W_\mu^3 B^\mu + g'^2 (B_\mu)^2 \right] \quad (2.10)$$

551 Focusing on the first term for the moment, substituting in Equation 2.2 for the physical W^\pm bosons,
 552 the mass term can be seen clearly:

$$M_W^2 W^+ W^- = \left(\frac{1}{2}vg\right)^2 W^+ W^- \quad (2.11)$$

553

$$M_W = \frac{1}{2}vg \quad (2.12)$$

554 With a bit of clever forward-thinking, the second term of Equation 2.10 can be rewritten as:

$$\frac{1}{8}v^2 \left[gW_\mu^3 - g'B_\mu \right]^2 + 0 \left[g'W_\mu^3 - gB_\mu \right]^2 = \frac{1}{2}M_Z^2 Z_\mu^2 + \frac{1}{2}M_A^2 A_\mu^2 \quad (2.13)$$

555 where Z_μ^2 and A_μ^2 represent the physical Z boson and photon, respectively, and are defined as:

$$Z_\mu = \frac{gW_\mu^3 - g'B_\mu}{\sqrt{g^2 + g'^2}} \quad (2.14)$$

556

$$A_\mu = \frac{g'W_\mu^3 - gB_\mu}{\sqrt{g^2 + g'^2}} \quad (2.15)$$

557 From this, it can be seen that the photon is massless, and the mass of the Z boson is identified as:

$$M_Z = \frac{1}{2}v\sqrt{g^2 + g'^2} \quad (2.16)$$

558 Lastly, the Higgs field can couple directly to the fermions. Taking the electron as an example,
 559 an additonal Lagrangian term can be written:

$$\mathcal{L}_e = -G_e [\bar{e}_L \phi e_R + \bar{e}_R \phi^\dagger e_L] \quad (2.17)$$

560 where e_L and e_R are the left-handed doublet and right-handed singlet, respectively, and ϕ is as in
 561 Equation 2.3. The symmetry can be spontaneously broken by a perturbation about the VEV:

$$\phi = \sqrt{\frac{1}{2}} \begin{pmatrix} 0 \\ v + h(x) \end{pmatrix} \quad (2.18)$$

562 which, when substituted into \mathcal{L}_e gives:

$$\begin{aligned} \mathcal{L}_e &= -\frac{G_e}{\sqrt{2}}v(\bar{e}_L e_R + \bar{e}_R e_L) - \frac{G_e}{\sqrt{2}}(\bar{e}_L e_R + \bar{e}_R e_L)h \\ &= -m_e \bar{e}e - \frac{m_e}{v} \bar{e}eh \end{aligned} \quad (2.19)$$

563 for electron mass $m_e = \frac{G_e v}{\sqrt{2}}$. From the second term, it can be seen that the strength of the Higgs
 564 coupling to the electron is proportional to the mass of the electron. The rest of the fermion couplings
 565 follow from this example.

566 What is accomplished here is quite remarkable. The weak and electromagnetic interactions have
567 been unified into a single $SU(2) \times U(1)$ interaction, and the physical bosons observed in nature arise
568 as mixtures of the four gauge fields. Additionally, the non-zero VEV of the Higgs field results in
569 masses for the W^\pm and Z bosons while the photon remains massless. Additionally, it is shown that
570 the Higgs couples to fermions in proportion to their mass. From experimental measurements, the
571 value of the VEV has been determined to be $v \approx 246$ GeV [16]. However, it should be noted that the
572 theory does not predict the mass of the Higgs boson or of the fermions; these must all be determined
573 from experiment.

574 **2.3 Diboson physics**

575 two bosons

576

CHAPTER 3

577

LHC and the ATLAS Detector

578 **3.1 The Large Hadron Collider**

579 The Large Hadron Collider (LHC) [17] is...

580 **3.2 The ATLAS Detector**

581 ATLAS is a general-purpose particle detector...

582 **3.2.1 The Inner Detector**

583 The Inner Detector serves the primary purpose of measuring the trajectories of charged particles...

584 **3.2.1.1 Pixel Detector**

585 The Pixel detector consists of four cylindrical barrel layers and three disk-shaped endcap layers...

586 **3.2.1.2 Semiconductor Tracker**

587 The Semiconductor Tracker uses the same basic technology as the Pixels, but the fundamental unit
588 of silicon is a larger “strip”...

589 **3.2.1.3 Transition Radiation Tracker**

590 The Transition Radiation Tracker is the outermost component of the ID...

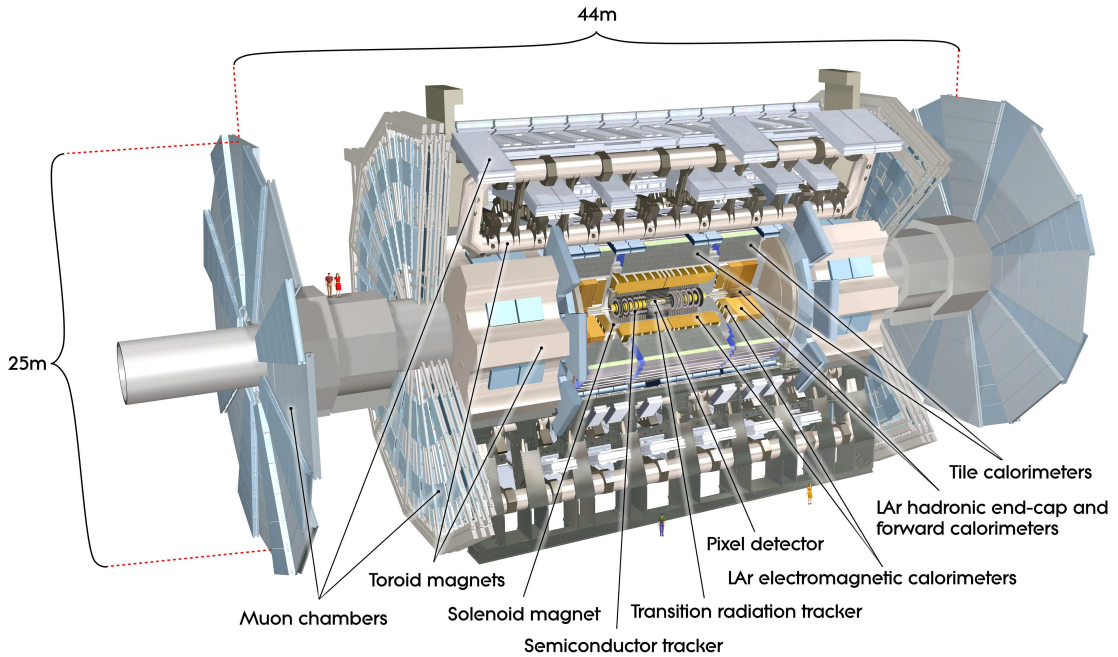


Figure 3.1: General cut-away view of the ATLAS detector [18].

591 3.2.2 The Calorimeters

592 ATLAS includes two types of calorimeter system for measuring electromagnetic and hadronic show-
 593 ers. These are the Liquid Argon (LAr) calorimeters and the Tile calorimeters. Together, these cover
 594 the region with $|\eta| < 4.9\dots$

595 3.2.2.1 Liquid Argon Calorimeters

596 The Liquid Argon system consists of...

597 3.2.2.2 Tile Calorimeters

598 The Tile calorimeter provides coverage for hadronic showers...

599 3.2.3 The Muon Spectrometer

600 Muon spectrometer stuff.

601 **3.2.4 Particle reconstruction**

602 Particle reconstruction algorithms

603 **3.2.4.1 Track reconstruction**

604 **3.2.4.2 Muon reconstruction**

605 **3.2.4.3 Electron reconstruction**

606 **3.2.4.4 Jet reconstruction**

CHAPTER 4

Alignment of the ATLAS Inner Detector

609 When a charged particle passes through the ATLAS ID, it leaves hits in the sensors along its path.
610 In order to accurately measure the track of the particle, it is necessary to know where these hits
611 occurred as precisely as possible, which in turn requires knowledge of the physical location of the
612 element that registered the hit. If one of these elements is *misaligned*, or displaced relative to its
613 position in the known detector geometry, the assumed location of the corresponding hit will not
614 match its actual location, resulting in an incorrect track fit. These misalignments can occur for
615 any number of reasons, including but not limited to elements shifting during maintenance periods
616 or cycles in ATLAS's magnetic field, or small movements during normal detector operations. The
617 effect of a misaligned detector element on the track reconstruction is shown in Figure 4.1.

618 In order to correct the misalignments, the ID alignment procedure is applied to accurately
619 determine the physical position and orientation of each detector element. The baseline accuracy of
620 the alignment is required to be such that the track parameter resolutions are not degraded by more
621 than 20% with respect to those derived from a perfect detector geometry². This corresponds to a
622 precision of better than $10\mu\text{m}$ in the positioning of the elements of the silicon detectors [19].

623 This chapter outlines the ID alignment procedure, the alignment of the detector during the 2015
624 data taking period, and the steps taken to measure momentum biases in the alignment.

²The so-called *perfect geometry* refers to the description of the ATLAS detector in which every sensor precisely matches its design specifications. The perfect geometry contains no misalignments, and the position of each sensor is known exactly.

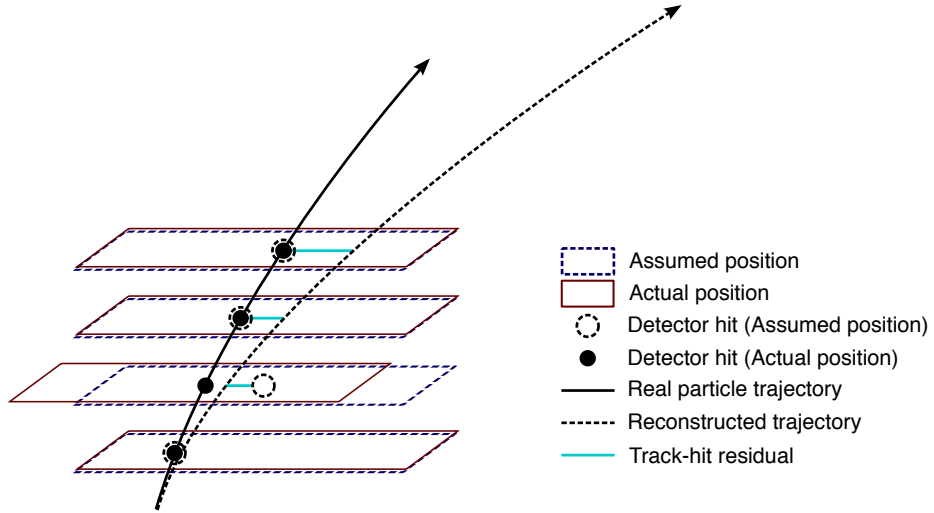


Figure 4.1: Graphical representation of the effect of a misaligned detector element. The reconstructed particle track (dashed arrow) differs from the actual trajectory of the particle (solid arrow) due to the shift in one of the detector elements. The cyan lines represent the track-to-hit residuals.

625 4.1 The alignment method

626 The alignment procedure uses track-based algorithm that updates the locations of detector elements
 627 in order to minimize the set of track-hit *residuals*. These residuals are defined as the distance between
 628 the fitted track position in a given detector element to the position of the hit recorded by the same
 629 element, and are shown by the cyan lines in Figure 4.1. Tracks in ATLAS are parameterized as
 630 five-dimensional vectors [20]:

$$\vec{\tau} = (d_0, z_0, \phi_0, \theta, q/p) \quad (4.1)$$

631 where d_0 and z_0 are the transverse and longitudinal impact parameters with respect to the origin,
 632 respectively, ϕ_0 is the azimuthal angle of the track at the point of closest approach to the origin, θ
 633 is the polar angle, and q/p is the charge of the track divided by its momentum. The residual for the
 634 i^{th} hit of a given track can then be written in terms of the track parameters $\vec{\tau}$ and a set of alignment
 635 parameters \vec{a} that describe the hit location [21]:

$$r_i(\vec{\tau}, \vec{a}) = (\vec{m}_i - \vec{e}_i(\vec{\tau}, \vec{a})) \cdot \hat{k} \quad (4.2)$$

636 where \vec{e}_i is the intersection point of the extrapolated track with the sensor, \vec{m}_i is the position of the
 637 associated hit within the sensor, and \hat{k} is the unit vector defining the direction of the measurement
 638 within the sensor. \vec{r} is then the vector of residuals for the given track.

639 A χ^2 function can be built from the residuals of all collected tracks:

$$\chi^2 = \sum_{\text{tracks}} \vec{r}^T V^{-1} \vec{r} \quad (4.3)$$

640 where V is the covariance matrix of the hit measurements. The χ^2 function is then minimized with
641 respect to the alignment parameters \vec{a} , which contain all degrees of freedom being aligned. The
642 minimization condition with respect to \vec{a} is:

$$\frac{d\chi^2}{d\vec{a}} = 0 \rightarrow 2 \sum_{\text{tracks}} \left(\frac{d\vec{r}}{d\vec{a}} \right)^T V^{-1} \vec{r} = 0 \quad (4.4)$$

643 This equation can be difficult to solve exactly, so the residual is rewritten as a first order Taylor
644 expansion:

$$\vec{r} = \vec{r}_0 + \frac{d\vec{r}}{d\vec{a}} \delta\vec{a} \quad (4.5)$$

645 where \vec{r}_0 is dependent on an initial set of track and alignment parameters \vec{r}_0 and \vec{a}_0 , respectively;
646 the track parameter dependence has also been folded into the total derivative $\frac{d\vec{r}}{d\vec{a}}$. Equation 4.5 can
647 then be inserted into the minimization condition from Equation 4.4 to give:

$$\left[\sum_{\text{tracks}} \left(\frac{d\vec{r}}{d\vec{a}} \right)^T V^{-1} \left(\frac{d\vec{r}}{d\vec{a}} \right) \right] \delta\vec{a} + \sum_{\text{tracks}} \left(\frac{d\vec{r}}{d\vec{a}} \right)^T V^{-1} \vec{r}_0 = 0 \quad (4.6)$$

648 From this equation, the alignment matrix \mathcal{M}_a and alignment vector $\vec{\nu}_a$ can be defined:

$$\mathcal{M}_a = \sum_{\text{tracks}} \left(\frac{d\vec{r}}{d\vec{a}} \right)^T V^{-1} \left(\frac{d\vec{r}}{d\vec{a}} \right) \quad (4.7)$$

649

$$\vec{\nu}_a = \sum_{\text{tracks}} \left(\frac{d\vec{r}}{d\vec{a}} \right)^T V^{-1} \vec{r}_0 \quad (4.8)$$

650 Finally, the alignment corrections $\delta\vec{a}$ can be solved for by inverting the alignment matrix:

$$\delta\vec{a} = -\mathcal{M}_a^{-1} \vec{\nu}_a \quad (4.9)$$

651 which is a linear system of equations with a number of equations equal to the number of alignment
652 degrees of freedom [22].

653 Inverting the matrix and solving this system of equations is referred to as *Global χ^2* align-
654 ment [21]. This can be useful, as \mathcal{M}_a contains all the correlations between the alignable structures.
655 However, inverting the matrix becomes difficult when the number of degrees of freedom becomes
656 large, and as the number of alignable structures increases, so too does the size of the matrix \mathcal{M}_a .
657 Eventually inverting the matrix becomes too computationally intensive to be practical.

658 This problem is solved by the *Local* χ^2 algorithm [23]. In this case, the alignment matrix is
 659 constructed to be block-diagonal, allowing for it to be inverted even for large numbers of degrees of
 660 freedom. This is achieved by replacing the full derivative in Equation 4.6 with the partial derivative
 661 $\frac{\partial \vec{r}}{\partial \vec{a}}$. The new alignment matrix \mathcal{M}'_a and alignment vector $\vec{\nu}'_a$ become:

$$\mathcal{M}_a = \sum_{\text{tracks}} \left(\frac{\partial \vec{r}}{\partial \vec{a}} \right)^T V^{-1} \left(\frac{\partial \vec{r}}{\partial \vec{a}} \right) \quad (4.10)$$

$$\vec{\nu}_a = \sum_{\text{tracks}} \left(\frac{\partial \vec{r}}{\partial \vec{a}} \right)^T V^{-1} \vec{r}_0 \quad (4.11)$$

662 663 Inverting \mathcal{M}'_a is considerably faster and less intensive even for large numbers of degrees of freedom;
 664 however, the correlations between the alignable structures is lost.

665 Due to the Taylor expansion used in Equation 4.6, several iterations of the alignment algorithm
 666 may be necessary to converge on a final set of alignment constants. The Local χ^2 alignment typically
 667 requires more iterations due to the loss of the correlation information [24]. In practice, the ATLAS
 668 reconstruction is run over a set of events, and the resulting tracks are fed to the alignment algorithm.
 669 The residuals are calculated, the alignment matrix is built and inverted, and a new set of alignment
 670 constants is obtained. The convergence of the alignment can be checked by:

671 1. Measure the $\Delta\chi^2$ with the previous iteration. If it is near zero, then the χ^2 is approaching its
 672 minimum.

673 2. Looking at the residual distributions for different alignable structures. A well aligned detector
 674 will have a mean residual of zero with a width approximating the intrinsic resolution of the
 675 detector.

676 If the above checks are satisfied, the process is finished and the final alignment constants are read
 677 out; if not, another iteration is performed. A visual representation of the alignment chain is shown
 678 in Figure 4.2.

679 Since a χ^2 minimization is used to align the detector, if there is a systematic misalignments in
 680 the detector that does not adversely affect the χ^2 , the algorithm will be insensitive to it. These
 681 misalignments are referred to as *weak modes*, and special care is taken to remove them [25]. One
 682 potential impact of weak modes is a bias in the track momentum of reconstructed particles. This
 683 particular effect is the subject of Section 4.4.

684 In practice, the detector is aligned both in “real-time” as data is collected, and during dedicated
 685 offline alignment campaigns. The real-time alignment is run in ATLAS’s so-called *calibration loop*,

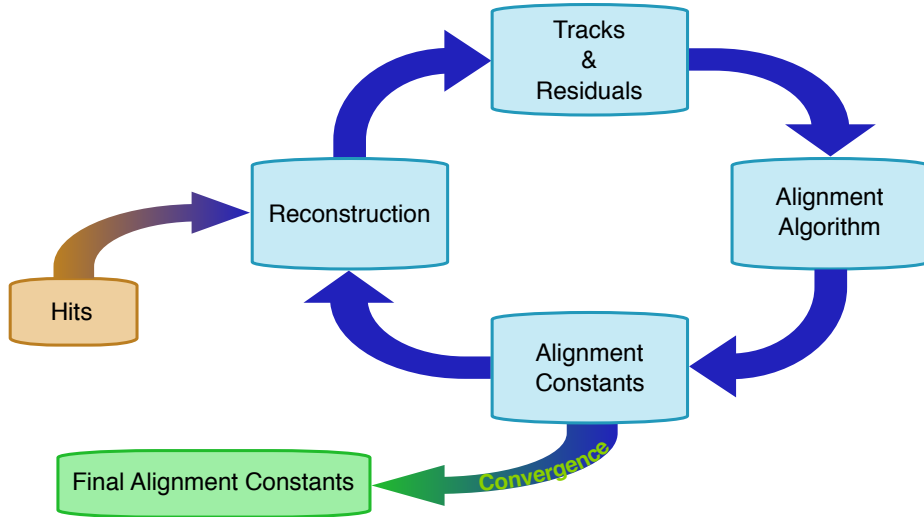


Figure 4.2: Graphical representation of the ID alignment chain.

which comprises the first stage in the preparation of data for physics analysis. The calibration loop requires the alignment as well as various other detector calibrations to be available within 48 hours for initial data processing. A fast, coarse-grained alignment³ is run on a subset of the available data containing full tracking information, and the results are propagated to the reconstruction of that particular run [26]. Due to the time constraints of the calibration loop, a full sensor-by-sensor alignment is not possible.

The more thorough and finely tuned alignments are reserved for the dedicated alignment campaigns. These generally occur early in data taking campaigns, typically once a sufficient amount of data is collected after a detector shutdown, in order to obtain a good baseline alignment for use in the remainder of the data collection period. Once data taking is complete, another campaign determines an improved set of alignment constants (divided into several “blocks” to account for time-dependent misalignments), and the full data is reprocessed using the newly derived detector geometry. The initial offline alignment of the ATLAS detector at the beginning of Run 2 in 2015 is the subject of Section 4.2.

4.1.1 Alignment levels

The alignment of the detector is performed at several levels of increasing granularity. This adds flexibility in being able to align only as finely as needed, and it also allows for global, detector-level

³The calibration loop runs up to a Level 2 alignment in the silicon detectors, which involves treating each layer of sensors as a single object, defined in greater detail in Table 4.1.

703 misalignments to be corrected first before dealing with finer adjustments.

- 704 • Level 1 (L1) alignment involves moving entire subdetector components as a single unit, such
705 as the entire Pixel detector, or the SCT barrel. These often have the largest misalignments,
706 but they are easily corrected and do not require large volumes of data to do so.
- 707 • Level 2 (L2) alignment treats individual layers in the silicon detectors (modules in the TRT)
708 and end cap disks as individual alignable objects.
- 709 • Level 2.7 (L27) alignment was introduced with the addition of the IBL to the ID in Run 2. It
710 involves the stave-by-stave alignment of the IBL and Pixel barrel⁴.
- 711 • Level 3 (L3) alignment treats each sensor in the silicon detectors and each straw in the TRT
712 as an individual alignable object. It is the finest grained alignment available but also the most
713 computationally intensive due to the large number of degrees of freedom. The large number
714 of individual detector sensors being aligned also requires the largest amount of statistics.

715 The different alignment levels are listed in more detail in Table 4.1, including the number of alignable
716 structures and associated degrees of freedom for each detector component.

717 The implementation of the alignment algorithm in the software is flexible enough to allow each
718 subsystem to be aligned individually at a specified level. Each alignable structure has six degrees of
719 freedom: 3 translations (T_x, T_y, T_z) and 3 rotations (R_x, R_y, R_z)⁵; however individual degrees of
720 freedom may be turned on and off as required. In a typical alignment job, L1 and L2 contain few
721 enough degrees of freedom that the Global χ^2 algorithm can be used, but L3 alignments (which can
722 contain over 36,000 degrees of freedom in the silicon detectors alone) require the Local χ^2 algorithm.

723 4.1.2 Alignment coordinate systems

724 The global coordinate system (x, y, z) used by the ID alignment matches that of the ATLAS
725 detector in general, as detailed in Section 3.2 **TODO: update with actual location of figure when**
726 **it's in....** The positions and orientations of individual detector modules of the ID are defined by
727 a right-handed local coordinate system (x', y', z') where the origin is defined as the geometrical
728 center of the module. The x' -axis for each silicon module is defined to point along the most sensitive

⁴For the purposes of this Chapter, the term “Pixel” will refer to the original three layers of the Pixel detector, and the IBL will be referenced separately.

⁵The TRT is an exception, as the subdetector does not have any resolution along the length of the straw. Therefore, for the barrel, T_z is omitted. Similarly for the straws themselves, only two parameters are defined: translation with respect to the radial direction (T_ϕ) and rotation with respect to the radial axis (R_r for the barrel and R_z for the end-caps) [27].

Level	Description of alignable structure	Structures	DoF
1	IBL detector	1	6
	Whole Pixel detector	1	6
	SCT barrel and 2 end-caps	3	18
	TRT barrel and 2 end-caps (T_z fixed)	3	17
Total:		8	47
2	IBL detector	1	6
	Pixel barrel layers	3	18
	Pixel end-cap disks	2×3	36
	SCT barrel layers	4	24
	SCT end-cap disks	2×9	108
	TRT barrel 32 modules (T_z fixed)	3×32	480
	TRT end-cap wheels	2×40	480
Total:		208	792
2.7	IBL staves	14	84
	Pixel barrel staves	$22+38+52$	672
	Pixel end-cap disks	2×3	18
	Total:		132
3	IBL modules	280	1,680
	Pixel modules	1,744	10,464
	SCT modules	4,088	24,528
	TRT barrel wires (T_ϕ, R_r only)	105,088	210,176
	TRT end-cap wires (T_ϕ, R_Z only)	245,760	491,520
	Total silicon sensors:		6,112
	Total TRT wires:		350,848
Total:		36,672	701,696

Table 4.1: The four alignment levels for each of the detector subsystems. The total number of alignable structures and degrees of freedom (DoF) to be aligned are given for each level.

729 direction of the module, the y' -axis is oriented along the long side of the module, and the z' -axis is
 730 orthogonal to the (x', y') plane. For the TRT straws, the x' -axis is perpendicular to both the wire
 731 and the radial direction, defined from the origin of the global frame to the straw center, the y' -axis
 732 points along the straw, and once again the z' -axis is orthogonal to the (x', y') plane. A depiction of
 733 the global and local coordinate systems for the ID is shown in Figure 4.3.

734 When considering the alignment degrees of freedom listed earlier in Section 4.1.1, grouped collec-
 735 tions of modules, layers, or entire subdetectors use the global coordinate system; individual modules
 736 use their respective local coordinate systems. The translations T_i are with respect to the origin of
 737 the given reference frame, and the rotations R_i are taken about the Cartesian axes.

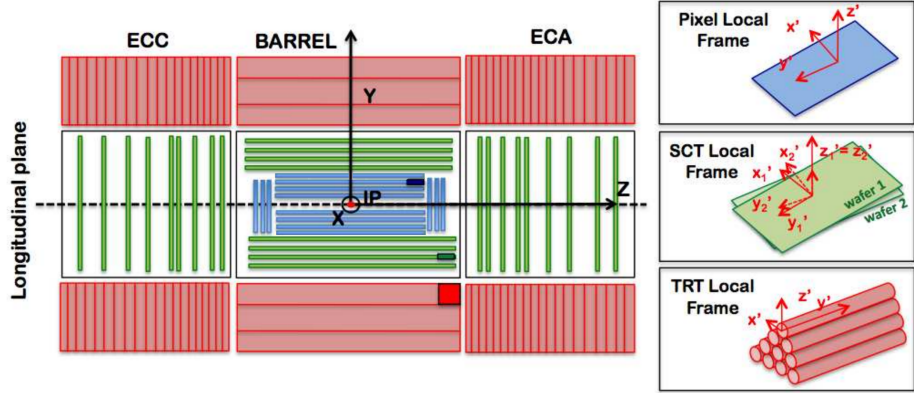


Figure 4.3: A schematic representation of the Inner Detector in the longitudinal plane with the global coordinate system overlaid on top. The Pixel detector and IBL are shown in blue, the SCT in green, and the TRT in red. The local coordinates for each subdetector module are inset on the right. Image taken from [28].

738 4.2 Early 2015 alignment of the ATLAS detector

739 At the end of Run 1, the LHC was shut down for upgrades and maintenance. During this time,
 740 a number of upgrades were performed on the ATLAS detector, including the installation of a new
 741 innermost layer of the Pixel detector, the Insertable B-Layer (IBL) [29]. **TODO: This will certainly**
 742 **be defined in the detector description, so maybe the citation and abbreviation are not needed** These
 743 changes to the ID required some detector components to be removed temporarily, and many elements
 744 shifted relative to each other over the course of the maintenance process. In order to correct for
 745 these large detector movements prior to $\sqrt{s} = 13$ TeV collision data taking, an alignment was
 746 performed using cosmic ray data collected in early 2015 [28]. This alignment was able to correct
 747 for the majority of the large detector-wide misalignments as well as determine the global position
 748 of the IBL at the micron level.

749 In June of 2015, shortly after the data taking period began, the first track-based alignment of
 750 the refurbished ID was performed using $\mathcal{L} = 7.9 \text{ pb}^{-1}$ of $\sqrt{s} = 13$ TeV pp collision data [30].
 751 Starting from the initial geometry determined by the cosmic ray alignment, referred to hereafter
 752 as the *March alignment*, an improved set of alignment constants, called the *June alignment*, was
 753 derived from a data set of approximately 1.4 million selected tracks. For comparison, a MC sample
 754 containing approximately 2.7 million tracks was constructed from dijet events simulated using a
 755 perfect detector geometry; the MC events are reweighted to match the η and p_T distributions found
 756 in the data. Additional validation of the alignment results uses a set of cosmic ray data collected

757 by the detector during the LHC collisions. **TODO:** find some way of saying that this section follows
 758 the alignment note [30]? or is it ok not to...

759 4.2.1 June alignment procedure

760 The data set used as the input for the alignment contains a subset of physics events used for prompt
 761 reconstruction recorded at a rate of 10 Hz. To ensure that only high quality tracks are used for the
 762 alignment, each track is required to have transverse momentum $p_T > 3$ GeV, contain at least one
 763 hit in the Pixel detector, at least seven hits in the combined silicon detectors, and at least 25 hits
 764 in the TRT.

765 A full L3 alignment of the IBL was included in the March alignment; however, a realignment
 766 was necessary. Since the cosmic rays pass through the detector top-down, the staves on the sides of
 767 the IBL could not be aligned as precisely as those on the top and bottom due to lower statistics.
 768 Additionally, the IBL was operating at a temperature of -20°C during the cosmic data taking
 769 and at -10°C for collision data taking. This proved to be significant, as it was observed that
 770 the IBL staves experience a temperature-dependent, parabolic bowing in the local x' -direction of
 771 approximately $-10\mu\text{m}/\text{K}$ [31]. As a result, a full L3 alignment of the IBL was essential in order to
 772 correct for the bowing. Due to it being a brand new element of the detector as well as its importance
 773 in vertexing and b jet tagging, aligning the IBL sensors with a high degree of precision was of great
 774 importance.

775 The June alignment was performed in two stages, with the first pass focusing on relative move-
 776 ments of the big structures and correcting for the bowing of the IBL. The March alignment corrected
 777 for these larger movements as well; however, it was observed during Run 1 that these sort of mis-
 778 alignments are introduced by changing conditions in the detector [25], such as in the cooling system
 779 or magnet power cycling, which may have occurred between the early cosmic data taking and the
 780 first $\sqrt{s} = 13$ TeV collisions. The silicon detectors were aligned at several different levels and the
 781 IBL was aligned at the module level; the TRT detector was kept fixed to act as a global reference
 782 frame. The full alignment chain for the first pass consisted of the following steps:

- 783 1. The IBL, Pixel, and SCT detectors were aligned at L1. The SCT barrel was not aligned in
 784 T_z in order to constrain global displacements along the z -axis, as the TRT is not sensitive to
 785 that degree of freedom.
- 786 2. The IBL, and Pixel barrel and end-caps, and SCT barrel were aligned at L2. The SCT end-caps
 787 were aligned at L1.

- 788 3. The IBL and pixel barrel were aligned at L27, using all six degrees of freedom. The Pixel
 789 end-cap disks were only aligned in the plane (T_x , T_y , and R_z). The SCT was treated the same
 790 as in the previous step.
- 791 4. The IBL was aligned at L3 using all six degrees of freedom for each module.

792 The primary goal for the second pass was to remove a bias in the transverse impact parameter
 793 d_0 present in the March alignment. The resolution of d_0 was also poorer than expected. In order
 794 to correct for this, an additional constraint was passed to the alignment by adding an impact
 795 parameter with respect to the beam spot as a pseudo-measurement [32]. When the alignment
 796 algorithm minimizes the χ^2 , it will take care of the impact parameter minimization as well. Only
 797 the IBL and Pixel detectors were aligned in this step. The stages of the second pass are listed below,
 798 and the beam spot constraint was used in each:

- 799 1. The IBL and Pixel detectors were aligned at L2 with the SCT fixed.
 800 2. The IBL was aligned at L27
 801 3. The IBL and Pixel barrel and end-caps were aligned at L3.

802 The set of alignment constants obtained at the end of the second pass represents the June alignment.
 803 The highest level of alignment over the course of the two passes for each subdetector is listed in
 804 Table 4.2.

Detector	Highest level of alignment
IBL	L3
Pixel	Barrel
	End-caps
SCT	Barrel
	End-caps
TRT	None

Table 4.2: Summary of the highest level of alignment applied to each ID subsystem when deriving the June alignment.

805 4.2.2 Alignment results

806 The primary measure of alignment quality is assessed by looking at the track-hit residual distri-
 807 butions. If the detector is well aligned, the residuals will be Gaussian-distributed with a mean

of zero and a width approximating the detector's resolution. The residual distributions are constructed from the same selection of tracks that were used to perform the alignment, and are the focus of Section 4.2.2.1. A second check on the alignment involves observables sensitive to the track parameter resolution. In this case, cosmic rays are used, making use of a “split track” technique that takes advantage of the top-to-bottom cosmic ray trajectory (compared to the center-out trajectory of collision tracks). This method and the corresponding tests of the alignment are detailed in Section 4.2.2.2

Additionally, the effect of the beam spot constrained alignment on the impact parameter d_0 needs to be checked. The d_0 distributions for both the March and June alignments are compared to the MC simulation using a perfect geometry in Figure 4.4. In the March alignment, there is a bias of 18 μm in the mean of the distribution and the width is nearly twice that of the perfect geometry. After the second pass of the June alignment, the mean has shifted to 1 μm and the distribution has narrowed considerably. From this, it appears that the constrained alignment successfully removed the d_0 bias.

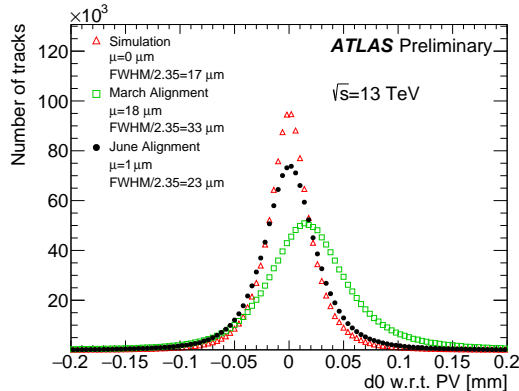


Figure 4.4: The d_0 distributions with respect to the reconstructed primary vertex using the $\sqrt{s} = 13 \text{ TeV}$ collision data sample reconstructed using the June (black) and March (green) alignments. The data is compared to a MC simulation using a perfect detector geometry (red). The distributions are normalized to the same number of entries.

4.2.2.1 Residual distributions from collisions

As mentioned previously, the primary focus of the June alignment campaign was on the IBL and the Pixel detectors. The detectors are the closest to the beam line and have the finest resolutions of the

825 ID subdetectors. The residual distributions in local x and y of the IBL planar sensors⁶ are shown
 826 in Figure 4.5. These and subsequent figures in this section compare the June and March alignments
 827 to the perfectly-aligned MC simulation. Noticeable improvement in the distribution widths can be
 828 seen in both the local x - and y -directions, nearly matching the simulation in local x , which is the
 829 most sensitive direction.

830 Due to the temperature-dependent bowing of the IBL, it is also interesting to look at the means of
 831 the residual distributions for each ring of IBL sensors along the beam line, as shown in Figure 4.6. A
 832 deformation is clearly visible in the March alignment in both measurement directions, and the shape
 833 in the local x -direction is consistent with an average stave bowing due to the different operating
 834 temperature of the IBL during the March alignment and the 13 TeV collisions. This feature was
 835 nearly eliminated in both directions through the L3 alignment of the IBL sensors.

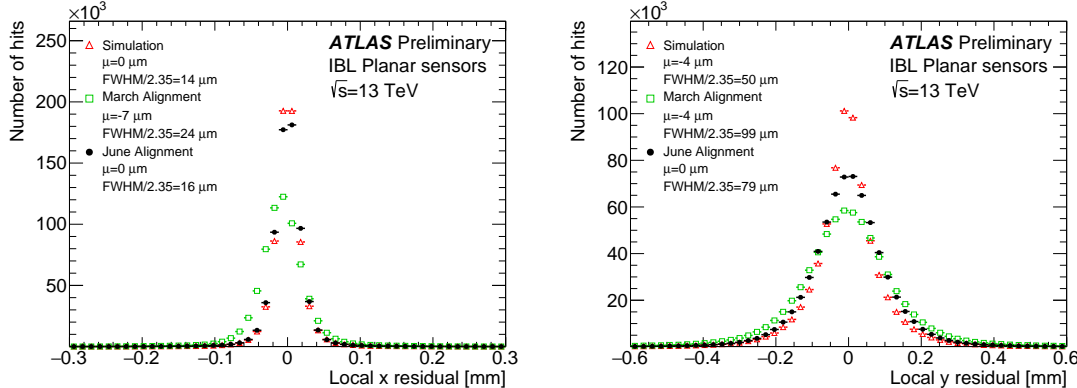


Figure 4.5: Local x (left) and local y (right) residual distributions of the IBL planar sensors using the $\sqrt{s} = 13$ TeV collision data sample reconstructed using the June (black) and March (green) alignments. The data is compared to a MC simulation using a perfect detector geometry (red). The distributions are normalized to the same number of entries.

836 The local x and y residual distributions for the Pixel detector barrel and end-caps are shown in
 837 Figure 4.7. Even though the IBL is not included in the plots of the barrel, some of the noticeable
 838 improvement in the more sensitive local x direction is an effect of the improved IBL alignment.
 839 Similarly, the relatively broad local y residual distribution in the barrel likely indicates that further
 840 refinement of the IBL alignment was needed along that direction. Even so, the June alignment
 841 outperforms the March alignment and rivals the simulation in most of the plots.

⁶The IBL contains 12 planar sensors in the center of a stave, with four 3D sensors on either end. Only the planar sensors are shown here due to low statistics in the 3D sensors as well as poor MC modeling of these sensors.

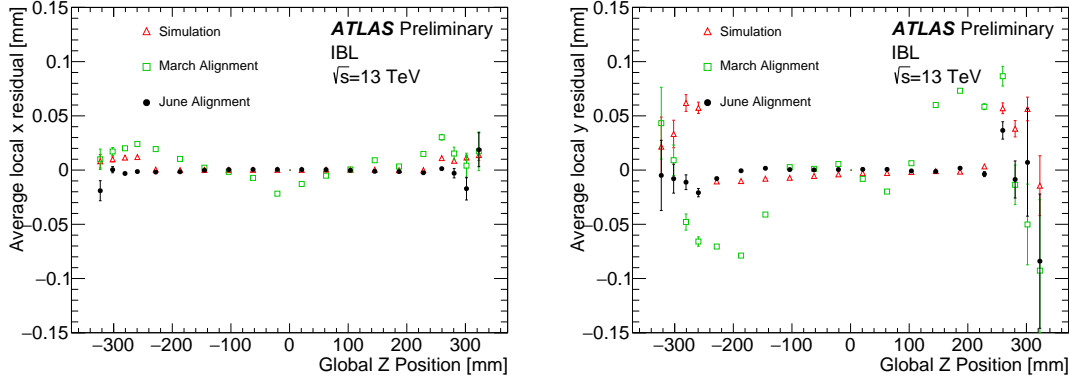


Figure 4.6: The mean of the local x (left) and local y (right) residual distributions as a function of the global z position of each IBL module using the $\sqrt{s} = 13$ TeV collision data sample reconstructed using the June (black) and March (green) alignments. The data is compared to a MC simulation using a perfect detector geometry (red).

842 Similar distributions for the SCT and TRT barrel and end-caps are shown in Figures 4.8 and
 843 4.9, respectively. Much like with the Pixel residuals, there is a reduction in the width of the TRT
 844 residuals between the March and June alignments due to the alignment of the other subdetectors
 845 improving the quality of the track fit. Even though neither subdetector was aligned at module-
 846 level, the residuals indicate that the previous L3 alignment performed in Run 1 has not degraded
 847 significantly during the upgrade and maintenance period.

848 4.2.2.2 Track parameter resolution from cosmic rays

849 Cosmic ray data is very useful as an independent check on the alignment in the barrel of the
 850 detector. While tracks from pp collisions originate within the detector and travel outwards, a cosmic
 851 ray that passes through the center of the detector leaves a track in both halves of the detector.
 852 If the cosmic ray is split in half, as in Figure 4.10, then it can be treated as two separate tracks
 853 each with nearly identical track parameters (some differences arise due to energy loss as the particle
 854 passes through the detector). The distribution of the difference in a given track parameter $\Delta\tau$ is
 855 approximately Gaussian with a variance $\sigma^2(\Delta\tau)$. Since both tracks come from the same particle,
 856 each track individually has a variance equal to $\sigma^2(\Delta\tau)/2$. The resolution of the track parameter is
 857 then given by the root mean square of the distribution divided by $\sqrt{2}$.

858 Cosmic rays whose split tracks each had transverse momentum $p_T > 2$ GeV and at least one,
 859 eight, and 25 hits in the barrels of the Pixel, SCT, and TRT detectors, respectively, were selected to

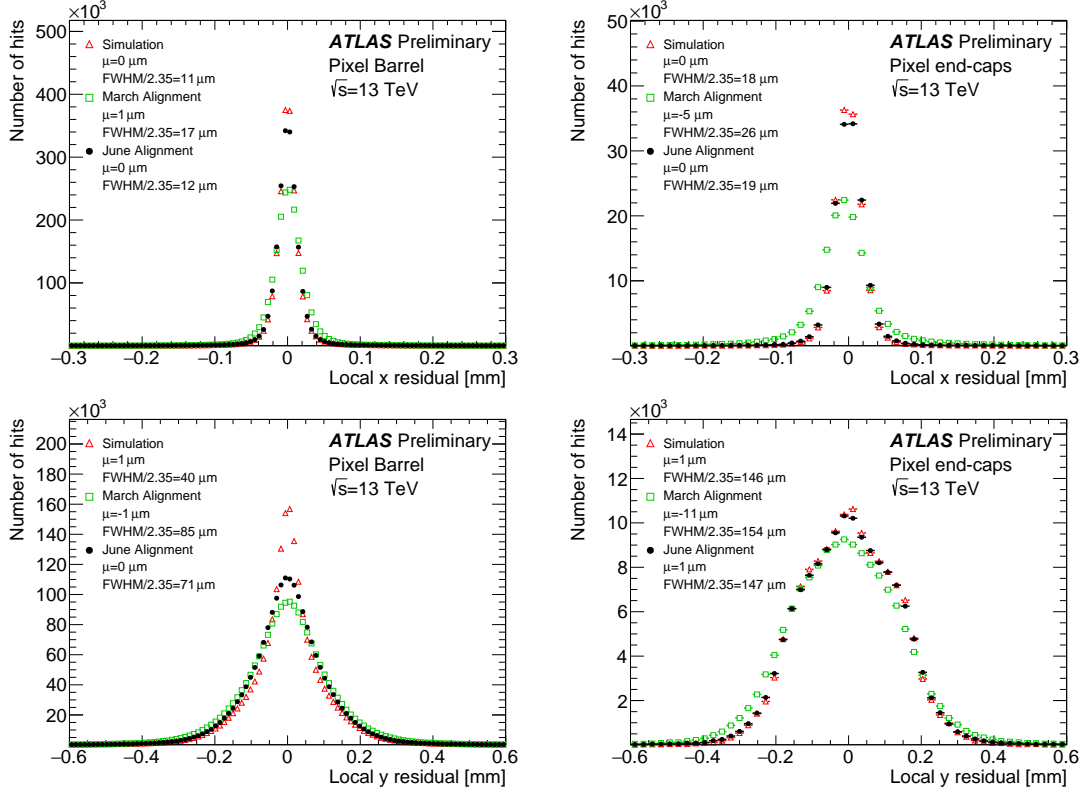


Figure 4.7: Local x (top) and local y (bottom) residual distributions for the Pixel barrel (excluding the IBL, left) and end-caps (right) using the $\sqrt{s} = 13$ TeV collision data sample reconstructed using the June (black) and March (green) alignments. The data is compared to a MC simulation using a perfect detector geometry (red). The distributions are normalized to the same number of entries.

measure a collection of track parameters. Figure 4.11 shows the difference in the impact parameter Δd_0 and the charge divided by the transverse momentum $\Delta q/p_T$ of the selected split-track cosmic rays for both the March and June alignments. Both distributions show a reduction in width in the June alignment, corresponding to an improvement in the resolution of each track parameter. The Δd_0 plot shows a significant improvement in the June alignment, further validating the removal of the bias in the impact parameter.

4.2.3 Error scaling

The final step in preparing the new set of June alignment constants deals with the adjustment of the hit errors, or *error scaling*. Knowledge of the exact position of a hit measurement on a track

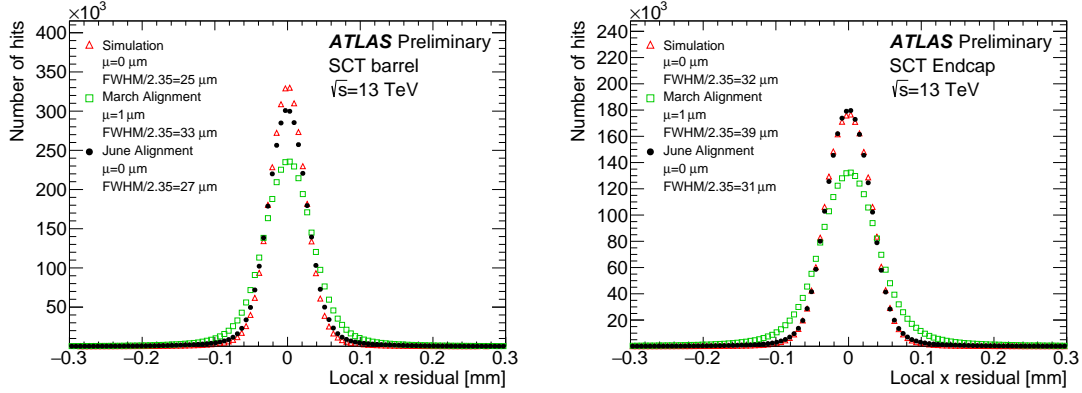


Figure 4.8: Local x residual distributions for the SCT barrel (left) and end-caps (right) using the $\sqrt{s} = 13 \text{ TeV}$ collision data sample reconstructed using the June (black) and March (green) alignments. The data is compared to a MC simulation using a perfect detector geometry (red). The distributions are normalized to the same number of entries.

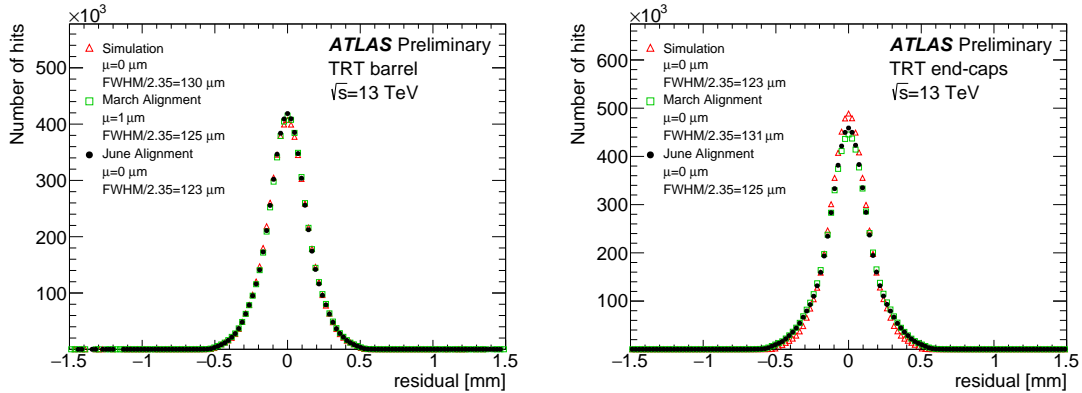


Figure 4.9: Residual distributions for the TRT barrel (left) and end-caps (right) using the $\sqrt{s} = 13 \text{ TeV}$ collision data sample reconstructed using the June (black) and March (green) alignments. The data is compared to a MC simulation using a perfect detector geometry (red). The distributions are normalized to the same number of entries.

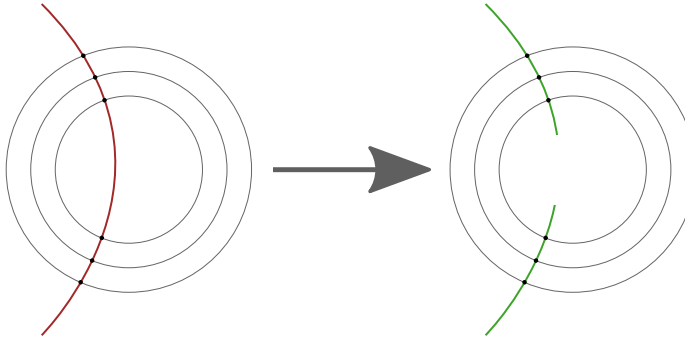


Figure 4.10: Representation of splitting a single cosmic ray track passing through the entire detector (left) into two separate tracks (right).

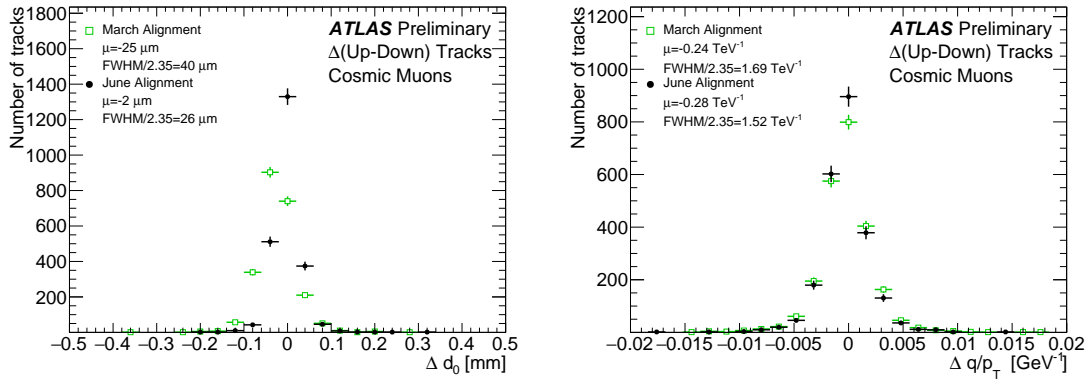


Figure 4.11: Distribution of the difference in the impact parameter Δd_0 (left) and charge over transverse momentum $\Delta q/p_T$ (right) between the two cosmic ray split tracks. The June (black) and March (green) alignments are compared. The distributions are normalized to the same number of entries.

is limited by the accuracy with which the sensors' positions are known. Let σ represent the hit uncertainty used in track fitting, and σ_0 be the detector's intrinsic uncertainty. If $\sigma = \sigma_0$, the pull of the track-hit residual distributions should form a Gaussian distribution centered at zero with a standard deviation $\sigma = 1$ [22]. In the case of residual misalignment, the pull distributions' standard deviations will stray from unity. The hit uncertainty can be written as:

$$\sigma = a \cdot \sigma_0 \oplus b \quad (4.12)$$

where a is a scaling factor, and b is a constant term which can be interpreted as a measure of any remaining misalignment of the detector elements. In this alignment campaign, the value of a is fixed at $a = 1$ and b is evaluated from the residual pull distributions for each subdetector in its sensitive

877 directions.

878 Once the value of b is determined, pull distributions derived from the new value of σ should
 879 have unit width. The error scaling values for each subdetector are listed in Table 4.3, and the pull
 880 distributions for the IBL after error scaling are shown in Figure 4.12.

Detector	Coordinate	$b(\mu\text{m})$
IBL	x	6.4
	y	43.6
Pixel	x	5.2
	y	28.6
SCT	x	7.5
	y	0
SCT	x	10.8
	x	8.6
TRT	$r\phi$	0
	$r\phi$	0

Table 4.3: Estimated value of the error scaling term b for each subdetector component with the June alignment.

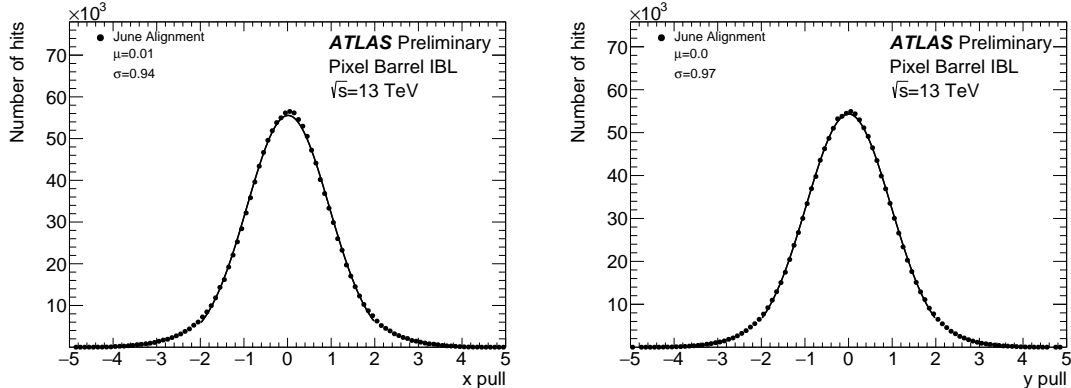


Figure 4.12: Pull distributions in local x (left) and y (right) for the IBL using the $\sqrt{s} = 13 \text{ TeV}$ collision data sample after applying the error scaling.

881 4.3 Level 2 alignment of the TRT

882 During validation of the final end-of-year reprocessing of the 2015 data, a misalignment was found in
 883 the barrel of the TRT detector, as several modules (triangular clusters of straws) showed rotations in
 884 the local y coordinate. The then-best available constants included a full L3 alignment of the silicon
 885 detectors and a separate L2 alignment of the TRT. However, not all degrees of freedom were enabled

when the TRT was aligned. To correct for these tilts, an additional four iterations of L2 alignment was performed on the TRT enabling all available degrees of freedom (T_x , T_y , R_x , R_y , and R_z in the barrel, and T_x , T_y , and R_z for the endcaps). Plots of the residual means from barrel ϕ sectors containing modules affected by the tilt misalignment are shown in Figure 4.13 before and after the L2 alignment.

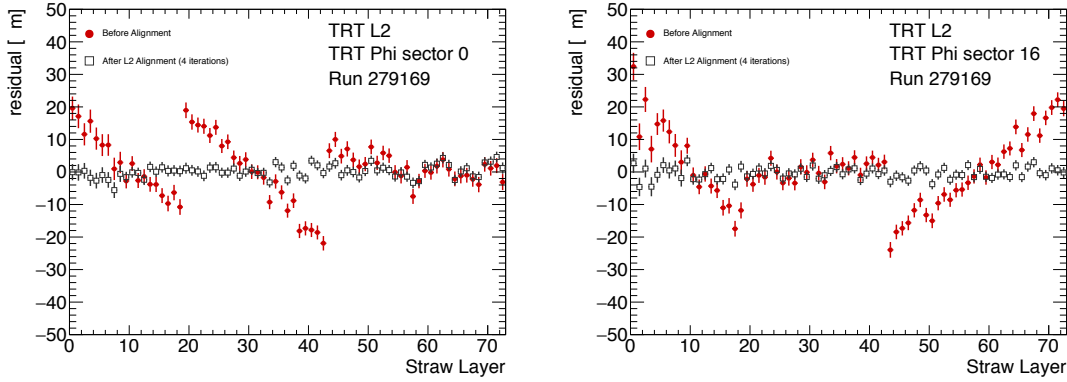


Figure 4.13: Residual means by straw layer in two TRT ϕ -sectors affected by a tilt misalignment. The tilts in each of the three modules are clearly visible in the red points representing the reconstructed data prior to alignment. After four iterations of L2 alignment, the residual means in the gray points are flat.

Following the L2 alignment, some additional time was taken to determine if a full wire-by-wire L3 alignment of the TRT was necessary. The TRT was last aligned at L3 during Run 1, but initial alignment campaigns in Run 2 did not show signs of misalignment, as can be seen from the residual distributions in Figure 4.9. In order to assess the alignment more carefully, two dimensional residual maps in ϕ and z were constructed for each layer in the TRT barrel and endcaps using the current alignment. These maps were compared to a similar set using the L3 alignment from 2010, from which it was determined that the straw-level alignment indeed hadn't degraded and a new L3 alignment was not needed. The maps for the first layer of the TRT barrel are shown in Figure 4.14 for both sets of alignment constants.

4.4 Momentum bias from sagitta deformations

A variety of weak mode deformations can exist in the detector even after alignment. As mentioned previously, these weak modes consist of misalignments which don't affect the χ^2 of the residuals and thus are not handled by the basic alignment algorithm. In the presence of a weak mode, the

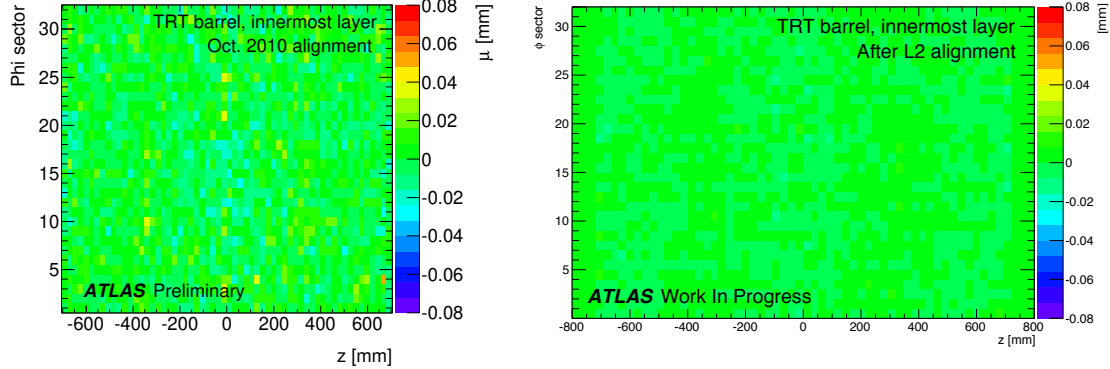


Figure 4.14: Two dimensional map of residuals in the first layer of the TRT barrel vs z and ϕ . Each bin represents the mean of a Gaussian fit to the TRT residuals in that bin. The map on the left is after the L3 (wire-by-wire) alignment of the TRT performed in 2010, and the map on the right is after the L2 alignment at the end of 2015. The z -axis for both plots use the same scale. Left figure taken from [22].

904 description of the detector geometry can still provide efficient and high quality track fits, but there
 905 may also be systematic biases in one or more track parameters. Several weak modes, their impacts
 906 on the reconstruction, and the steps taken to eliminate them are detailed in [25, 33]. This section
 907 focuses specifically on sagitta distortions that result in a bias in the reconstructed track momentum.

908 These *sagitta* distortions consist of detector movements orthogonal to the trajectory of the outgoing
 909 particle. The effect on the reconstructed track curvature is different for positively and negatively
 910 charged particles, resulting in a charge-antisymmetric bias. This effect is illustrated in the curl
 911 deformation shown in Figure 4.15.

912 In the plane transverse to ATLAS’s magnetic field, outgoing particle tracks form circular arcs.
 913 The sagitta is defined as the distance from the center of this arc to the center of its base, as shown in
 914 Figure 4.16, and it represents the “amount of bending” in the track. In the case where the sagitta s
 915 is considerably smaller than the detector radius R_0 , which is a valid assumption when working with
 916 high momentum tracks, the transverse momentum of a particle of charge q can be written as [34]:

$$p_T \propto qB \frac{R_0^2}{8s} \quad (4.13)$$

917 where B is the strength of the detector’s magnetic field. If a sagitta bias is present, the track’s
 918 transverse momentum shifts by [33]:

$$q/p_T \rightarrow q/p_T + \delta_s \quad \text{or} \quad p_T \rightarrow p_T \cdot (1 + qp_T\delta_s)^{-1} \quad (4.14)$$

919 where δ_s is a universal bias parameter that uniquely defines the deformation. Finally, since the

reconstructed polar angle does not change under a sagitta deformation, the longitudinal component of the momentum scales along with the transverse component, and an equivalent equation can be written for the total momentum:

$$p \rightarrow p \cdot (1 + qp_T \delta_s)^{-1} \quad (4.15)$$

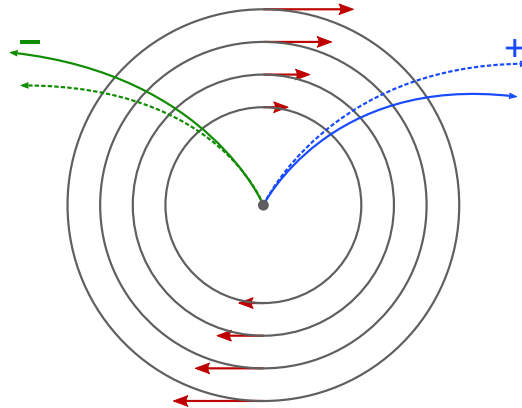


Figure 4.15: Representation of a curl distortion in the detector. The image shows a cutaway in the transverse plane. The deformation is represented by the red arrows, and the impact on the reconstructed positive (blue) and negative (green) tracks are shown. The dashed lines represent the true particle trajectories, and the solid lines represent the reconstructed trajectories.

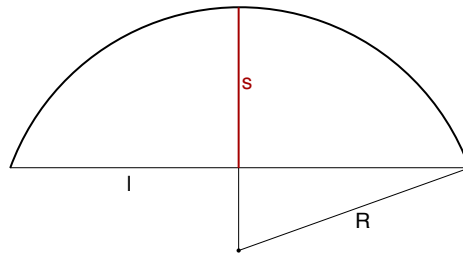


Figure 4.16: Geometric definition of the sagitta s in relation to the length of the chord l and the radius r of a circular arc.

4.4.1 Sagitta bias monitoring with electron E/p

Since a sagitta bias results in changes in the momentum of particles' tracks as measured by the ID, they can be identified using independent measurements from other systems in the detector. One such method involves using the energy-momentum ratio of electrons (E/p). Since the electron's energy is measured in ATLAS's calorimeter systems, it is not sensitive to any sagitta bias that may exist in the ID and the corresponding track momentum. Under the assumption that the calorimeter

929 response is independent of the charge of incoming particles, a charge-dependent momentum bias in
 930 the ID will manifest as a difference in the E/p ratio for electrons and positrons.

931 In the presence of a sagitta bias, the momentum will change according to Equation 4.15 and the
 932 average measured $\langle E/p \rangle$ can be written as:

$$\langle E/p \rangle^\pm \rightarrow \langle E/p \rangle^\pm \pm \langle E_T \rangle \delta_s \quad (4.16)$$

933 where the approximation $p_T \approx E_T$ is used. Assuming that $\langle E/p \rangle^+ = \langle E/p \rangle^-$ in the absense of a
 934 bias, the sagitta bias parameter can be written as:

$$\delta_s = \frac{\langle E/p \rangle^+ - \langle E/p \rangle^-}{2\langle E_T \rangle} \quad (4.17)$$

935 If the kinematic selections for electrons and positrons are identical, the energy scale of the calorimeter
 936 will not factor into the $\langle E/p \rangle$ difference; however, it will affect $\langle E_T \rangle$ which would scale the measured
 937 δ_s . This is expected to be a small effect, as the energy scale for electrons has been measured at
 938 $\sqrt{s} = 13$ TeV with uncertainties on the per-mil level across the entire detector [35].

939 4.4.1.1 Measuring $\langle E/p \rangle$

940 The E/p ratio is measured using electrons and positrons from $Z \rightarrow e^\pm e^\mp$ events in order to obtain
 941 a high purity sample of electron candidates. They are required to pass a basic selection criteria to
 942 ensure they are well measured by both the ID and the calorimeters:

- 943 • $E_T > 25$ GeV
- 944 • $|\eta| < 2.47$, excluding the calorimeter's barrel-to-endcap transition region in $1.37 < |\eta| < 1.52$
- 945 • Pass MediumLH identification working point detailed in Section 3.2.4.3
- 946 • Pass a selection of quality cuts, including a requirement that the electron be identified using
 947 cluster information in the calorimeter
- 948 • The associated track must have at least one hit in the IBL, three in the Pixel detector, and
 949 five in the SCT detector.

950 Events with exactly two opposite-charge electrons passing this selection with a dielectron invariant
 951 mass within 30 GeV of the Z boson mass are then used for the E/p calculation.

952 Since the size of the sagitta bias δ_s is not expected to be constant across the entire detector,
 953 a two-dimensional rectangular grid binned in detector η and ϕ is constructed. From the selected

events, separate distributions of E/p are made for electrons and positrons lying in each bin. Each distribution is fit with Crystal Ball function⁷, and the peak of the distribution is taken as the value of $\langle E/p \rangle$. If there is no bias on the track momentum in the bin, the peaks for electrons and positrons should match. Example E/p distributions including the Crystal Ball fits are shown in Figure 4.17.

It is important to emphasize that deviations from one in the *ratio* of $\langle E/p \rangle$ for electrons and positrons indicates that a momentum bias may be present. The value of $\langle E/p \rangle$ itself is not expected to equal one exactly, as the track momentum on average tends to be slightly lower than the energy measurement in the calorimeter. This is due to the fact that if the electron were to radiate a photon, its momentum would change slightly, while it is likely that both the electron and the emitted photon would leave energy deposits near each other in the calorimeter and be reconstructed into the same object.

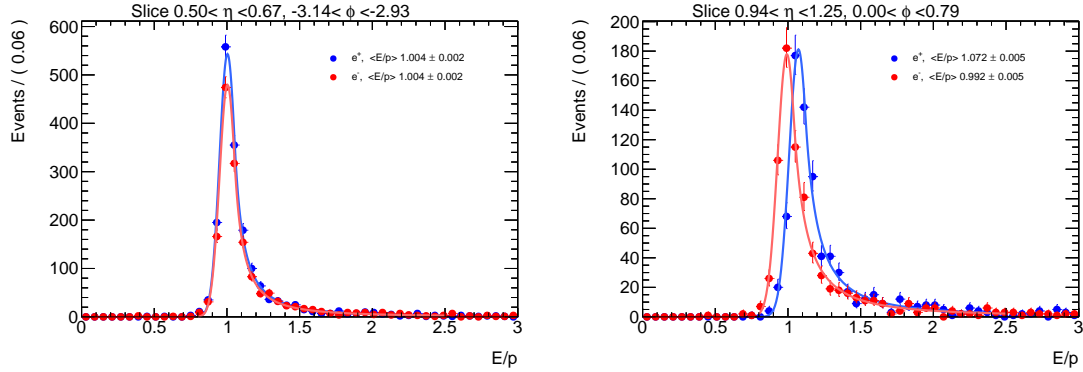


Figure 4.17: E/p distributions of electrons and positrons in two different $\eta\phi$ bins of the detector. The left hand plot is taken from a region with no momentum bias where $\langle E/p \rangle^+ = \langle E/p \rangle^-$, while the right hand plot shows an 8% disagreement in $\langle E/p \rangle$ between electrons and positrons.

Once the $\langle E/p \rangle^\pm$ distributions in each $\eta\phi$ bin have been extracted from the fits, a two dimensional map of δ_s can be constructed using Equation 4.17. The map gives an overview of sagitta biases that may be present in the detector, and can be used by the alignment algorithm to reduce the bias in the next iteration. In this case, the tracks fed to the alignment have their momenta corrected according to [33]:

$$q/p_{\text{corr}} = q/p_{\text{reco}}(1 - qp_T\delta_s) \quad (4.18)$$

where p_{reco} is the reconstructed momentum of the track. The corrected momentum is then constrained in the alignment.

⁷The Crystal Ball function is a probability density function consisting of a Gaussian core and a power-law tail.

972 **4.4.1.2 Results in 13 TeV data**

973 The E/p method has been used to monitor sagitta biases in the detector several times over the
974 course of Run 2. During this time, it has primarily served as an independent cross-check to a
975 second method using $Z \rightarrow \mu^\pm \mu^\mp$ events [33]. The $Z \rightarrow \mu^\pm \mu^\mp$ method identifies individual track
976 momentum biases through shifts in the reconstructed Z mass, which leaves it relatively insensitive
977 to global sagitta biases. For this reason, the sagitta bias maps produced using this technique are
978 normalized to those from the E/p method before being used to constrain the alignment.

979 The results of two implementations of the E/p method are presented here.

- 980 1. The first follows the end-of-year reprocessing of the entire ATLAS 2016 data set at $\sqrt{s} = 13$ TeV.
981 Two sets of alignment constants are compared: the *prompt* alignment, which was derived
982 shortly after each run was recorded, and the *reprocessed* alignment. The maps of the sagitta
983 bias comparing the two alignments calculated using the E/p method are shown in Figure 4.18,
984 and the comparison of the η projection of each map is shown in Figure 4.19.
- 985 2. The second uses the 2017 data after reprocessing, and compares the effects of multiple it-
986 erations of the method. In each iteration, the momenta of the electrons and positrons are
987 corrected based on Equation 4.15 using the value of δ_s computed in the previous iteration,
988 and a new sagitta bias map is calculated. If the method is indeed characterizing the sagitta
989 biases correctly, the corrections should converge quickly. The initial sagitta bias map is com-
990 pared to the map after two such iterations in Figure 4.20, and the sagitta bias projected along
991 η for each iteration is shown in Figure 4.21. Indeed, after just two iterations, δ_s is consistent
992 with zero in nearly all bins.

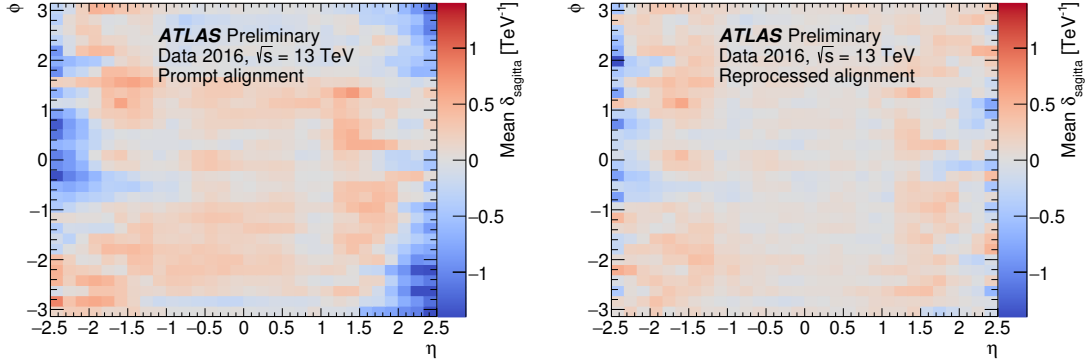


Figure 4.18: Sagitta bias in the $\sqrt{s} = 13$ TeV data collected by ATLAS in 2016 as a function of η and ϕ for the prompt (left) and reprocessed (right) alignments using the E/p method.

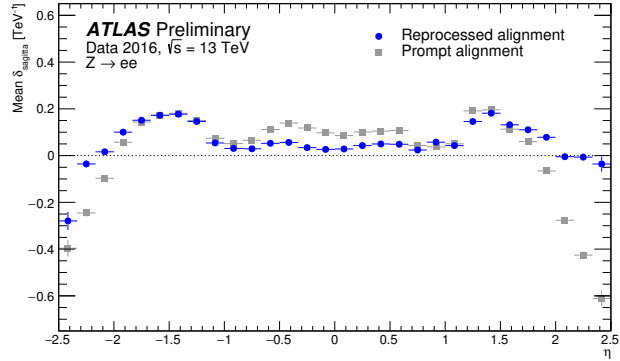


Figure 4.19: Sagitta bias in the $\sqrt{s} = 13$ TeV data collected by ATLAS in 2016 projected along η for the prompt (gray) and reprocessed (blue) alignments using the E/p method.

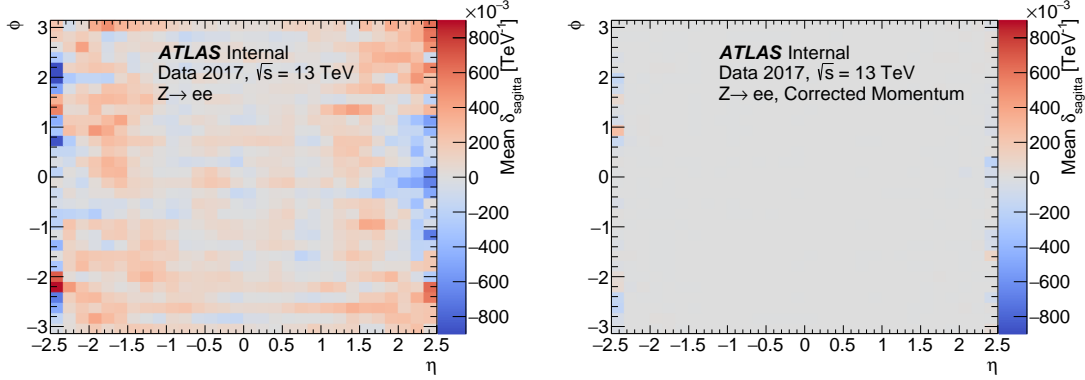


Figure 4.20: Sagitta bias in the $\sqrt{s} = 13$ TeV data collected by ATLAS in 2017 as a function of η and ϕ in reconstructed electrons (left) and after two iterations of momentum corrections (right) from the E/p method.

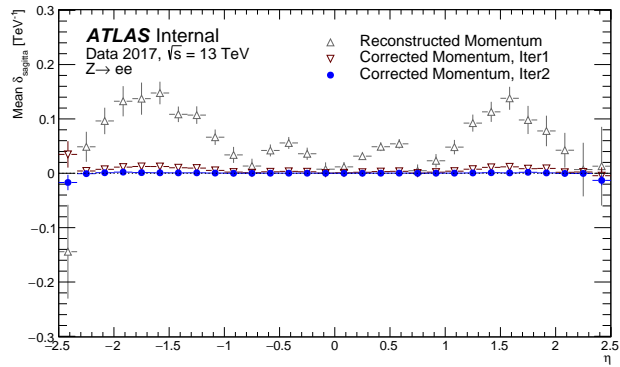


Figure 4.21: Sagitta bias in the $\sqrt{s} = 13 \text{ TeV}$ data collected by ATLAS in 2017 projected along η in reconstructed electrons (gray) and after one (red) and two (blue) iterations of momentum corrections from the E/p method.

CHAPTER 5

Measurement of same-sign WW production at $\sqrt{s} = 13$ TeV with ATLAS

996 Production of same-sign W boson pairs is a particularly interesting SM process. When produced
 997 via vector boson scattering (VBS), $W^\pm W^\pm jj$ is particularly sensitive to the electroweak symmetry
 998 breaking (EWSB) mechanism as well as potential “beyond the Standard Model” (BSM) physics.
 999 $W^\pm W^\pm jj$ events can be produced via electroweak-mediated (EWK) diagrams, of which VBS is a
 1000 subset, or QCD-mediated diagrams. The biggest advantage of same-sign $W^\pm W^\pm jj$ lies in its ratio
 1001 of electroweak (EWK) to QCD production cross sections. Despite the opposite-sign $W^\pm W^\mp$ having
 1002 a considerably larger total cross section, its EWK-mediated diagrams are considerably smaller than
 1003 its QCD-mediated diagrams, while for same-sign $W^\pm W^\pm$ the ratio is approximately one to one.
 1004 This makes $W^\pm W^\pm jj$ one of the best channels for studying VBS at the LHC.

1005 The first evidence of electroweak (EWK) $W^\pm W^\pm jj$ production was seen by the ATLAS and
 1006 CMS experiments at $\sqrt{s} = 8$ TeV with excesses of 3.6σ [36] and 2.0σ [37] over backgrounds,
 1007 respectively. More recently, ATLAS and CMS have both observed the EWK process at $\sqrt{s} = 13$ TeV
 1008 with significances of 6.9σ [38] and 5.5σ [39], respectively. The analysis presented in this chapter
 1009 is based off of the ATLAS $\sqrt{s} = 13$ TeV observation and cross section measurement of EWK
 1010 $W^\pm W^\pm jj$ production [38, 40].

1011 **5.0.2 Theoretical overview of vector boson scattering**

1012 VBS processes are very important to understand due to their sensitivity to the EWSB mechanism.
 1013 The scattering amplitude of longitudinally polarized vector bosons grows with center-of-mass energy
 1014 and ultimately violates unitarity above $\sqrt{s} = 1$ TeV in the absence of a light SM Higgs boson [41],

1015 [42]. However, once the Higgs is introduced, the divergences cancel and the cross section no longer
 1016 grows unbounded, as can be seen in Figure 5.1, which consists of plots from [43].

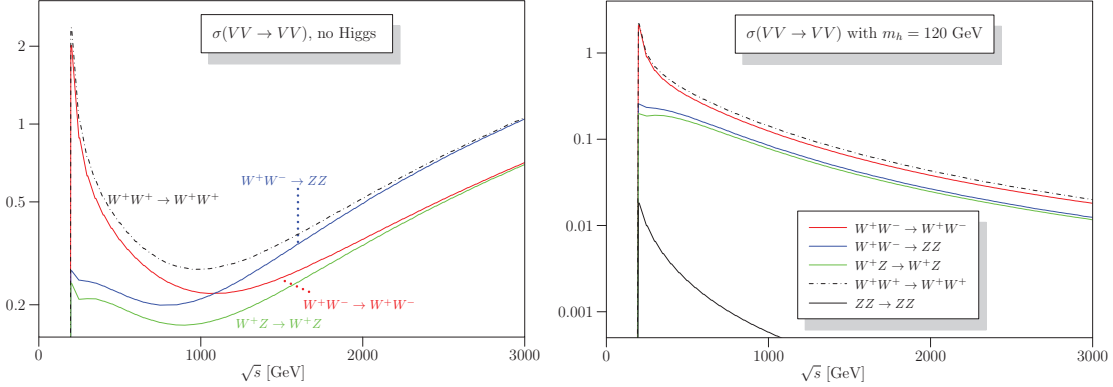


Figure 5.1: Cross sections in nanobarns for five different scattering processes of longitudinally polarized vector bosons as a function of center of mass energy \sqrt{s} . Without a SM Higgs boson (left), the cross sections grow unbounded with \sqrt{s} ; however with a 120 GeV Higgs boson (right), the cross sections no longer diverge. Plots taken from [43].

1017 With the discovery of the Higgs boson in 2012 [44, 45], the EWSB mechanism can now be directly
 1018 studied. Due to the exchange of a Higgs in the s - and t -channel VBS diagrams ($W^\pm W^\pm jj$ itself only
 1019 contains the t -channel diagram), VBS processes are directly sensitive to properties of the Higgs. For
 1020 example, the high-mass tail in the VV scattering system allows an approximation of the effective
 1021 coupling strength of the Higgs to vector bosons that is independent of any assumptions on the Higgs
 1022 width [46]. Additionally, the center of mass energy dependence of the VV scattering can reveal
 1023 whether the Higgs boson unitarizes the longitudinal scattering amplitude fully or only partially [47].

1024 VBS events are characterized by two quarks from the colliding protons each radiating a massive
 1025 vector boson which then scatter and decay in the detector. The incoming quarks carry a large
 1026 amount of momentum and only deflect a small amount upon radiating the vector boson; as a result,
 1027 they often travel very close to the beam line. Ignoring the decay products of the bosons, these VBS
 1028 events result in a final state of two vector bosons (V) and two jets (j) at high pseudorapidities
 1029 (called *forward jets*) from the outgoing quarks. The shorthand $VVjj$ is used to represent this final
 1030 state.

1031 $VVjj$ events can be produced via two different physical processes. The first involves purely
 1032 electroweak interactions in the tree-level diagrams, with $\mathcal{O}(\alpha_{EWK}) = 6$ and will be referred to as
 1033 *EWK production*. This can be further broken down into VBS and non-VBS production. In the
 1034 VBS EWK production, the scattering occurs via triple or quartic gauge couplings, as well as the

1035 s - or t -channel exchange of a Higgs boson. The non-VBS EWK production contains the same final
 1036 state of two vector bosons and two outgoing quarks, but the bosons do not scatter. Due to gauge
 1037 invariance, it is not possible to separate the VBS from the non-VBS productions [48]; therefore,
 1038 both are included in the signal generation and are indistinguishable from one another. The second
 1039 process involves a mix of the EWK and strong interactions, of order $\mathcal{O}(\alpha_s) = 2 \otimes \mathcal{O}(\alpha_{\text{EWK}}) = 4$ and
 1040 will be referred to as *QCD production*. The tree-level Feynman diagrams for VBS EWK, non-VBS
 1041 EWK, and QCD $VVjj$ production are found in Figures 5.2, 5.3, and 5.4, respectively.

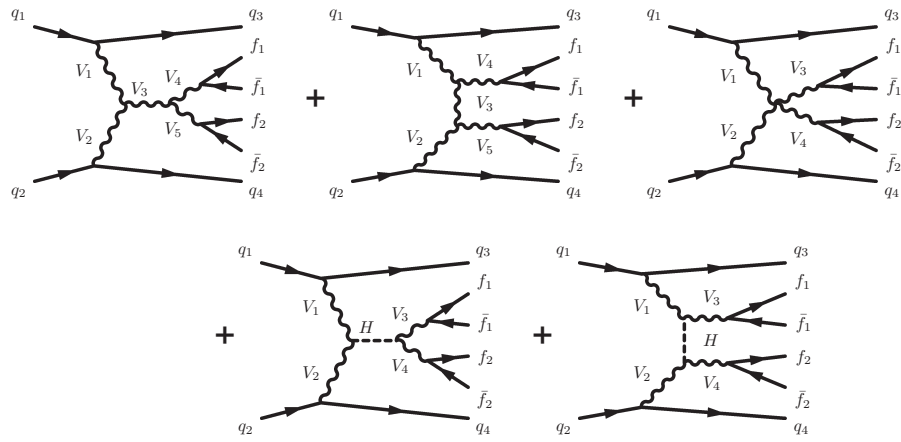


Figure 5.2: Tree-level Feynman diagrams for VBS EWK $VVjj$ production including triple gauge couplings involving W and/or Z bosons (top left and top middle), quartic gauge coupling (top right), or the exchange of a Higgs boson (s -channel bottom left and t -channel bottom right). The labels are quarks (q), fermions (f), and gauge bosons ($V = W, Z$).

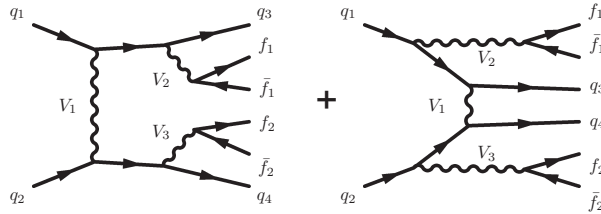


Figure 5.3: Tree-level Feynman diagrams for non-VBS EWK $VVjj$ production. The labels are quarks (q), fermions (f), and gauge bosons ($V = W, Z$).

1042 5.0.3 Same-sign $W^\pm W^\pm$ scattering

1043 Same-sign $W^\pm W^\pm jj$ scattering is considered to be one of the best channels for studying VBS at the
 1044 LHC [46]. This is due primarily to the ratio of the EWK to the QCD production, which matters

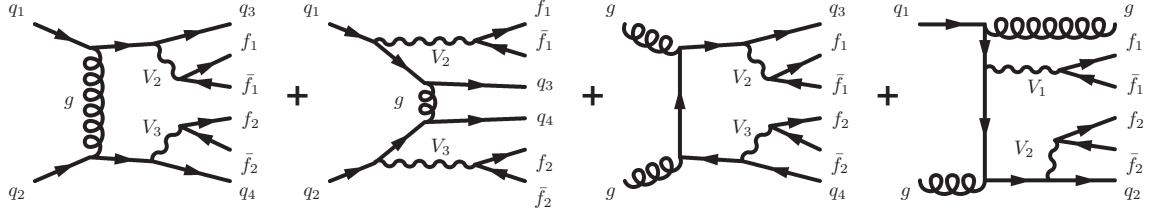


Figure 5.4: Tree-level Feynman diagrams for QCD $VVjj$ production. The labels are quarks (q), fermions (f), and gauge bosons ($V = W, Z$).

1045 a great deal due to the VBS events being a subset of the total EWK production. In an analysis
 1046 the EWK production would be considered the signal and the QCD production a background, so a
 1047 favorable ratio of the two helps greatly when comparing the size of the signal to the backgrounds.
 1048 A study at $\sqrt{s} = 8$ TeV [49] was done using the **SHERPA** Monte Carlo (MC) generator to calculate
 1049 EWK and QCD production cross sections at leading order for a variety of $VVjj$ processes decaying
 1050 to leptons and can be found in Table 5.1. Despite its lower cross section compared to other $VVjj$
 1051 processes, the EWK to QCD ratio for $W^\pm W^\pm jj$ is approximately one-to-one, whereas for opposite-
 1052 sign $W^\pm W^\mp jj$ the ratio is closer to 3%.

Process	Final state	σ_{EWK}	σ_{QCD}
$W^\pm W^\pm$	$l^\pm l^\pm \nu\nu jj$	19.5 fb	18.8 fb
$W^\pm W^\mp$	$l^\pm l^\mp \nu\nu jj$	91.3 fb	3030 fb
$W^\pm Z$	$l^\pm l^\pm l^\mp \nu jj$	30.2 fb	687 fb
ZZ	$l^+ l^- \nu\nu jj$	2.4 fb	162 fb
ZZ	$l^+ l^- l^+ l^- jj$	1.5 fb	106 fb

Table 5.1: Predicted cross sections for EQK and QCD production of diboson processes relevant to VBS at $\sqrt{s} = 8$ TeV using the **SHERPA** MC generator. Loose generator level cuts are applied on lepton $p_T > 5$ GeV, dilepton invariant mass $m_{ll} > 4$ GeV, and at least two jets with $m_{jj} > 10$ GeV. Numbers taken from [49].

1053 This analysis studies $W^\pm W^\pm jj$ scattering where both W bosons decay leptonically to $e\nu$ or $\mu\nu$ ⁸.
 1054 The $W^\pm W^\pm jj$ VBS final state consists of two leptons with the same electric charge, two neutrinos,
 1055 and two high energy forward jets with a large invariant mass. Tree-level Feynman diagrams of VBS
 1056 $W^\pm W^\pm jj$ production can be found in Figure 5.5 and a visual representation of the VBS topology
 1057 can be found in Figure 5.6. The two forward jets also serve as a powerful tool to suppress the
 1058 QCD production mode. In EWK events, the two jets tend to have much higher separation and a
 1059 larger combined invariant mass than the two leading jets in a QCD event. The two plots shown in

⁸Throughout the rest of this chapter, l denotes either electrons (e) or muons (μ) unless stated otherwise. Additionally, e , μ , and ν (neutrino) with no charge or anti-particle designation refer interchangeably to either the particle or anti-particle.

1060 Figure 5.7 highlight the differences in these dijet quantities between the two production modes. An
 1061 ATLAS event display of a real $W^\pm W^\pm jj$ candidate event is shown in Figure 5.8.

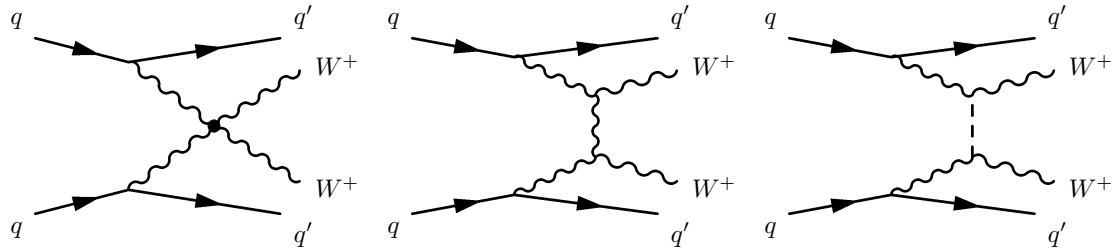


Figure 5.5: Feynman diagrams for VBS EWK production of $W^\pm W^\pm jj$ events. The leftmost diagram contains a quartic gauge coupling vertex, and the rightmost diagram contains an exchange of a Higgs boson. **TODO: Make diagrams consistent with others**

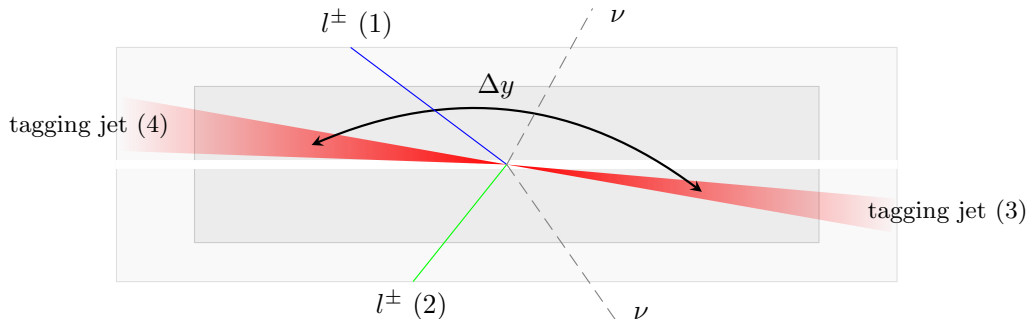


Figure 5.6: $W^\pm W^\pm jj$ VBS event topology containing two leptons (1 and 2) with the same electric charge, two neutrinos, and two forward tagging jets (3 and 4) with large rapidity separation Δy .

1062 5.0.4 Overview of backgrounds

1063 In addition to QCD production of $W^\pm W^\pm jj$ events, there are several other processes that can end
 1064 up with a final state of two same-sign leptons, two neutrinos, and two jets. However, due to the ± 2
 1065 final state charge, there is a considerable reduction in SM backgrounds (such as Z boson events)
 1066 when compared to an analysis like opposite-sign $W^\pm W^\mp jj$.

1067 One of the largest sources of background involves processes with prompt leptons⁹. These are
 1068 events that contain two leptons with the same electric charge and one or more additional leptons

⁹Prompt leptons are those that are produced in the primary collision and are a direct decay product of the process of interest. Non-prompt leptons originate from some secondary process, such as a b -hadron decay, or are jets that get mis-reconstructed as a lepton.

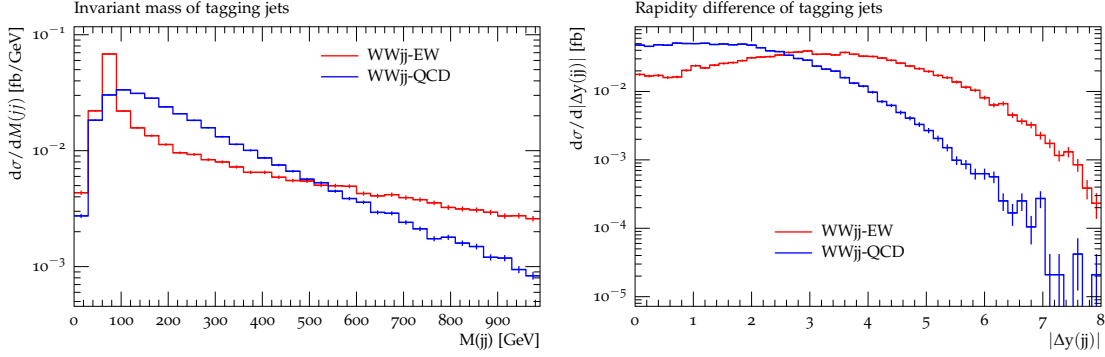


Figure 5.7: Generator level comparisons at $\sqrt{s} = 8$ TeV of dijet invariant mass (m_{jj} , left) and dijet rapidity (Δy_{jj} , right) in EWK (red) and QCD (blue) $W^\pm W^\pm jj$ events. Both data sets have been normalized to the same area. Plots taken from [49].

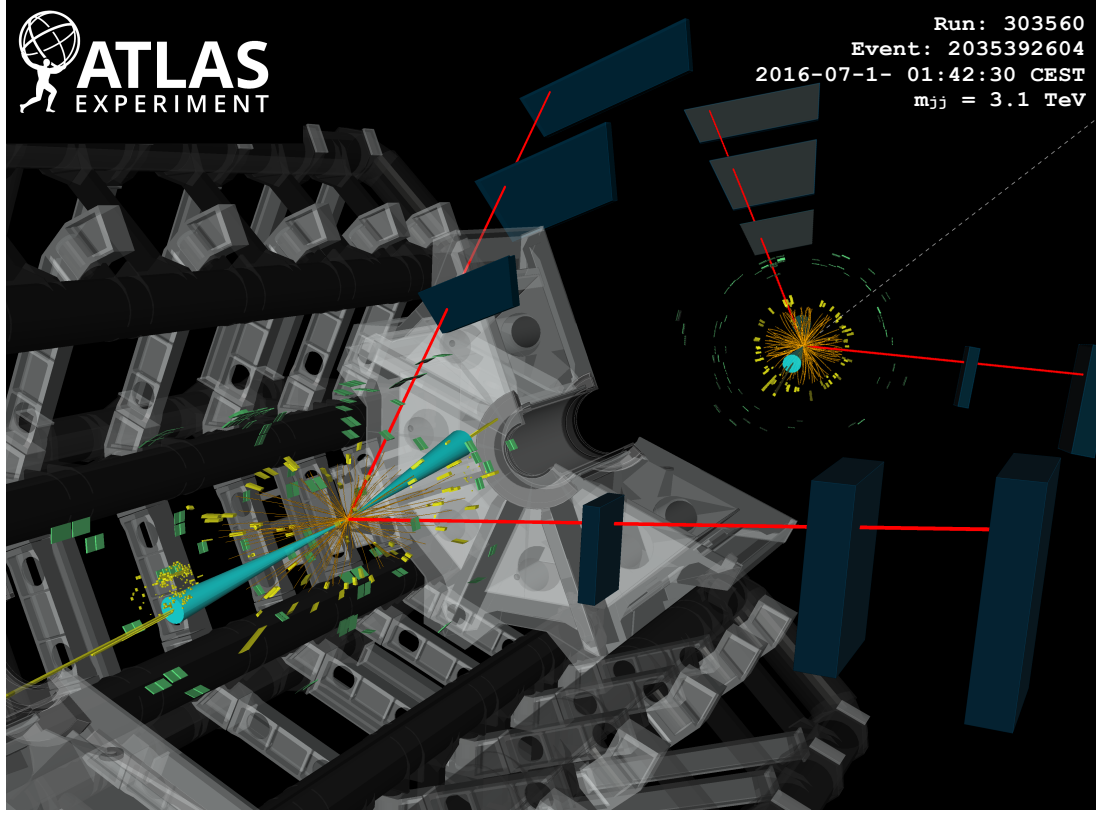


Figure 5.8: ATLAS event display of a $pp \rightarrow W^+ W^+ \rightarrow \mu^+ \nu_\mu \mu^+ \nu_\mu jj$ event. The muons are represented by the red lines travelling from the ID through the MS, and the forward jets are represented by the blue cones with yellow energy deposits in the calorimeters. The direction of the E_T^{miss} in the transverse plane is indicated by the gray dashed line in the inset image. Event display taken from [38].

that are “lost”, either by failing the selection criteria or falling outside of the detector’s acceptance. The number of processes that can contribute is limited by the requirement of same-sign leptons, and as a result this background is dominated by processes involving two or more vector bosons, with the largest contribution coming from WZ events and smaller contributions from ZZ and $t\bar{t}V$ events. Triboson events where one boson decays hadronically also contribute to this background; however, the jets are generally softer and more central than in a typical VBS event, and the cuts applied on the forward jets suppress these contributions.

The other dominant background comes from non-prompt, or “fake”, leptons. Here one or more leptons originate from the decay of another particle unrelated to the signal process, such as a heavy-flavor decay or photon conversion, or come from a jet that is misidentified as a lepton. This background is mostly made up of events from $t\bar{t}$ and $W+\text{jets}$ processes, with a much smaller contribution from $V\gamma$ events. **TODO: check whether $V\gamma$ really qualifies as non-prompt, we lump $Z\gamma$ in with the charge flip background in the paper...**

Finally, opposite-sign lepton pairs can enter the signal region if one of the leptons is reconstructed with the wrong charge (called *charge misidentification*¹⁰). In practice, this only affects events with electrons, as the charge misidentification rate for muons is negligible [50]. This is a major background in events with two electrons, but is a much smaller contribution for events with one electron and one muon.

5.1 Data and Monte Carlo samples

This analysis uses 36.1 fb^{-1} of $\sqrt{s} = 13$ TeV proton-proton collision data recorded by ATLAS during 2015 and 2016. The uncertainty in the combined integrated luminosity is 2.1%. It is derived following a methodology similar to that detailed in [51] and using the LUCID-2 detector for the baseline luminosity measurements [52] from calibration of the luminosity scale using x - y beam-separation scans.

5.1.1 Monte Carlo samples

A number of Monte Carlo (MC) simulations are employed to model signal and background processes. In order to model the real collision data as closely as possible, each MC has been run through a full simulation of the ATLAS detector [53] in GEANT4 [54], and events have been reconstructed

¹⁰Charge misidentification is also referred to interchangeably as *charge mis-ID* and *charge flip*.

1097 using the same algorithms as the data. The simulation reproduces as closely as possible the momentum
 1098 resolutions and calorimeter responses of the detector, and also includes the effects of pileup by
 1099 including soft QCD interactions using PYTHIA v8.1 [55]. The MC samples used in this analysis are
 1100 detailed in this section and summarized in Table 5.2.

1101 The $W^\pm W^\pm jj$ samples are modeled using SHERPA v2.2.2 [56, 57, 58] with the NNPDF3.0 PDF
 1102 set [59]. The EWK signal samples are generated by fixing the electroweak coupling constant to
 1103 $\mathcal{O}(\alpha_W) = 6$, and a QCD background sample was also generated with $\mathcal{O}(\alpha_W) = 4$. SHERPA includes
 1104 up to one parton at next-to-leading order (NLO) and up to three at leading order (LO) in the
 1105 strong coupling constant α_s . A second $W^\pm W^\pm jj$ EWK sample is generated using POWHEG-BOX
 1106 v2 [60] with the NNPDF3.0 PDF set and at NLO accuracy. This sample is only used for systematic
 1107 studies, as POWHEG-BOX does not include resonant triboson contributions in its matrix element, which
 1108 are non-negligible at NLO [61].

1109 Diboson processes (VV where $V = W, Z$) are simulated with SHERPA v2.2.2 for mixed hadronic
 1110 and leptonic decays and SHERPA v2.2.1 for fully leptonic decays of the bosons. Similarly, triboson
 1111 (VVV) and $V\gamma$ processes are simulated using SHERPA v2.1.1 with up to one parton at NLO and up
 1112 to three at LO. $W+jets$ processes are simulated with SHERPA2.2.1 with up to two partons at NLO
 1113 and four at LO. All the above SHERPA samples use the NNPDF3.0 PDF set and SHERPA's own parton
 1114 showering. The $Z+jets$ events are generated with Madgraph5_aMC@NLO [62] at LO and interfaced
 1115 with PYTHIA v8.1 for parton showering.

1116 $t\bar{t}$ events are generated using POWHEG-BOX v2 with the CT10 PDF set [63]. $t\bar{t}V$ samples are
 1117 generated at NLO with Madgraph5_aMC@NLO and the NNPDF3.0 PDF set interfaced with PYTHIA v8
 1118 for parton showering. Finally, single top events are generated with POWHEG-BOX v1 and the CT10f4
 1119 PDF set interfaced with PYTHIA v6 [64] for parton showering.

1120 5.2 Object and event selection

1121 This section details the selection criteria for objects used in the analysis as well as the selection for
 1122 signal events.

1123 5.2.1 Object selection

1124 Muons, electrons, and jets all must pass strict selection requirements to ensure that only high quality,
 1125 well measured objects are used. For leptons, a baseline selection is defined (called the *preselection*),
 1126 which all leptons must pass in order to be considered for the analysis. This preselection is an

Process	Generator	Comments
$W^\pm W^\pm jj$ (EWK)	SHERPA v2.2.2	Signal sample
$W^\pm W^\pm jj$ (EWK)	POWHEG-BOX v2	Systematics sample
$W^\pm W^\pm jj$ (QCD)	SHERPA v2.2.2	
Diboson	SHERPA v2.2.2	Both bosons decay leptonically ($llll$, $lll\nu$, $ll\nu\nu$)
Triboson	SHERPA v2.2.1	One boson decays leptonically, the other hadronically
$W + \text{jets}$	SHERPA v2.2.1	
$Z + \text{jets}$	Madgraph5_aMC@NLO	
$V\gamma$	SHERPA v2.1.1	
$V\gamma jj$ (EWK)	SHERPA v2.2.4	
$t\bar{t}V$	Madgraph5_aMC@NLO	
$t\bar{t}$	POWHEG-BOX v2	
Single top	POWHEG-BOX v1	EWK t -, s -, & Wt -channels

Table 5.2: Summary of MC samples used in the analysis.

intentionally loose set of criteria in order to have high acceptance for rejecting backgrounds with additional leptons (i.e. $WZ \rightarrow 3l\nu jj$). Signal leptons are then required to satisfy a much tighter *signal selection* aimed at suppressing backgrounds from non-prompt or fake leptons. A third set of lepton selection criteria, the *loose selection*, defines a sample enriched in non-prompt leptons, and it is used in the fake factor method for estimating the non-prompt background, discussed in detail in Section 5.3.4. Jets are only required to pass one set of selection criteria. These selections are detailed in the following sections and summarized in Table 5.3 for muons, Table 5.4 for electrons, and Table 5.5 for jets.

5.2.1.1 Muon candidate selection

Cuts on muon p_T serve to reject low momentum leptons from background processes and additional collisions from pileup events. Preselected muons must have $p_T > 6$ GeV and signal muons $p_T > 27$ GeV. The p_T requirement for loose muons is lower than for signal muons, $p_T > 15$ GeV, for reasons that are discussed in Section 5.3.4. **TODO:** reference proper subsection when it's done

Muons are required to fall within the detector's η acceptance: $|\eta| < 2.7$ for preselected muons, which is tightened to $|\eta| < 2.5$ for the signal muons.

Cuts on the transverse and longitudinal impact parameters are applied to ensure that the candidate muon originated from the primary particle interaction and not some other source, such as a heavy flavor decay. The preselection and the loose selection both have looser requirements on the transverse impact parameter significance (d_0/σ_{d_0}) than the signal selection; all three have the same requirement on the transverse impact parameter ($|z_0 \times \sin \theta|$).

Finally, the muon candidates are required to pass a particle identification and an isolation criteria as defined in [65]. The methods used in constructing the identification and isolation workingpoints are described in more detail in Section 3.2.4.2. The muon identification serves to select prompt muons with high efficiency and well measured momenta. This analysis uses two different workingpoints, **Loose** for preselected muons and **Medium** for loose and signal muons, where **Medium** muons are a tighter subset of those that pass the **Loose** requirement. Muon isolation is a measurement of detector activity around the muon candidate, and it is measured with both track-based and calorimeter-based variables. The isolation workingpoint used for the signal muons, **Gradient**, is defined such that there is 90% or better background rejection efficiency for 25 GeV muons, and 99% efficiency at 60 GeV. There is no minimum isolation requirement for preselected or loose muons. Loose muons are additionally required to fail one or both of the signal transverse impact parameter cut and signal isolation requirement.

Muon preselection	
Momentum cut	$p_T > 6$ GeV
Angular acceptance	$ \eta < 2.7$
Longitudinal impact parameter	$ z_0 \times \sin \theta < 0.5$ mm
Transverse impact parameter	$d_0/\sigma_{d_0} < 10$
Particle identification	Loose

Muon signal selection	
Momentum cut	$p_T > 27$ GeV
Angular acceptance	$ \eta < 2.5$
Longitudinal impact parameter	$ z_0 \times \sin \theta < 0.5$ mm
Transverse impact parameter	$d_0/\sigma_{d_0} < 3$
Particle identification	Medium
Particle isolation	Gradient

Muon loose selection	
Momentum cut	$p_T > 15$ GeV
Angular acceptance	$ \eta < 2.5$
Longitudinal impact parameter	$ z_0 \times \sin \theta < 0.5$ mm
Transverse impact parameter	$d_0/\sigma_{d_0} < 10$
Particle identification	Medium
Fail signal transverse impact parameter and/or isolation cuts	

Table 5.3: Muon selection criteria. All muons are required to pass the preselection (top), and then either the signal (middle) or loose (bottom) criteria is applied to the preselected electrons.

1159 **5.2.1.2 Electron candidate selection**

1160 The electron candidate selections are very similar to those for muons. The p_T cut starts at $p_T >$
 1161 6 GeV for the preselection, increases to $p_T > 20$ GeV for loose electrons, and finally to $p_T > 27$ GeV
 1162 for signal electrons. The $|\eta|$ cut for electrons requires $|\eta| < 2.47$ for all electrons, with the region
 1163 $1.37 \leq |\eta| \leq 1.52$ removed from loose and signal electrons. This region is where the electromagnetic
 1164 calorimeter transitions from the barrel to the endcaps and is not fully instrumented. Both the
 1165 transverse and longitudinal impact parameter cuts are the same for all electron selections.

1166 The electron particle identification uses a multivariate likelihood technique (LH) [66] detailed
 1167 in Section 3.2.4.3. Preselected electrons must pass the loosest LH workingpoint `LooseLH` with
 1168 an additional requirement that there be a reconstructed track hit in the first layer of the pixel
 1169 detector (a so-called *B*-layer hit). The LH requirement for the loose and signal electrons the tightness
 1170 of the identification using `MediumLH` and `TightLH`, respectively. As for isolation, the `Gradient`
 1171 workingpoint is required for signal electrons only. The loose electrons must fail one or both of the
 1172 signal identification and isolation requirements.

1173 **5.2.1.3 Jet candidate selection**

1174 The final objects that need to pass selection are jets. Jets are clustered using the anti- k_t algo-
 1175 rithm [67] within a radius of $\Delta R = 0.4$. The jets are then calibrated using E_T - and η -dependent
 1176 correction factors that are trained using MC simulations [68]. These calibrated jets are then re-
 1177 quired to have $p_T > 30$ GeV if they lie in the forward regions of the detector ($2.4 < |\eta| < 4.5$) and
 1178 $p_T > 25$ GeV in the central region ($|\eta| \leq 2.4$). In order to suppress pileup jets, the so-called jet-
 1179 vertex-tagger (JVT) discriminant associates a jet with the primary interaction vertex [69]; central
 1180 jets with $p_T > 60$ GeV are required to pass the `Medium` JVT workingpoint, which corresponds to
 1181 an average efficiency of over 92%. Finally, the jets are required to be separated by selected prompt
 1182 leptons by at least $\Delta R(j, l) > 0.3$.

1183 **5.2.1.4 Treatment of overlapping objects**

1184 In the event that one or more objects are reconstructed very close to each other, there is the
 1185 possibility for double-counting if both originated from the same object. The procedure by which
 1186 this ambiguity is resolved is called *overlap removal* (OR). The standard ATLAS recommendation
 1187 for OR is implemented in this analysis [70, 71] and is summarized in Table 5.6.

Electron preselection	
Momentum cut	$p_T > 6$ GeV
Angular acceptance	$ \eta < 2.47$
Longitudinal impact parameter	$ z_0 \times \sin \theta < 0.5$ mm
Transverse impact parameter	$d_0/\sigma_{d_0} < 5$
Particle identification	LooseLH + B-layer hit

Electron signal selection	
Momentum cut	$p_T > 27$ GeV
Angular acceptance	$ \eta < 2.47$, excluding $1.37 \leq \eta \leq 1.52$
Longitudinal impact parameter	$ z_0 \times \sin \theta < 0.5$ mm
Transverse impact parameter	$d_0/\sigma_{d_0} < 5$
Particle identification	TightLH
Particle isolation	Gradient

Electron loose selection	
Momentum cut	$p_T > 20$ GeV
Angular acceptance	$ \eta < 2.47$, excluding $1.37 \leq \eta \leq 1.52$
Longitudinal impact parameter	$ z_0 \times \sin \theta < 0.5$ mm
Transverse impact parameter	$d_0/\sigma_{d_0} < 5$
Particle identification	MediumLH
Fail signal identification and/or isolation cuts	

Table 5.4: Electron selection criteria. All electrons are required to pass the preselection (top), and then either the signal (middle) or loose (bottom) criteria is applied to the preselected electrons.

Jet selection	
Momentum cut	$p_T > 30$ GeV for $2.4 < \eta < 4.5$ $p_T > 60$ GeV for $ \eta < 2.4$
JVT cut	Medium
Jet-lepton separation	$\Delta R(j, l) > 0.3$

Table 5.5: Jet selection criteria. All jets are required to pass the above selection in order to be used in the analysis.

1188 Since electrons leave a shower in the EM calorimeter, every electron has a jet associated with
 1189 it. Therefore, any jets close to an electron (within $\Delta R(e, j) < 0.2$) are rejected due to the high
 1190 probability that they are the same object. On the other hand, when jets and electrons overlap
 1191 within a large radius of $0.2 < \Delta R(e, j) < 0.4$, it is likely that the electron and jet both are part of
 1192 a heavy-flavor decay, and the electron is rejected.

1193 High energy muons can produce photons via bremsstrahlung radiation or collinear final state
 1194 radiation which results in a nearby energy deposit in the calorimeters. Non-prompt muons from
 1195 hadronic decays produce a similar signature; however, in this case the jet has a higher track multiplicity
 1196 in the ID. It is possible to address both cases by rejecting the jet when the ID track multiplicity
 1197 is less than three and otherwise rejecting the muon for jets and muons within $\Delta R(\mu, j) < 0.4$.

1198 In addition to the case above where muon bremsstrahlung results in a nearby reconstructed jet,
 1199 the ID track from the muon and the calorimeter energy deposit can lead to it being reconstructed
 1200 as an electron. In this case, if both a muon and an electron share a track in the ID, the muon is
 1201 kept and the electron is rejected, unless the muon is calorimeter-tagged¹¹, in which case the muon
 1202 is removed in favor of the electron.

Overlap	Check	Result (remove → keep)
Electron & Jet	$\Delta R(e, j) < 0.2$	Jet → electron
	$0.2 < \Delta R(e, j) < 0.4$	Electron → jet
Muon & Jet	$\Delta R(\mu, j) < 0.4$ and Jet N_{ID} tracks < 3	Jet → muon
	$\Delta R(\mu, j) < 0.4$ and Jet N_{ID} tracks ≥ 3	Muon → jet
Electron & Muon	Shared ID track	Electron → muon
	Shared ID track & muon is calo-tagged	Muon → electron

Table 5.6: Summary of the overlap removal procedure used in the analysis. If the criteria in the “check” column is met, in the “result” column, the object on the left of the arrow is removed in favor of the object on the right.

1203 5.2.2 Signal event selection

1204 After the objects have been selected, cuts are applied on a per-event level to select $W^\pm W^\pm jj$ signal
 1205 events. The event selection is summarized in Table 5.8 and is detailed in this section. It includes
 1206 the results of an optimization performed using a multidimensional grid scan.

1207 The initial event selection begins by choosing events that pass one or more of the trigger re-
 1208 quirements listed in Table 5.7. At least one signal lepton is “matched” to a passed trigger in order

¹¹A calorimeter-tagged (CT) muon is a muon that is identified by matching an ID track to a calorimeter energy deposit. CT muons have relatively low reconstruction efficiency compared to those measured by the MS, but can be used to recover acceptance in regions of the detector where the MS does not have full coverage [65].

to ensure that it was indeed a signal lepton that fired the trigger. A collection of *event cleaning* cuts must also be passed in order to remove events collected during periods in which one or more components of the detector was not operating optimally. Finally, the events are required to contain at least one interaction vertex. An event can have multiple reconstructed vertices from additional proton-proton collisions that occurred in the same bunch crossing. In this case, the *primary vertex* is determined by choosing the vertex with the largest sum of the p_T^2 of its associated tracks.

	2015 data	2016 data
Electrons	$p_T > 24$ GeV and Medium ID	$p_T > 26$ GeV and Tight ID and Loose isolation
	$p_T > 60$ GeV and Medium ID	$p_T > 60$ GeV and Medium ID
	$p_T > 120$ GeV and Loose ID	$p_T > 140$ GeV and Loose ID
Muons	$p_T > 20$ GeV and Loose isolation $p_T > 50$ GeV	$p_T > 26$ GeV and Medium isolation $p_T > 50$ GeV

Table 5.7: Summary of trigger requirements for electrons and muons for $\sqrt{s} = 13$ TeV data collected in 2015 and 2016. At least one of the triggers must be satisfied.

Events are then required to contain exactly two signal leptons with the same electric charge. The dilepton pair must have a combined invariant mass of $m_{ll} \geq 20$ GeV in order to suppress low mass Drell-Yan backgrounds. Two additional selections are applied to events in the ee -channel: both electrons are required to have $|\eta| < 1.37$ with an invariant mass at least 15 GeV away from the Z -boson mass to reduce events where one electron is reconstructed with the wrong charge (this background will be discussed in more detail in Section 5.3 TODO: Replace with proper subsection once it's written). To suppress backgrounds from events with more than two leptons, events with more than two leptons passing the preselection are vetoed.

Missing transverse energy (E_T^{miss}) represents any particles that escape the detector without being measured, such as neutrinos, and is defined as the magnitude of the vector sum of transverse momenta of all reconstructed objects. It can be difficult to calculate accurately, as it involves measurements from all subsystems within the detector, and it is sensitive to any corrections that may be applied to the reconstructed physics objects [72]. These corrections, including the momentum smearing for muons, energy scale and smearing for electrons, and jet calibrations, are propagated to the E_T^{miss} calculation. Events are required to contain $E_T^{\text{miss}} > 30$ GeV in order to account for the two neutrinos from the W boson decays.

At least two jets are required. The leading and subleading jets must have $p_T > 65$ GeV and $p_T > 35$ GeV, respectively, and are referred to as the *tagging jets*. Events are vetoed if they contain one or more jets that have been tagged as a b -jet to suppress backgrounds from heavy flavor decays

1234 (especially top quark events). The b -tagging algorithm used by ATLAS is a boosted decision tree
1235 (BDT) called MV2c10, and this analysis uses a workingpoint with 85% efficiency [73].

1236 Finally, cuts are applied on the VBS signature outlined in Section 5.0.3. The tagging jets are
1237 required to have a dijet invariant mass $m_{jj} > 200$ GeV and be separated in rapidity by $|\Delta y_{jj}| > 2.0$.
1238 This preferentially selects the VBS EWK events over the QCD-produced $W^\pm W^\pm jj$ events.

Event selection	
Event preselection	Pass at least one trigger with a matched lepton Pass event cleaning At least one reconstructed vertex
Lepton selection	Exactly two leptons passing signal selection Both signal leptons with the same electric charge $ \eta < 1.37$ and $ M_{ee} - M_Z > 15$ GeV (ee -channel only) Veto events with more than two preselected leptons
Missing transverse energy	$E_T^{\text{miss}} \geq 30$ GeV
Jet selection	At least two jets Leading jet $p_T > 65$ GeV Subleading jet $p_T > 35$ GeV $m_{jj} > 200$ GeV $N_{b\text{-jet}} = 0$ $ \Delta y_{jj} > 2.0$

Table 5.8: The signal event selection.

1239 5.3 Background estimations

1240 The major sources of background events are summarized in Section 5.0.4, and the methods used to
1241 estimate them are detailed in this section. Prompt backgrounds from ZZ and $t\bar{t}V$ are estimated
1242 directly from MC simulations. The shape of the WZ and $V\gamma$ backgrounds are taken from MC, and
1243 the predicted yeilds are normalized to the data predictions in dedicated control regions, as outlined
1244 in Sections 5.3.1 and 5.3.2, respectively. Opposite sign events with a charge misidentified electron
1245 are estimated by a data-driven background method which is summarized in Section 5.3.3. Finally, a
1246 *fake factor* method is used to estimate the contributions from non-prompt backgrounds and is the
1247 subject of Section 5.3.4.

1248 5.3.1 Estimation of the WZ background

1249 The dominant background involving prompt leptons comes from $WZ + \text{jets}$ events. The contribution
1250 is estimated from MC simulation and normalized to data in a control region enriched in WZ events

defined by the same event selection as Table 5.8 for the signal region, with the following changes applied to increase the purity of the WZ process:

- The third lepton veto is inverted, requiring a third lepton with $p_T > 15$ GeV
- Two of the leptons must make a same-flavor opposite-sign pair. If more than one pair exists, the one with m_{ll} closest to the Z boson mass is chosen.
- The trilepton invariant mass is required to be $m_{lll} > 106$ GeV to reduce contributions from $Z\gamma$ and $Z+jets$

Once the event yields in the control region are calculated, they are propagated to the final signal region fit, detailed in Section 5.4.1, in a single bin combining all the lepton channels. The systematic uncertainties of the WZ background are also calculated at this time. The event yields for the WZ control region are listed in Table 5.9, and distributions of the leading lepton p_T and η as well as trilepton invariant mass m_{lll} are found in Figures 5.10 and 5.9, respectively.

Event yields in the WZ control region	
WZ	197.9 ± 1.4
ZZ	14.1 ± 0.3
Triboson	1.26 ± 0.1
top	10.8 ± 1.1
$Z\gamma$	3.1 ± 1.1
$Z+jets$	2.5 ± 1.4
Total prediction	229.7 ± 2.5
Data	201 ± 14.2

Table 5.9: Event yields in the WZ control region before normalization. All lepton flavor channels are combined.

5.3.2 Estimation of the $V\gamma$ background

Events from $V\gamma$ processes can pass selection if the photon converts into an e^+e^- pair and one of the electrons passes the selection criteria. The background is estimated from MC simulations which are then scaled by a normalization factor calculated from a control region enriched in $Z(\mu^+\mu^-)\gamma$ events. This control region selects two opposite-sign muons and an additional electron that is assumed to come from the photon conversion. The full event selection is detailed in Table 5.10.

The $Z\gamma$ MC samples available do not cover the full range of p_T^γ and $\Delta R(\gamma, l)$; thus, additional Drell-Yan samples ($Z+jets$) are used to fill out the phase space. Overlap between the two samples

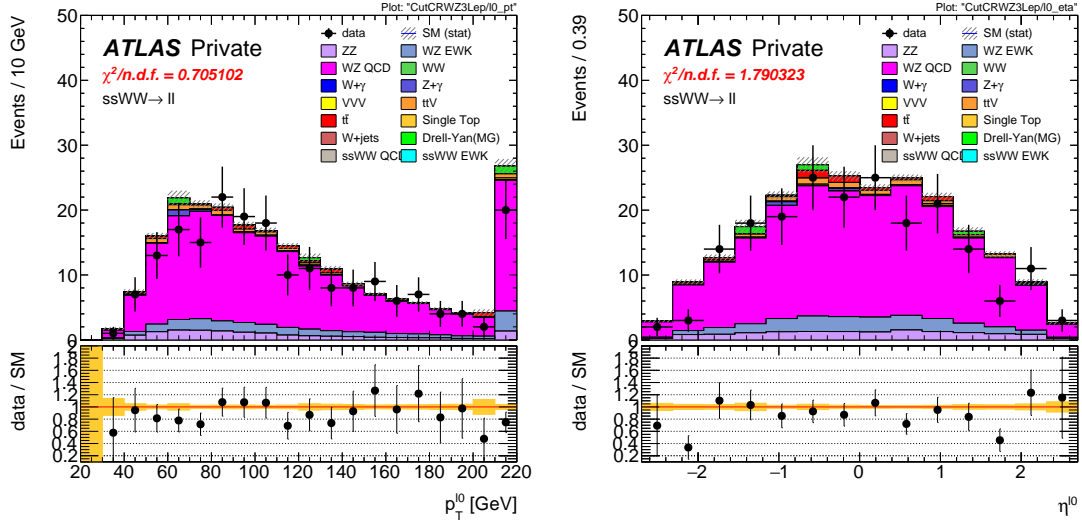


Figure 5.9: Leading lepton p_T (left) and η (right) distributions in the WZ control region before normalization. All lepton channels are combined.

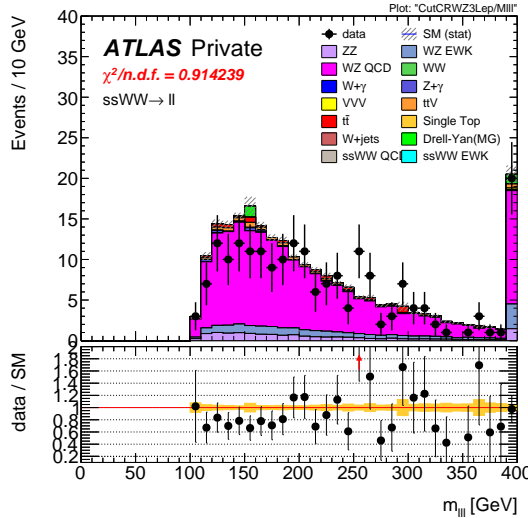


Figure 5.10: Trilepton invariant mass m_{lll} distribution in the WZ control region before normalization. All lepton channels are combined.

$V\gamma$ control region
Exactly two muons with $p_T > 27$ GeV and $p_T > 20$ GeV
Exactly one additional electron with $p_T > 15$ GeV
Remove overlap between $Z+jets$ and $Z\gamma$
Di-muon + photon invariant mass $75 < M_{\mu\mu\gamma} < 100$ GeV
$E_T^{\text{miss}} < 30$ GeV

Table 5.10: Selection criteria for the $V\gamma$ control region.

are removed based to avoid double counting. Events with final state photons at truth level are checked to ensure that the photon did not originate from a hadronic decay. Cuts on $p_T^\gamma > 10$ GeV and $\Delta R(\gamma, l) > 0.1$ are then applied at generator level, and $Z\gamma$ events that fail and $Z+jets$ events that pass this additional selection are removed.

The normalization factor is calculated directly from the event yields in the $V\gamma$ control region rather than in the signal fit, as is done for the WZ background. The event yields are listed in Table 5.11, and the normalization factor is determined to be 1.77. No MC events from $Z\gamma$ processes survive the full event selection; thus, the scaling is only applied to the $W\gamma$ background in the signal region. A systematic uncertainty of 44% is assigned to the background based off of the uncertainties in the calculation of the normalization factor.

Event yields in the $V\gamma$ control region	
$Z\gamma$	24.6 ± 3.3
$Z+jets$	3.0 ± 1.5
diboson + triboson	6.7 ± 0.3
top	1.5 ± 0.5
Total prediction	35.8 ± 3.7
Data	57 ± 7.6

Table 5.11: Event yields in the $V\gamma$ control region. The $V\gamma$ scale factor of 1.77 is calculated by scaling up the $Z\gamma$ and $Z+jets$ backgrounds to account for the difference between the data and predicted total background.

5.3.3 Estimation of backgrounds from charge misidentification

If an electron's charge is mis-reconstructed, it can lead to a real, opposite-sign lepton pair passing the same-sign requirement in the event selection. There are two primary reasons this can occur:

1. An electron emits a photon via bremsstrahlung which then converts into an electron-positron pair, and the conversion track with the wrong electric charge is matched to the original electron. This is the dominant process leading to charge flip, and it is highly dependent on the electron η due to the different amount of detector material the electron passes through.
2. The curvature of the electron's track is mismeasured, resulting in the wrong charge being assigned. This process is dependent on the momentum of the electron, as its track becomes more straight as the momentum of the electron increases.

In order to estimate this background, the rate at which an electron's charge is misidentified is calculated from $Z \rightarrow e^+e^-$ MC simulation. It is known that the MC does not perfectly model

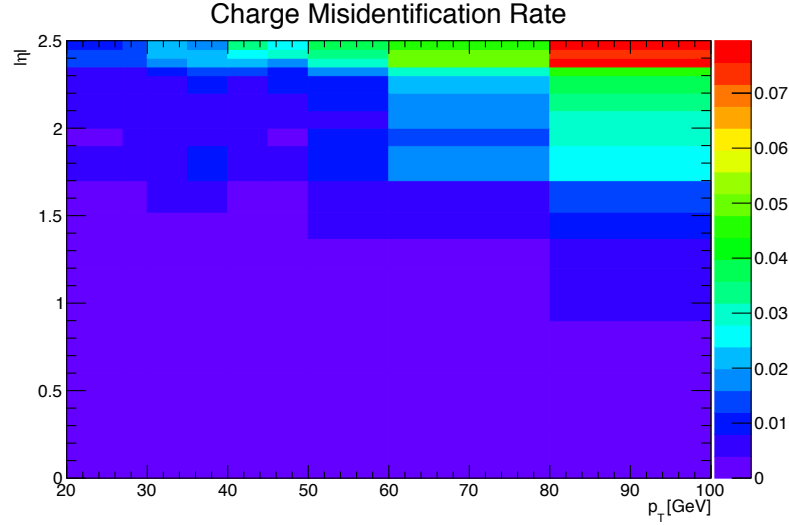


Figure 5.11: Charge misidentification rates for electrons as a function of $|\eta|$ and p_T . Rates are calculated from $Z \rightarrow e^+e^-$ MC after applying scale factors to approximate the charge mis-ID rates in data.

the material effects leading to charge flip; as a result, scale factors are applied to the MC in order for it to better reflect the real performance. These scale factors are obtained from the ratio of charge mis-ID rates in data and uncorrected MC in [40] following the method outlined in [74]. Once the scale factors are applied, the charge misidentification rate ε can be extracted by comparing the electron's reconstructed charge with the charge of its truth particle:

$$\varepsilon(\eta, p_T) = \frac{N_{\text{wrong charge}}}{N_{\text{prompt electrons}}} \quad (5.1)$$

The charge mis-ID rate is calculated in bins of electron $|\eta|$ and p_T and varies from below 0.1% in the

central region of the detector up to 8% in the forward regions for high p_T (above 90 GeV) electrons.

A two-dimensional plot of ε can be found in Figure 5.11.

Given the charge flip rate $\varepsilon(\eta, p_T)$, the rate at which an electron has its charge correctly reconstructed is $(1 - \varepsilon)$. Thus there are three possible combinations of charge identification, assuming a two-electron event:

- 1304 1. Both electrons are reconstructed correctly: $(1 - \varepsilon)^2$
- 1305 2. Both electrons are mis-reconstructed: ε^2
- 1306 3. Only one electron is mis-reconstructed: $2\varepsilon(1 - \varepsilon)$

1307 In order to estimate the size of the background from charge misidentification, opposite-sign events
 1308 are selected using the default event selection for a given signal or control region with the same-sign
 1309 requirement inverted. These events are then weighted by the probability for one of the electrons to
 1310 be reconstructed with the wrong charge:

$$\omega = \frac{\varepsilon_1(1 - \varepsilon_2) + \varepsilon_2(1 - \varepsilon_1)}{(1 - \varepsilon_1)(1 - \varepsilon_2) + \varepsilon_1\varepsilon_2} \quad (5.2)$$

1311 where the subscripts 1 and 2 refer to the leading and subleading electrons, respectively, and ε_i is a
 1312 function of the η and p_T of the i^{th} electron. In the case of an event with only one electron and one
 1313 muon, Equation 5.2 simplifies:

$$\omega = \frac{\varepsilon}{1 - \varepsilon} \quad (5.3)$$

1314 This method assumes that there is little contamination from fake electrons in the opposite-sign
 1315 sample, and this has been verified with MC simulation.

1316 Additionally, charge-flipped electrons tend to be reconstructed with lower energy when compared
 1317 to electrons with the correct charge. This is due to energy loss from the material interactions that
 1318 can cause the charge to be misidentified. A correction factor is calculated from MC simulations,
 1319 comparing the p_T of the truth electron to its reconstructed counterpart:

$$\alpha = \frac{\left(\frac{p_T^{\text{reco}}}{p_T^{\text{truth}}} - 1\right)_{\text{correct charge}}}{\left(\frac{p_T^{\text{reco}}}{p_T^{\text{truth}}} - 1\right)_{\text{wrong charge}}} \quad (5.4)$$

1320 The correction is then applied to the p_T of the charge-flipped electron via

$$p_T = p_T^0 / (1 + \alpha) + dE \quad (5.5)$$

1321 where p_T^0 is the uncorrected p_T of the electron and dE is a gaussian smearing factor centered at
 1322 zero with a width related to the energy resolution. Since which electron is misreconstructed is never
 1323 determined in this method, in the case of a two-electron event, the energy correction is applied
 1324 randomly to one of the two electrons based on the probabilities for them to be charge-flipped. This
 1325 also determines the overall sign of the event; the charge of the electron that does not receive the
 1326 correction is taken to be the charge for both.

1327 Systematic uncertainties on the charge mis-ID rates are calculated by generating two additional
 1328 sets of rates with the uncertainties on the scale factors varied up and down. The size of the esti-
 1329 mated charge flip background without the energy correction applied is also taken as a systematic
 1330 uncertainty. These systematic uncertainties are estimated to be approximately $\pm 15\%$.

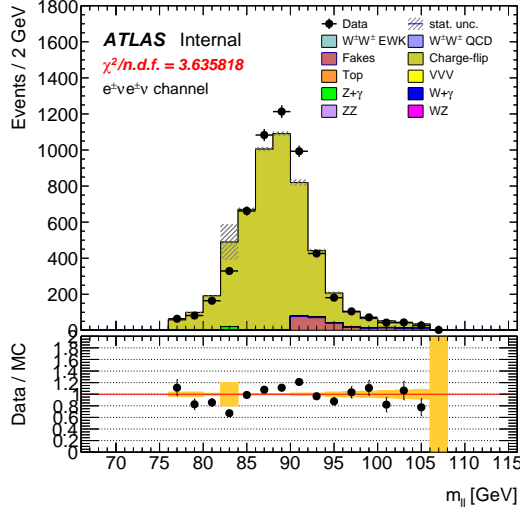


Figure 5.12: Dilepton invariant mass distribution m_{ll} for the ee channel in the same-sign inclusive VR.

1331 5.3.3.1 Validation of the charge misidentification estimate

1332 The performance of the charge misidentification estimation is tested in the same-sign inclusive
 1333 validation region (VR), defined in Table 5.12. For ee events, the mass of the dilepton pair is required
 1334 to lie within 15 GeV of the Z boson mass to increase the purity of the charge flip background.
 1335 $t\bar{t}$ production, which can contribute to both the charge mis-ID and fake lepton backgrounds, is
 1336 suppressed by the b -jet veto. The di-electron invariant mass is shown in Figure 5.12, and distributions
 1337 of the leading and subleading electron p_T in the ee -channel are shown in Figure 5.13 with the Z
 1338 mass cut inverted. Agreement between data and prediction is seen within the total statistical and
 1339 systematic uncertainties in the VR.

Same-sign inclusive VR
Exactly 2 same-sign signal leptons
$p_T > 27$ GeV for both leptons
$m_{ll} > 20$ GeV
$ m_{ee} - m_Z > 15$ GeV ($e^\pm e^\pm$ -channel only)
$N_{b\text{-jet}} = 0$

Table 5.12: Selection criteria for the same-sign inclusive validation region.

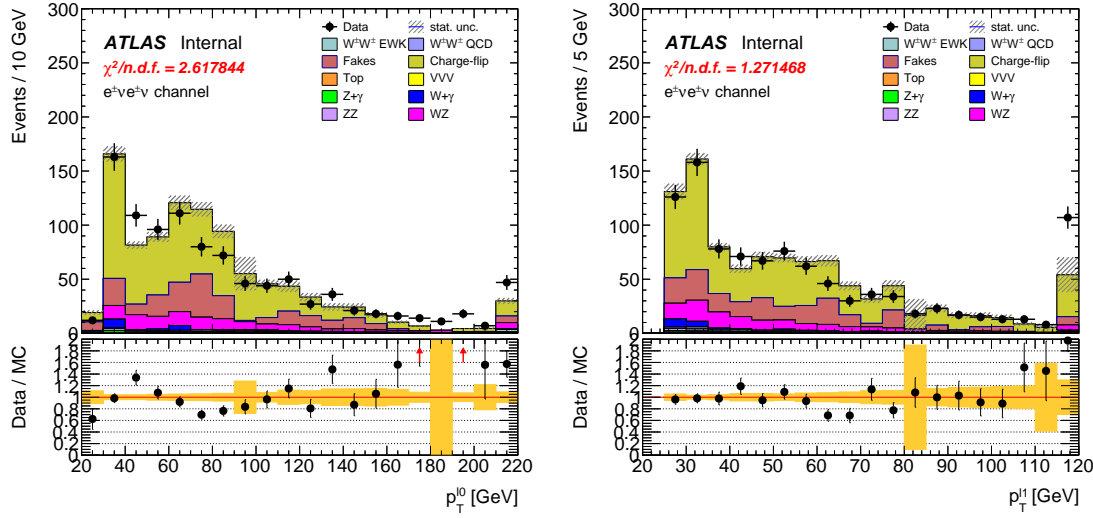


Figure 5.13: p_T distributions for the leading (left) and subleading (right) electron for the ee channel in the same-sign inclusive VR. In these plots, the cut requiring m_{ee} to fall within the Z mass window has been inverted in order to test the modelling away from the Z peak.

1340 5.3.4 Estimation of non-prompt backgrounds with the fake factor method

1341 Events with one prompt lepton produced in association with hadronic jets can pass the event selection
 1342 if a jet is misidentified as a charged lepton or if a non-prompt lepton from the decay of a heavy
 1343 flavor particle (such as b - and c -hadrons) passes the signal lepton criteria. These misidentified jets
 1344 and non-prompt leptons are collectively referred to as *fake leptons*, or simply *fakes*. The rate at
 1345 which a fake lepton is misidentified is generally not modelled well enough by the MC to accurately
 1346 estimate their contributions directly from simulation. Therefore, a data-driven technique called the
 1347 *fake factor* is used to estimate the size and shape of background processes from fake leptons. In this
 1348 analysis, a new modification to the fake factor is used involving the particle isolation variables; the
 1349 method is outlined in the context of the *default* fake factor in Section 5.3.4.1, and the modified fake
 1350 factor is outlined in Section 5.3.4.2.

1351 5.3.4.1 Overview of the default fake factor method

1352 The goal of the fake factor method is to measure the fake rate from real collision events in a region
 1353 enriched in fake leptons and use it to estimate the size of the fake lepton background in a chosen
 1354 signal or control region. This is done by creating two samples using different lepton definitions:

- 1355 1. The *nominal* sample is made up of leptons passing the signal selection.

1356 2. The *loose* sample is made up of leptons that fail the signal selection while still passing a
 1357 loosened set of criteria. This sample is enriched in fake leptons and is orthogonal to the set of
 1358 signal leptons.

1359 Using the sets of nominal and loose leptons, a fake factor f can be calculated in a region enriched
 1360 in processes that are prone to producing fake leptons:

$$f = \frac{N_{\text{nominal}}}{N_{\text{loose}}} \quad (5.6)$$

1361 Since the fake rate is not expected to be constant over the entire phase space, the fake factor can
 1362 be divided into bins:

$$f(b) = \frac{N_{\text{nominal}}(b)}{N_{\text{loose}}(b)} \quad (5.7)$$

1363 where b represents the bin number. In this analysis, the fake factor is binned in lepton p_T .

1364 In order to estimate the fake background contribution in a given signal or control region, the
 1365 fake factor is applied to a second control region with a selection identical to the region of interest
 1366 with one of the leptons required to satisfy the loose criteria. The region for which the background
 1367 is estimated contains two nominal leptons and is referred to as *nominal+nominal* (NN), and the
 1368 associated control region where the fake factor is applied contains one nominal and one loose lepton
 1369 and is referred to as *nominal+loose* (NL). The fake background in a NN region can then be
 1370 calculated as:

$$N_{NN}^{\text{fake bkg.}} = \sum_b f(b) N_{NL}(b) \quad (5.8)$$

1371 Backgrounds containing two prompt leptons can also enter the NL region if one of the leptons
 1372 passes the nominal selection and the other passes the loose selection. Since the fake factor method
 1373 estimates the fake background by scaling the amount of non-prompt events in the NL region, if these
 1374 prompt contributions are not removed, they will be included in the scaling and the background
 1375 will be overpredicted. The final estimate of the fake background becomes:

$$N_{NN}^{\text{fake bkg.}} = \sum_b f(b) (N_{NL}(b) - N_{NL}^{\text{prompt}}(b)) \quad (5.9)$$

1376 **5.3.4.2 The fake factor with p_T^{cone}**

1377 When a jet produces a non-prompt lepton, that lepton only carries a fraction of the underlying jet's
 1378 total momentum. Due to the isolation cut applied to the nominal leptons, they typically carry a

1379 much larger percentage of the underlying jet momentum¹² than the loose leptons (which are allowed
 1380 to fail this criteria).

1381 This discrepancy in the underlying jet momentum fraction can cause problems in the calculation
 1382 of the fake factor f . Consider the case where two separate events have jets of identical momentum,
 1383 but one produces a non-prompt lepton that passes the nominal selection, and the other produces a
 1384 non-prompt lepton that passes the loose selection. The loose lepton on average will have lower p_T
 1385 than the nominal lepton despite both originating from jets with the same momentum. This can be
 1386 seen explicitly when comparing the p_T of a muon to its associated truth jet:

$$\Delta p_T(\mu, j) = \frac{p_T(j) - p_T(\mu)}{p_T(j) + p_T(\mu)} \quad (5.10)$$

1387 Since muons are not included in the jet reconstruction algorithm, Δp_T approximates the momentum
 1388 of the muon compared to the rest of the jet. For muons that carry more than 50% of the jet's
 1389 momentum, Δp_T will be negative and vice-versa. The Δp_T distributions for nominal and loose
 1390 muons in $t\bar{t}$ MC events is shown Figure 5.14, where a 50 GeV jet on average corresponds to a
 1391 35 GeV nominal muon and a 20 GeV loose muon¹³.

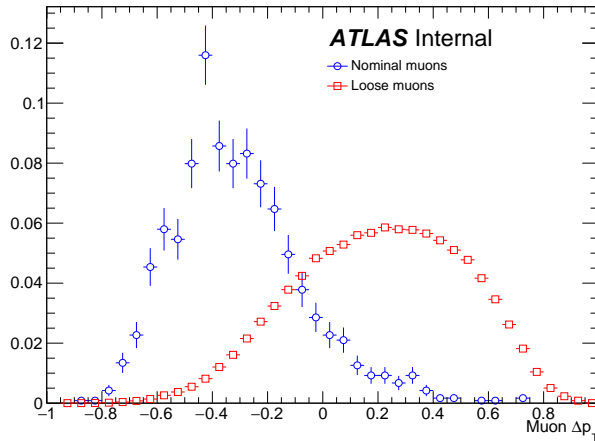


Figure 5.14: Δp_T distributions for nominal (blue) and loose (red) muons in simulated $t\bar{t}$ events. Each muon has been matched to a truth-level jet. Both distributions are normalized to unit area.

1392 Since the default fake factor defined in Equation 5.7 is binned in lepton p_T , within a given bin,

¹²Since the isolation variables are a measure of detector activity around the lepton, if other nearby particles carried a significant portion of the jet's momentum, the lepton would likely fail this cut.

¹³To better illustrate the point, here the muon is added back into the jet p_T , and the corresponding muon p_T is obtained via $\Delta p_T(\mu, j) = \frac{(p_T(j) - p_T(\mu)) - p_T(\mu)}{(p_T(j) - p_T(\mu)) + p_T(\mu)} = \frac{p_T(j) - 2p_T(\mu)}{p_T(j)}$.

1393 the underlying jet p_T spectrum can differ substantially between the numerator and the denominator.
 1394 Additionally, these differences can vary depending on the process producing the non-prompt leptons
 1395 or on the specific kinematic selections of the signal or control regions where the fake factor is applied.

1396 Fortunately, the majority of the jet momentum not carried by the non-prompt lepton (excluding
 1397 neutrinos) can be recovered using isolation variables. A track-based isolation is chosen, referred to
 1398 as p_T^{cone} , and it contains the sum of the p_T of all particle tracks originating from the primary vertex
 1399 within a cone of $\Delta R < 0.3$ around the lepton. Thus, the sample of loose leptons in the denominator
 1400 of the fake factor calculation is binned in $p_T + p_T^{\text{cone}}$ rather than simply lepton p_T . Adding the
 1401 isolation cone greatly reduces the difference in the fraction of the underlying jet momentum carried
 1402 by the nominal and loose leptons. To check this, a new Δp_T is calculated between a lepton and its
 1403 matched truth jet, where the truth jet p_T has been corrected to include all muons within a cone of
 1404 $\Delta R < 0.4$:

$$p_T(j) = p_T(j_{\text{truth}}) + \sum_{\Delta R < 0.4} p_T(\mu_{\text{truth}}) \quad (5.11)$$

1405 The Δp_T distributions comparing p_T and $p_T + p_T^{\text{cone}}$ for nominal and loose leptons using the corrected
 1406 jet p_T are found in Figure 5.15, and better agreement is seen between the numerator (nominal) and
 1407 denominator (loose with $p_T + p_T^{\text{cone}}$) distributions.

1408 The numerator remains binned in lepton p_T , due to the fact that it is meant to mirror the signal
 1409 region as closely as possible, and the signal lepton selection does not use $p_T + p_T^{\text{cone}}$. The impact of
 1410 this is expected to be negligible due to the p_T^{cone} isolation being small for signal leptons, as shown
 1411 for muons in Figure 5.16. Finally, the fake factor f becomes:

$$f(b) = \frac{N_{\text{nominal}}(b(p_T))}{N_{\text{loose}}(b(p_T + p_T^{\text{cone}}))} \quad (5.12)$$

1412 5.3.4.3 Application of the fake factor

1413 The fake factor itself is measured from a sample data events passing a dijet selection requiring
 1414 exactly one lepton (either passing the nominal or loose selections) and at least one jet. The leading
 1415 jet must also be b -tagged and approximately back-to-back with the lepton in order to enhance non-
 1416 prompt lepton contributions while reducing contributions from processes involving W and Z bosons.
 1417 W boson events are further suppressed by requiring the sum of the E_T^{miss} and the transverse mass
 1418 of the lepton and E_T^{miss} to be less than 50 GeV. The full event selection for the dijet region is
 1419 summarized in Table 5.13.

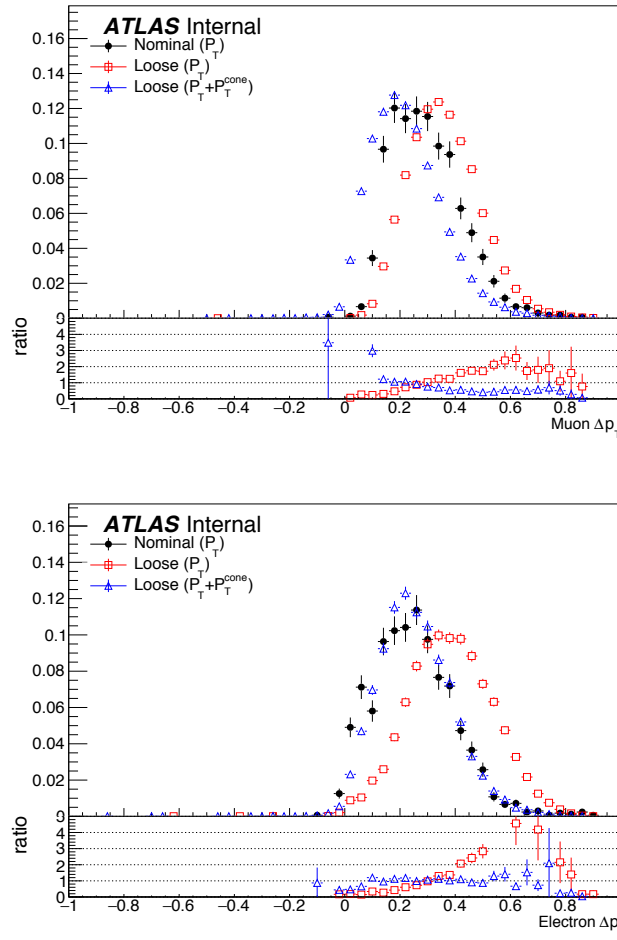


Figure 5.15: Δp_T distributions for muons (top) and electrons (bottom) in simulated $t\bar{t}$ events. Each lepton has been matched to a truth-level jet, and that truth jet has had its p_T corrected to include all truth muons within a cone of $\Delta R < 0.4$. The nominal leptons are in black. Δp_T is calculated for the loose leptons using p_T (red) and $p_T + p_T^{\text{cone}}$ (blue).

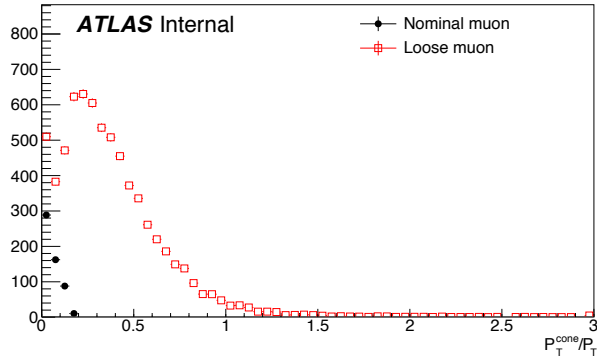


Figure 5.16: Distributions of p_T^{cone}/p_T for nominal (black) and loose (red) muons in simulated $t\bar{t}$ events.

Dijet event selection	
Event preselection	
Exactly one lepton with $p_T > 15$ GeV	
$N_{\text{jet}} > 0$	
Leading jet is b -tagged	
$p_T^{\text{lead. jet}} > 25$ GeV	
$p_T^{\text{lead. jet}} > 30$ GeV if $ \eta_j > 2.5$	
$ \Delta\phi(l, \text{lead. jet}) > 2.8$	
$m_T(l, E_T^{\text{miss}}) + E_T^{\text{miss}} < 50$ GeV	

Table 5.13: Event selection for the dijet region used for calculating the fake factor. The selected lepton can pass either the nominal (signal) or loose selections. In the case of the nominal leptons, the $p_T > 27$ GeV requirement is replaced with $p_T > 15$ GeV.

1420 The numerator sample is constructed from dijet events in which the lepton passes the nominal
 1421 (signal) selection and is binned in the lepton p_T . Similarly, the denominator sample is made up of
 1422 the remaining dijet events where the lepton passes the loose selection and is binned in the lepton
 1423 $p_T + p_T^{\text{cone}}$. The nominal and loose leptons pass the signal selection¹⁴ and loose selection, respectively,
 1424 defined earlier in Table 5.3 for muons and Table 5.4 for electrons. Backgrounds from $W + \text{jets}$, $Z + \text{jets}$,
 1425 $t\bar{t}$, and single top processes are estimated from MC simulations requiring one lepton to be prompt
 1426 using the truth information; these contributions are subtracted from the dijet data. The fake factor
 1427 is then calculated using Equation 5.12 for muons and for central and forward electrons separately.
 1428 The muon fake factor is shown in Figure 5.17, and the two electron fake factors are shown in
 1429 Figure 5.18. The numerical values of the fake factors, including their systematic uncertainties which

¹⁴The $p_T > 27$ GeV cut in the signal lepton selection is dropped in favor of the $p_T > 15$ GeV requirement in the dijet selection.

¹⁴³⁰ will be discussed in Section 5.3.4.4, are listed in Table 5.14.

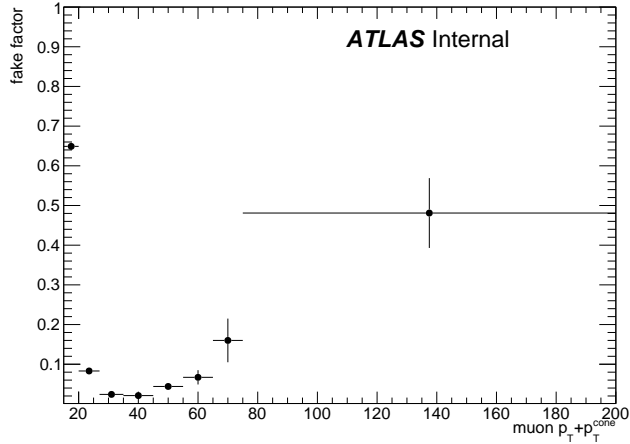


Figure 5.17: The measured fake factor as a function of muon $p_T + p_T^{\text{cone}}$. The error bars represent the statistical uncertainty only.

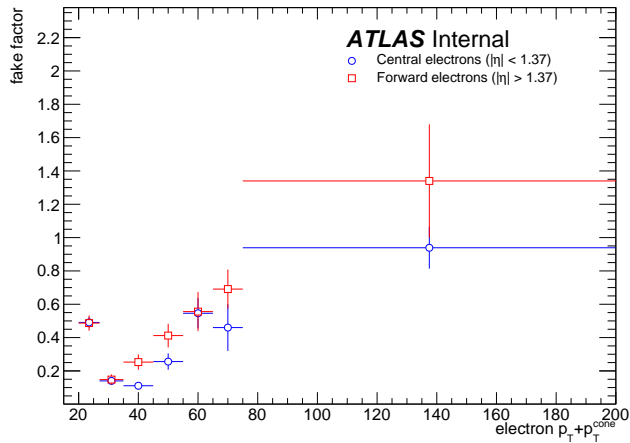


Figure 5.18: The measured fake factor as a function of electron $p_T + p_T^{\text{cone}}$ in the central ($|\eta| < 1.37$, blue) and forward ($|\eta| > 1.37$, red) regions of the detector. The error bars represent the statistical uncertainty only.

¹⁴³¹ In order to properly account for the denominator being binned in $p_T + p_T^{\text{cone}}$, special care needs
¹⁴³² to be taken when estimating the fake background from the NL regions. For the purposes of the
¹⁴³³ fake factor calculation, it is perhaps more intuitive to consider a loose *object* with $p_T = p_T + p_T^{\text{cone}}$
¹⁴³⁴ instead of simply a loose *lepton*, as the lepton and the underlying jet are treated as a whole with this

method. When the lepton p_T cuts required by a particular signal or control region are applied to nominal and loose leptons, the cut is applied to the p_T of the nominal lepton and to the $p_T + p_T^{\text{cone}}$ of the loose object. Similarly, when looking up the fake factor weight for a given NL event, the value taken from the bin corresponding to the $p_T + p_T^{\text{cone}}$ of the loose object. Finally, when applying the weight to the event, $p_T + p_T^{\text{cone}}$ is assigned as the p_T of the loose object. Figure 5.19 contains a graphical representation of this procedure.

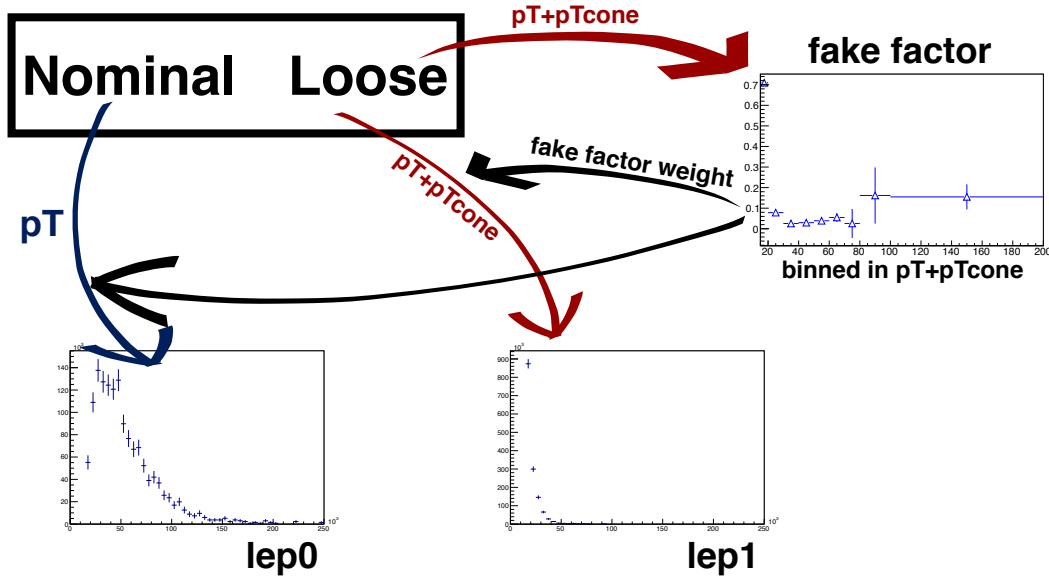


Figure 5.19: Graphical representation of the fake factor application using $p_T + p_T^{\text{cone}}$. The value of $p_T + p_T^{\text{cone}}$ for the loose lepton is used to “look up” the fake factor weight which is then applied to the event. The loose lepton’s p_T becomes $p_T + p_T^{\text{cone}}$ for the purpose of the fake background estimation.

Finally, it should be noted that the addition of p_T^{cone} to the loose object may cause the loose leptons in the denominator sample to migrate into higher bins. This results in an overall decrease in the number of loose objects in the lower $p_T + p_T^{\text{cone}}$ bins due to there not being additional leptons at lower p_T to replace them. Since the fake factor is a ratio of the number of events in a bin, this effect causes the first few bins of the fake factor to increase, as can be seen clearly in Figure 5.17. However, the signal and control regions (and their corresponding NL regions) contain a $p_T > 27$ GeV cut that prevents these migrations from negatively impacting the fake estimation.

1448 **5.3.4.4 Systematic uncertainties**

1449 Four sources of systematic uncertainty are considered: the dijet event selection, the prompt back-
 1450 ground subtraction, the jet flavor composition, and residual dependence on the underlying jet p_T
 1451 spectrum. In order to measure the impact of these systematics, new fake factors are computed
 1452 with each of the systematic variations and the differences from the nominal values are taken as the
 1453 uncertainty.

- 1454 1. In order to estimate uncertainties due to the dijet selection, the cut on $M_T + MET$ is varied
 1455 by ± 5 GeV, $\Delta\phi(l, j)$ by ± 0.1 , and the jet p_T cut by $+5$ GeV.
- 1456 2. To estimate the systematic uncertainty on the prompt background subtraction, the MC pre-
 1457 diction in a $W+jets$ control region is compared to data. The discrepancy between data and
 1458 MC is found to be approximately 10% [40]. Therefore, the prompt background used for the
 1459 subtraction is scaled up and down by $\pm 10\%$.
- 1460 3. The difference in the jet flavor composition between the dijet events and the events in the
 1461 NL regions can affect the accuracy of the fake background estimation. The dijet sample is
 1462 dominated by light jets, while the NL regions tend to be dominated by heavy flavor from $t\bar{t}$.
 1463 To account for this, the fake factor is computed with a b -jet veto.
- 1464 4. To measure any residual dependence on the underlying jet p_T spectrum, the leading jet p_T
 1465 distribution is reweighted to match the p_T spectrum of truth jets that produce fake leptons
 1466 in MC simulations. This results in an increase in the number of nominal and loose leptons at
 1467 high momentum [40].

1468 **5.3.4.5 Results of the fake factor**

1469 The fake background contribution in the signal region is estimated by applying the fake factors
 1470 to the equivalent NL region using Equation 5.9, where the fake factor used corresponds to the
 1471 flavor of the loose lepton in the event. As usual, the prompt background is subtracted from the
 1472 NL events using MC simulation. Charge misidentification is handled using the same method as
 1473 in Section 5.3.3, with an additional set of charge flip rates calculated for loose leptons. The fake
 1474 background yields in the signal region are listed in Table 5.15. An overall uncertainty of 50% is
 1475 assigned to the fake background estimation in $\mu^\pm\mu^\pm$ events, and between 40% to 90% for $e^\pm e^\pm$ and
 1476 $\mu^\pm e^\pm$ events, including both statistical and systematic effects.

fake factor	$p_T[15, 20]$	$p_T[20, 27]$	$p_T[27, 35]$	$p_T[35, 45]$	$p_T[45, 55]$	$p_T[55, 65]$	$p_T[65, 75]$	$p_T[75, 200]$
nominal	0.649 ± 0.007	0.083 ± 0.002	0.024 ± 0.002	0.021 ± 0.003	0.044 ± 0.007	0.067 ± 0.018	0.160 ± 0.055	0.481 ± 0.088
MT+MET	0.649 ± 0.007	0.082 ± 0.002	0.082 ± 0.002	0.020 ± 0.003	0.045 ± 0.007	0.068 ± 0.018	0.207 ± 0.062	0.523 ± 0.086
$\Delta\phi(\ell, j)$	0.645 ± 0.008	0.083 ± 0.003	0.024 ± 0.002	0.021 ± 0.004	0.045 ± 0.008	0.064 ± 0.021	0.064 ± 0.058	0.438 ± 0.092
Jet p_T	0.650 ± 0.007	0.083 ± 0.002	0.024 ± 0.002	0.021 ± 0.003	0.045 ± 0.007	0.069 ± 0.018	0.159 ± 0.018	0.481 ± 0.088
$N_{b\text{-jet}} = 0$	0.724 ± 0.003	0.094 ± 0.001	0.035 ± 0.001	0.025 ± 0.002	0.022 ± 0.004	0.060 ± 0.015	0.026 ± 0.053	0.044 ± 0.134
Bkg. subtraction	0.648 ± 0.007	0.083 ± 0.002	0.024 ± 0.002	0.019 ± 0.003	0.037 ± 0.007	0.044 ± 0.019	0.096 ± 0.062	0.370 ± 0.082
Jet p_T Reweighting	0.539 ± 0.077	0.093 ± 0.007	0.025 ± 0.004	0.043 ± 0.019	0.063 ± 0.014	0.085 ± 0.025	0.141 ± 0.110	1.962 ± 0.492

(a) Fake factor for muons.

fake factor	$p_T[20, 27]$	$p_T[27, 35]$	$p_T[35, 45]$	$p_T[45, 55]$	$p_T[55, 65]$	$p_T[65, 75]$	$p_T[75, 200]$
nominal	0.491 ± 0.031	0.140 ± 0.020	0.111 ± 0.023	0.256 ± 0.049	0.546 ± 0.091	0.460 ± 0.140	0.939 ± 0.125
MT+MET	0.493 ± 0.030	0.138 ± 0.019	0.115 ± 0.022	0.261 ± 0.045	0.559 ± 0.084	0.656 ± 0.091	0.802 ± 0.016
$\Delta\phi(\ell, j)$	0.488 ± 0.032	0.137 ± 0.020	0.110 ± 0.025	0.283 ± 0.053	0.503 ± 0.097	0.351 ± 0.149	1.117 ± 0.255
Jet p_T	0.489 ± 0.035	0.134 ± 0.021	0.105 ± 0.025	0.224 ± 0.048	0.593 ± 0.093	0.356 ± 0.144	0.928 ± 0.177
$N_{b\text{-jet}} = 0$	0.506 ± 0.029	0.140 ± 0.018	0.111 ± 0.022	0.260 ± 0.046	0.545 ± 0.084	0.546 ± 0.120	0.882 ± 0.103
Bkg. subtraction	0.493 ± 0.032	0.146 ± 0.021	0.115 ± 0.024	0.259 ± 0.049	0.550 ± 0.091	0.460 ± 0.140	0.939 ± 0.125
Jet p_T Reweighting	0.387 ± 0.009	0.130 ± 0.008	0.321 ± 0.012	0.473 ± 0.015	0.716 ± 0.180	0.716 ± 0.180	0.716 ± 0.180

(b) Fake factor for central electrons ($|\eta| < 1.37$).

fake factor	$p_T[20, 27]$	$p_T[27, 35]$	$p_T[35, 45]$	$p_T[45, 55]$	$p_T[55, 65]$	$p_T[65, 75]$	$p_T[75, 200]$
nominal	0.487 ± 0.046	0.148 ± 0.031	0.253 ± 0.046	0.412 ± 0.071	0.556 ± 0.117	0.691 ± 0.117	1.340 ± 0.340
MT+MET	0.483 ± 0.045	0.152 ± 0.031	0.241 ± 0.043	0.443 ± 0.070	0.565 ± 0.106	0.668 ± 0.117	1.075 ± 0.189
$\Delta\phi(\ell, j)$	0.495 ± 0.047	0.156 ± 0.033	0.271 ± 0.052	0.364 ± 0.074	0.664 ± 0.107	0.749 ± 0.056	0.885 ± 0.084
Jet p_T	0.471 ± 0.051	0.158 ± 0.035	0.247 ± 0.051	0.474 ± 0.085	0.283 ± 0.107	0.546 ± 0.149	1.189 ± 0.266
$N_{b\text{-jet}} = 0$	0.478 ± 0.042	0.170 ± 0.031	0.274 ± 0.046	0.389 ± 0.066	0.645 ± 0.104	0.757 ± 0.102	1.319 ± 0.326
Bkg. subtraction	0.523 ± 0.048	0.149 ± 0.033	0.235 ± 0.045	0.429 ± 0.073	0.555 ± 0.117	0.691 ± 0.117	1.340 ± 0.340
Jet p_T Reweighting	0.525 ± 0.011	0.234 ± 0.013	0.644 ± 0.016	0.710 ± 0.014	0.274 ± 0.316	0.274 ± 0.316	0.274 ± 0.316

(c) Fake factor for forward electrons ($1.37 < |\eta|$).Table 5.14: Values of the fake factor in each p_T bin and for each individual systematic source.

	estimated yield	f_e stat. up	f_e stat. dn	f_e syst. up	f_e syst. dn	f_μ stat. up	f_μ stat. dn	f_μ syst. up	f_μ syst. dn
$e^\pm e^\pm$	11.42 ± 3.13	—	—	—	—	—	—	—	—
$\mu^\pm \mu^\pm$	4.82 ± 0.77	—	—	—	—	0.65	-0.65	3.64	-0.61
$\mu^\pm e^\pm$	37.08 ± 5.16	4.90	-4.90	5.59	-14.34	1.39	-1.39	16.10	-1.98

Table 5.15: Estimated yields for the fake lepton background. The estimated yield is shown in the first column together with the statistical uncertainty followed by the systematic uncertainties from variations of the the fake factors within their statistical (stat.) and systematic (syst.) uncertainties. The labels f_e and f_μ indicate the fake factors for electrons and muons, respectively.

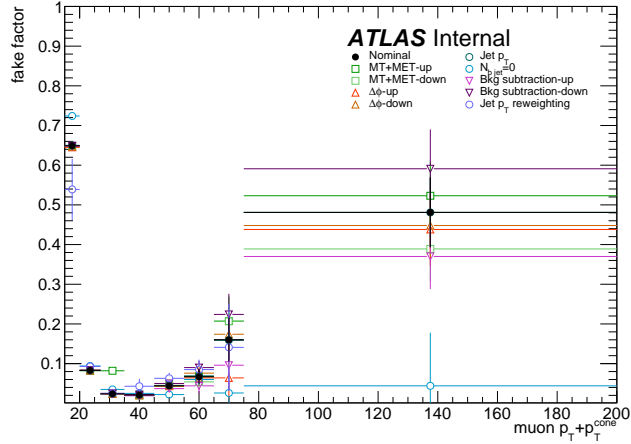


Figure 5.20: Systematic variations in the fake factor as a function of muon $p_T + p_T^{\text{cone}}$. The individual fake factors obtained for each systematic variation are displayed with their statistical uncertainties.

1477 5.3.4.6 Validation of the fake factor

1478 The accuracy of the fake factor method is tested in several validation regions, the most sensitive
 1479 of which is the same-sign top fakes VR (SS top VR), defined in Table 5.16. This region inverts
 1480 the signal region's b -jet veto to accept events with exactly one b -jet. Due to this requirement, the
 1481 dominant source of events comes from the $t\bar{t}$ process where a b -jet fakes an isolated lepton. The
 1482 distribution of the subleading lepton p_T in this VR is shown in Figure 5.22 for all lepton flavor
 1483 combinations. There is good agreement between the data and the prediction, even when only taking
 1484 into account the statistical uncertainty and not the large systematic uncertainties assigned to the
 1485 fake estimation.

Same-sign inclusive VR
Exactly 2 same-sign signal leptons
$p_T > 27$ GeV for both leptons
$m_{ll} > 20$ GeV
$ m_{ee} - m_Z > 15$ GeV ($e^\pm e^\pm$ -channel only)
$N_{b\text{-jet}} = 1$
$N_{\text{jet}} \geq 2$
Leading jet $p_T > 65$ GeV
Subleading jet $p_T > 35$ GeV

Table 5.16: Selection criteria for the same-sign top fakes validation region.

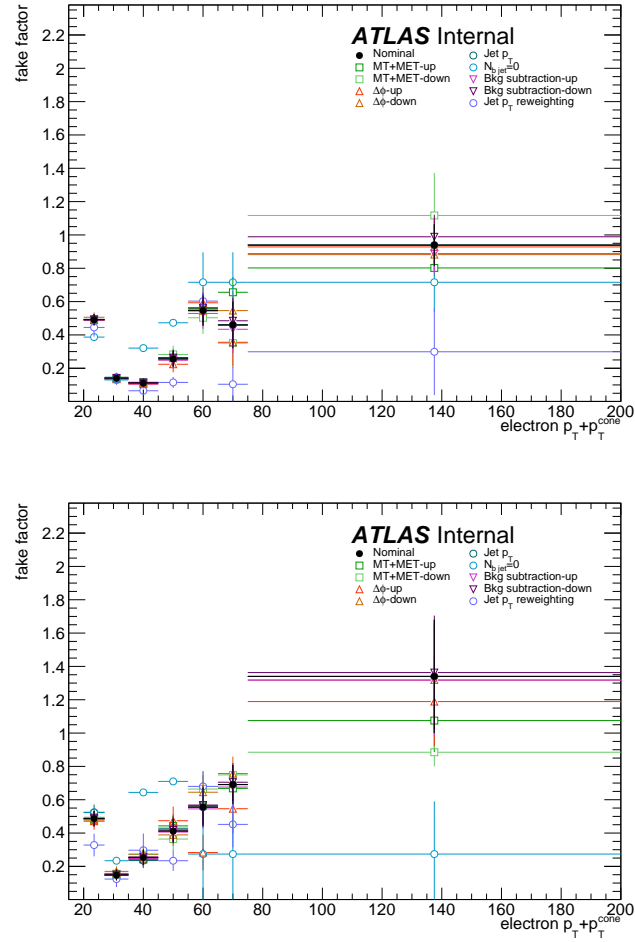


Figure 5.21: Systematic variations in the fake factor as a function of electron $p_T + p_T^{\text{cone}}$ in the central ($|\eta| < 1.37$, top) and forward ($|\eta| > 1.37$, bottom) regions of the detector. The individual fake factors obtained for each systematic variation are displayed with their statistical uncertainties.

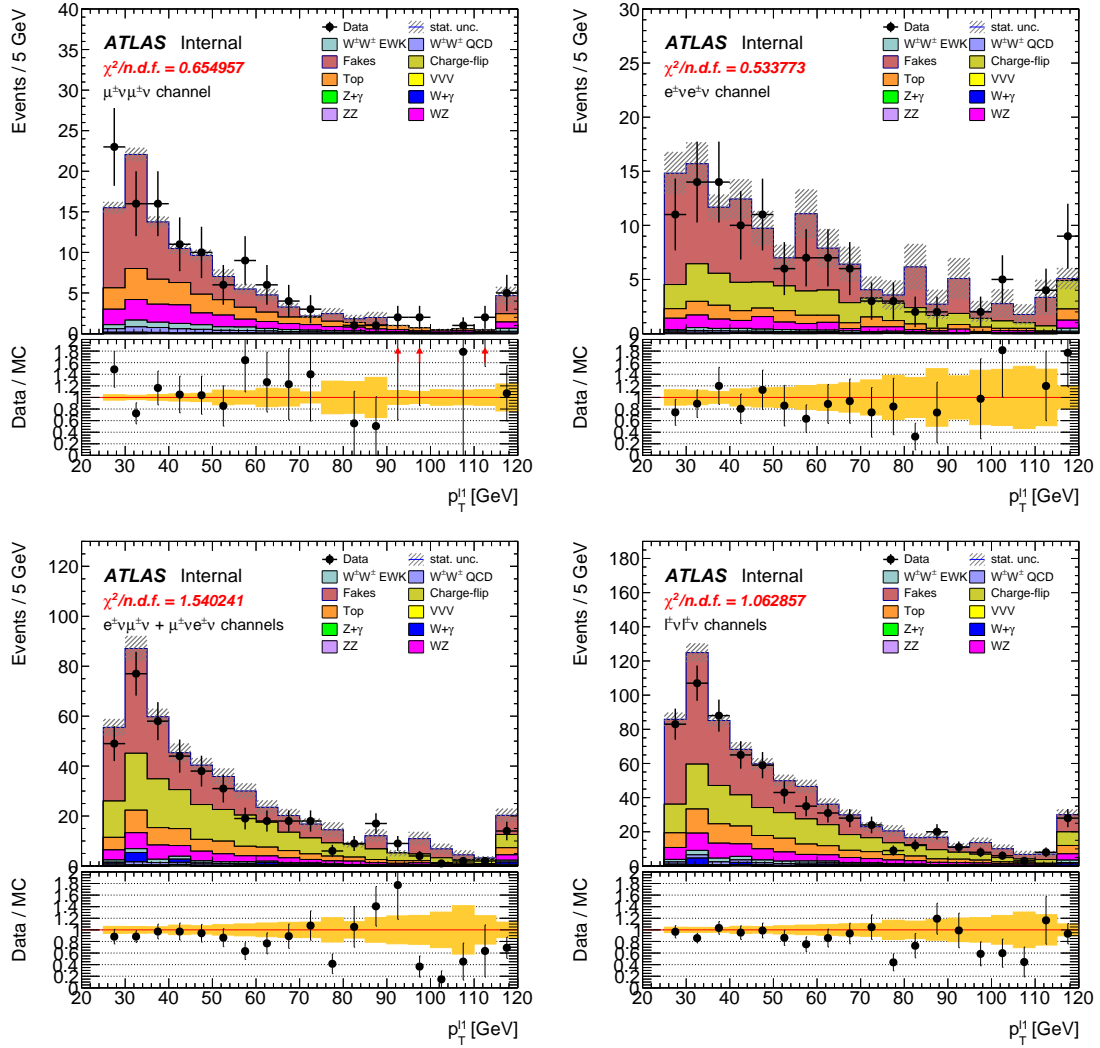


Figure 5.22: Distributions of the subleading lepton p_T in the same-sign top fakes VR for $\mu^\pm\mu^\pm$ events (top right), $e^\pm e^\pm$ events (top left), $\mu^\pm e^\pm$ events (bottom left), and all events combined (bottom right). All errors are statistical only.

1486 **5.3.5 Reduction of WZ background using custom overlap removal**

1487 The dominant source of prompt background in this analysis comes from WZ events where both
 1488 bosons decay leptonically. Traditionally, the background is dealt with by imposing a veto on any
 1489 event with a third lepton passing some loose identification criteria (the so-called *trilepton veto*). In
 1490 the case of this analysis, if one or more leptons (in addition to the two signal leptons) passed the
 1491 preselection criteria, the event would be rejected. However, WZ events can still enter the signal
 1492 region if one of the leptons fails the veto selection or falls outside of the detector’s acceptance.

1493 In order to understand the sources of WZ events that are not removed by the trilepton veto,
 1494 a study was performed on truth-level leptons¹⁵ on $W^\pm W^\pm jj$ and WZ MC samples. Events with
 1495 three truth leptons were selected, and each was matched to its reconstruction-level partner by finding
 1496 the closest $\Delta R(\text{truth}, \text{reco})$ and $\Delta p_{\text{T},\text{truth},\text{reco}}$ match. For events surviving the trilepton veto, the
 1497 two signal leptons were removed, and the remaining leptons represent real leptons that failed to
 1498 be selected for the veto. Between 40-50% of these leptons fell outside of the eta acceptance of the
 1499 analysis (see Figure 5.23) and were unrecoverable. The second largest source of leptons failing the
 1500 preselection was the OR, defined in Section 5.2.1.4. The standard OR procedure appeared to be
 1501 too aggressive in removing leptons in favor of jets, causing many three lepton events to “lose” their
 1502 third lepton and pass the trilepton veto. Therefore a *Custom OR* was investigated which would
 1503 replace the standard OR in the preselection and allow for better WZ rejection by removing fewer
 1504 third leptons.

1505 **TODO:** Mention how the extra leptons in the $W^\pm W^\pm jj$ are background leptons since there are
 1506 only 2 from the main decay

1507 In order to construct a “custom” OR, a new quantity is defined between a lepton (l) and a nearby
 1508 jet (j)

$$p_{\text{T},\text{ratio}}(l, j) = \frac{p_{\text{T}l}}{p_{\text{T}j}} \quad (5.13)$$

1509 which, along with $\Delta R(l, j)$, will allow for more third leptons to pass the preselection. The idea
 1510 behind including $p_{\text{T},\text{ratio}}$ is to be able to preferentially remove background leptons originating from
 1511 jets (i.e. those that carry a low percentage of the total jet momentum) instead of removing *any*
 1512 lepton near to jet. The distributions of $p_{\text{T},\text{ratio}}$ and the associated efficiency curves for muons and
 1513 electrons can be found in Figures 5.24 and 5.26, respectively, and the distributions for $\Delta R(\mu, j)$ for

¹⁵Truth particles are the particles produced directly by the MC generator before being passed through the full detector simulation, at which point they are considered *reconstruction-level* (or *reco-level*) particles.

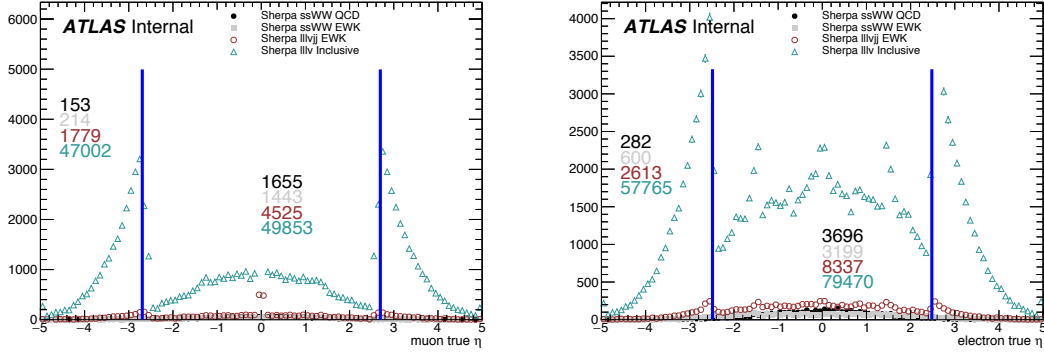


Figure 5.23: Pseudorapidity (η) distributions of truth muons (top) and electrons (bottom) for Sherpa $W^\pm W^\pm jj$ and WZ MC samples. The blue vertical lines represent the allowed η range for each lepton flavor. The numbers correspond to the number of raw MC events that fall within and outside of the allowed η range for each MC sample.

1514 muons can be found in Figure 5.25. Since all electrons have an associated jet in the calorimeters,
 1515 the $\Delta R(e, j)$ variable is not a good quantity to use for this custom OR.

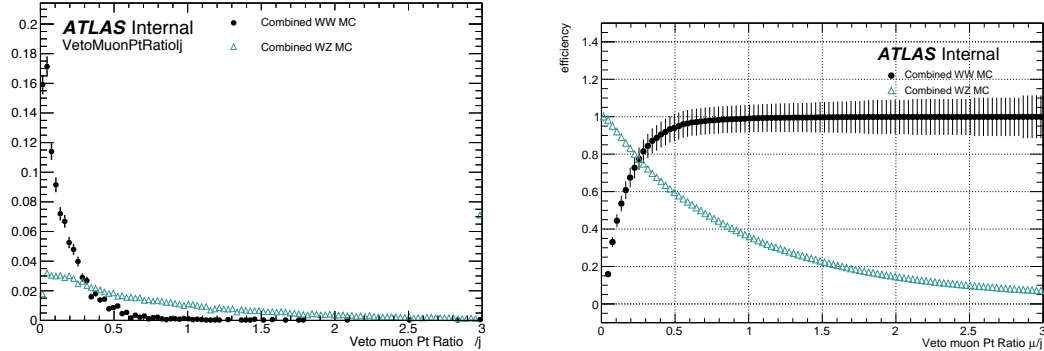


Figure 5.24: Distributions of $p_{T,\text{ratio}}(\mu, j)$ for EWK and QCD $W^\pm W^\pm jj$ signal (black) and WZ background (teal) for truth-matched third muons in events that pass the trilepton veto. Both distributions are normalized to unit area. The associated efficiency curves are on the right where efficiency is defined as the percentage of total events that would pass a cut on $p_{T,\text{ratio}}(\mu, j)$ at a given value on the x -axis.

1516 A workingpoint for the Custom OR was chosen by requiring 90% signal retention for muons
 1517 and 90% background rejection for electrons. The cut on electrons was allowed to be much tighter
 1518 because the number of signal events with a third electron is considerably smaller than for muons.
 1519 It should be re-emphasized the signal events that are present in Figures 5.24–5.26 do not represent
 1520 the full set of signal events, but only those with a real third lepton (which must come from some

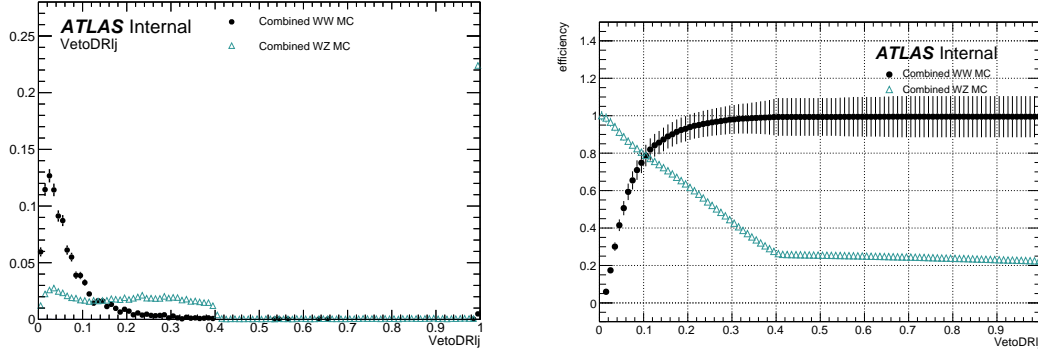


Figure 5.25: Distributions of $\Delta R(\mu, j)$ for EWK and QCD $W^\pm W^\pm jj$ signal (black) and WZ background (teal) for truth-matched third muons in events that pass the trilepton veto. Both distributions are normalized to unit area. The associated efficiency curves are on the right where efficiency is defined as the percentage of total events that would pass a cut on $\Delta R(\mu, j)$ at a given value on the x -axis.

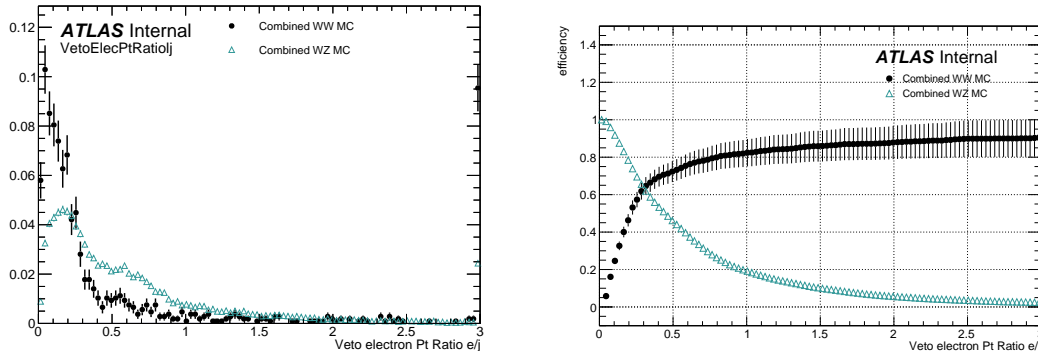


Figure 5.26: Distributions of $p_{T,\text{ratio}}(e, j)$ for EWK and QCD $W^\pm W^\pm jj$ signal (black) and WZ background (teal) for truth-matched third electrons in events that pass the trilepton veto. Both distributions are normalized to unit area. The associated efficiency curves are on the right where efficiency is defined as the percentage of total events that would pass a cut on $p_{T,\text{ratio}}(e, j)$ at a given value on the x -axis.

source other than the signal $W^\pm W^\pm jj$ process). For muons, an or of $p_{T,\text{ratio}}(\mu, j)$ and $\Delta R(\mu, j)$ is used to maximize the third lepton acceptance due to correlations between the quantities, as shown in Figure 5.27; for electrons, only a cut on $p_{T,\text{ratio}}(e, j)$ is used. The Custom OR workingpoint is outlined in Table 5.17.

Custom OR Definition	
Muons	$p_{T,\text{ratio}}(\mu, j) > 0.40$ or $\Delta R(\mu, j) > 0.15$
Electrons	$p_{T,\text{ratio}}(e, j) > 0.18$

Table 5.17: Custom OR definition. Leptons must pass this selection in order to be counted for the trilepton veto.

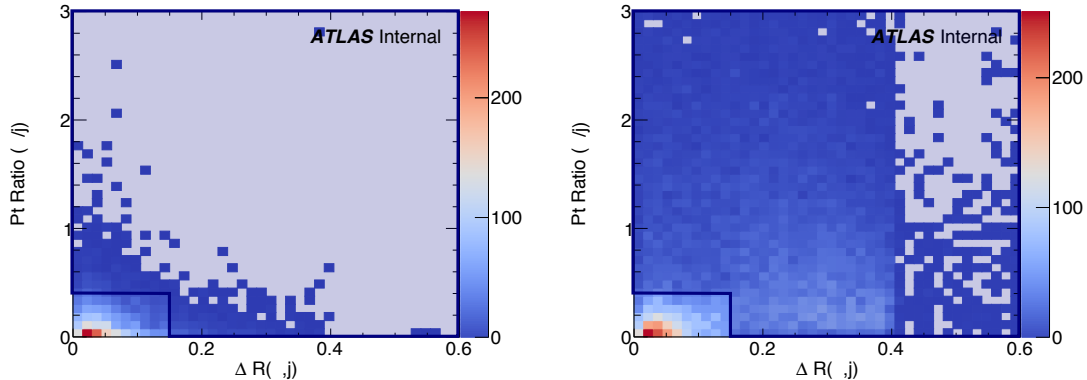


Figure 5.27: Two-dimensional plots of $p_{T,\text{ratio}}(\mu, j)$ vs $\Delta R(\mu, j)$ for truth-matched third muons in events that pass the trilepton veto for EWK and QCD $W^\pm W^\pm jj$ signal (left) and WZ background (right). The blue overlay indicates the area in which the third leptons will pass the custom OR and result in the event failing the trilepton veto.

Tests of the performance of the Custom OR yield promising results, with approximately 20% reduction in WZ background compared to less than 2% signal loss in the signal region. Unfortunately, due to differences between the primary analysis framework and the one used for testing, in practice the gains in WZ rejection are not nearly as substantial, and ultimately the Custom OR is not included in the final analysis. However, it is still a potentially useful tool for improving background rejection via lepton number vetoes in analyses with overly aggressive OR procedures.

5.4 Cross section measurement

The $W^\pm W^\pm jj$ EWK cross section is extracted from the signal region using a maximum-likelihood fit applied simultaneously to four m_{jj} bins in the signal region as well as to the low- m_{jj} and WZ

control regions. For the fit and cross section extraction, the signal region is defined as in Table 5.8 with the dijet invariant mass requirement raised to $m_{jj} > 500$ GeV. The low- m_{jj} region is defined to mirror the signal region exactly with the dijet invariant mass inverted to $200 < m_{jj} < 500$ GeV, and the WZ control region is defined previously in Section 5.3.1.

The signal and low- m_{jj} regions are split into six channels based on the flavor and charge of the dilepton pair: $\mu^+\mu^+$, $\mu^-\mu^-$, μ^+e^+ , μ^-e^- , e^+e^+ , and e^-e^- . This split by charge increases the sensitivity of the measurement due to the W^+/W^- charge asymmetry at hadron colliders favoring the production of W^+ bosons [75]. Since the signal events contain two W bosons, the signal strength compared to charge-symmetric backgrounds is much greater in the $++$ channels for both charges combined. The WZ control region is included in the fit as a single bin ($l^\pm l^\pm l^\pm$).

The maximum likelihood fit and cross section extractions are outlined in Sections 5.4.1 and 5.4.3, respectively. The results of the cross section measurement and of the analysis as a whole are presented in Section 5.6.

5.4.1 Maximum likelihood fit

TODO: This section is very similar to what is written in the support note... May need to put some work into flushing it out so it's not so close to copy-paste The number of predicted signal events in each channel c and m_{jj} bin b can be calculated from the SM predicted signal cross section $\sigma_{\text{theo}}^{\text{tot}}$, the total integrated luminosity \mathcal{L} , the signal acceptance \mathcal{A} , and the efficiency corrections $\mathcal{C}(\theta)$, where θ represents the set of nuisance parameters that parameterize the effects of each systematic uncertainty on the signal and background expectations. The acceptance and efficiency corrections will be covered in more detail in Section 5.4.2.

$$N_{cb}^{\text{sig}}(\theta) = \sigma_{\text{theo}}^{\text{tot}} \mathcal{A}_b \mathcal{C}_b(\theta) \mathcal{L} \quad (5.14)$$

A signal strength parameter μ is defined as the ratio of the measured cross section to the SM predicted cross section. The expected number of events in a given channel and bin can then be expressed as the sum of the estimated background ($N_{cb}^{\text{bkg}}(\theta)$) and the number of predicted signal events scaled by μ :

$$\begin{aligned} N_{cb}^{\text{exp}}(\theta) &= \mu N_{cb}^{\text{sig}}(\theta) + N_{cb}^{\text{bkg}}(\theta) \\ &= \mu \sigma_{\text{theo}}^{\text{tot}} \mathcal{A}_b \mathcal{C}_b(\theta) \mathcal{L} + N_{cb}^{\text{bkg}}(\theta) \end{aligned} \quad (5.15)$$

The nuisance parameters are constrained by Gaussian probability distribution functions, and the normalization of the WZ background mentioned in Section 5.3.1 is included in the fit as a free

1561 parameter. The expected yields for signal and background processes are adjusted by the set of
 1562 nuisance parameters within the constraints of the systematic uncertainties. The yields after the fit
 1563 correspond to the value that best matches the observed data.

1564 The number of events per channel and bin after the fit can be written as a sum of the predicted
 1565 event yields for each sample s :

$$\nu_{cb}(\phi, \theta, \gamma_{cb}) = \gamma_{cb} \sum_s [\eta_{cs}(\theta) \phi_{cs}(\theta) \lambda] h_{cbs}(\theta) \quad (5.16)$$

1566 In this equation, the fitted number of events in a given channel and bin is obtained by weighting
 1567 the histogram of predicted yields h_{cbs} by the product of a given luminosity λ and any normalization
 1568 factors ϕ_{cs} that may be given for each channel and sample. The input histogram and the normaliza-
 1569 tion factors may depend on the nuisance parameters θ taking into account sources of systematic
 1570 uncertainty. Uncertainties on the normalization factors $\eta_{cs}(\theta)$ are also included. Finally, bin-by-bin
 1571 scale factors γ_{cb} are included to parameterize the statistical uncertainties of the MC predictions.

1572 The binned likelihood function is given by a product of Gaussian functions for the luminosity
 1573 and for the background uncertainties and a product of Poisson functions for the number of observed
 1574 events in each bin and channel:

$$L(\mu|\theta) = \mathcal{G}(\mathcal{L}|\theta_{\mathcal{L}}, \sigma_{\mathcal{L}}) \cdot \prod_c \prod_b \mathcal{P}(N_{cb}^{\text{meas.}} | \nu_{cb}(\mu)) \prod_p \mathcal{G}(\theta_p^0 | \theta_p) \quad (5.17)$$

1575 where \mathcal{G} and \mathcal{P} are the Gaussian and Poisson functions, respectively. As before, \mathcal{L} represents the
 1576 integrated luminosity with uncertainty $\sigma_{\mathcal{L}}$ and associated nuisance parameter $\theta_{\mathcal{L}}$. The number of
 1577 measured events in a given bin and channel is represented by $N_{cb}^{\text{meas.}}$, and $\nu_{cb}(\mu)$ is the predicted
 1578 number of events defined in Equation 5.16 expressed as a function of the signal strength μ . Finally,
 1579 the set of nuisance parameters θ and any auxiliary measurements used to constrain them θ^0 are
 1580 multiplied for each parameter p .

1581 The profile likelihood ratio is defined as

$$q_{\mu} = -2 \ln \frac{L(\mu, \hat{\theta}_{\mu})}{L(\hat{\mu}, \hat{\theta})} \quad (5.18)$$

1582 with $\hat{\mu}$ and $\hat{\theta}$ as the unconditional maximum likelihood estimates and $\hat{\theta}$ as the conditional maximum
 1583 likelihood estimate for a given value of μ . The fitted signal strength $\hat{\mu}$ is obtained by maximizing
 1584 the likelihood function with respect to all parameters. The compatibility of the observed data
 1585 with the background-only hypothesis can then be calculated by setting $\mu = 0$. Observation of the
 1586 $W^{\pm}W^{\pm}jj$ EWK process is claimed if the data is found to be inconsistent with the background-only
 1587 hypothesis by more than 5σ .

1588 **5.4.2 Definition of the fiducial volume**

1589 Before extracting the cross section, it is necessary to define the fiducial volume, or the phase space
 1590 of measureable events. It is a subset of the total phase space defined by selection requirements
 1591 designed to mirror those applied in the analysis as closely as possible. The selection criteria for the
 1592 fiducial volume are listed in Table 5.18.

Fiducial region selection	
Lepton selection	Two prompt leptons (e, μ) $p_T > 27$ GeV and $ \eta < 2.5$ for both leptons Both leptons with the same electric charge Dilepton invariant mass $m_{ll} > 20$ GeV Dilepton separation $\Delta R(ll) > 0.3$
Missing transverse energy	Two neutrino system with $p_T^{\nu\nu} > 30$ GeV
Jet selection	At least two jets Leading jet $p_T > 65$ GeV Subleading jet $p_T > 35$ GeV Leading and subleading jet $ \eta < 4.5$ Jet-lepton separation $\Delta R(l, j) > 0.3$ Dijet invariant mass $m_{jj} > 500$ GeV Dijet separation $\Delta y_{jj} > 2.0$

Table 5.18: Definition of the fiducial volume.

1593 In MC simulations, the total phase space is generated, providing the total theoretical cross section
 1594 $\sigma_{\text{theo}}^{\text{tot}}$ and the total number of signal events $\mathcal{N}_{\text{sig}}^{\text{tot}}$ ¹⁶. After applying the fiducial selection at truth
 1595 level, the total number of signal events in the fiducial region $\mathcal{N}_{\text{sig}}^{\text{fid}}$ is obtained. An acceptance factor
 1596 \mathcal{A} is used to represent the efficiency of events falling in the fiducial region at truth level:

$$\mathcal{A} = \frac{\mathcal{N}_{\text{sig}}^{\text{fid}}}{\mathcal{N}_{\text{sig}}^{\text{tot}}} \quad (5.19)$$

1597 A correction factor \mathcal{C} is also necessary to translate from the truth level fiducial volume to the
 1598 reconstruction level signal region and is defined in terms of the number of reconstruction level MC
 1599 events in the signal region $N_{\text{sig}, \text{MC}}^{\text{SR}}$:

$$\mathcal{C} = \frac{N_{\text{sig}, \text{MC}}^{\text{SR}}}{\mathcal{N}_{\text{sig}}^{\text{fid}}} \quad (5.20)$$

1600 Since the fit is binned in m_{jj} , the acceptance and efficiency correction factors need to be as well.
 1601 Therefore, \mathcal{A}_i and \mathcal{C}_{ij} are written in terms of truth m_{jj} bins i and reconstruction m_{jj} bins j . A
 1602 graphical representation of these regions and the use of the acceptance and correction factors can
 1603 be seen in Figure 5.28.

¹⁶For the purpose of clarity, the number of events at truth level is represented by a script \mathcal{N} , and the number of events at reconstruction level uses a regular N .

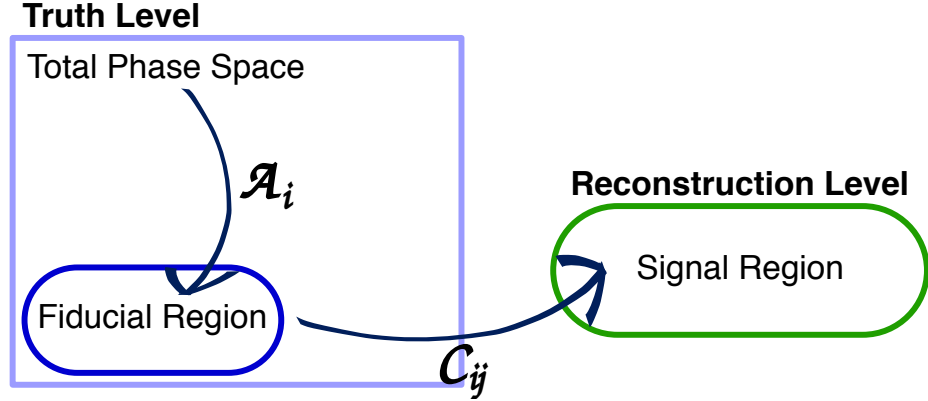


Figure 5.28: Visual representation of the different kinematic regions relevant to the cross section measurement. The acceptance factor \mathcal{A} converts from the truth level total phase space to the truth level fiducial region, and the efficiency correction \mathcal{C} translates the fiducial region in to the reconstruction level signal region.

1604 5.4.3 Cross section extraction

1605 The $W^\pm W^\pm jj$ EWK fiducial cross section is measured using the signal strength parameter μ that is
 1606 determined by the maximum likelihood fit. This parameter is dependent on the nuisance parameters
 1607 θ and can be written explicitly in terms of the measured and theoretical cross sections as:

$$\mu(\theta) = \frac{\sigma_{\text{meas}}^{\text{SR}}}{\sigma_{\text{theo}}^{\text{SR}}} \quad (5.21)$$

1608 In the simple case with only one bin, the equation for the total number of expected events in the
 1609 signal region first introduced in Equation 5.15 can be written as:

$$N_{\text{exp}}^{\text{SR}}(\theta) = \mu(\theta) \cdot \sigma_{\text{theo}}^{\text{tot}} \cdot \mathcal{L} \cdot \mathcal{A} \cdot \mathcal{C}(\theta) + N_{\text{bkg}}^{\text{SR}}(\theta) \quad (5.22)$$

1610 with the non-binned versions of \mathcal{A} and \mathcal{C} defined in Equations 5.19 and 5.20, respectively.

1611 If the measured fiducial cross section is written as:

$$\sigma_{\text{meas}}^{\text{fid}} = \mu \cdot \mathcal{A} \cdot \sigma_{\text{theo}}^{\text{tot}} \quad (5.23)$$

1612 then Equation 5.22 can be rearranged to read:

$$\sigma_{\text{meas}}^{\text{fid}} = \frac{N_{\text{exp}}^{\text{SR}}(\theta) - N_{\text{bkg}}^{\text{SR}}(\theta)}{\mathcal{L} \cdot \mathcal{C}(\theta)} \quad (5.24)$$

1613 The measured fiducial cross section can finally be rewritten in terms of $\hat{\mu}$, which is the best estimator
 1614 of the signal strength as extracted from the fit:

$$\begin{aligned} \sigma_{\text{meas}}^{\text{fid}} &= \hat{\mu}(\theta) \cdot \sigma_{\text{theo}}^{\text{tot}} \cdot \mathcal{A} \\ &= \hat{\mu}(\theta) \cdot \sigma_{\text{theo}}^{\text{fid}} \end{aligned} \quad (5.25)$$

1615 In practice, however, the cross section is not extracted from a single bin, and Equation 5.22
 1616 becomes for a single channel in truth and reconstruction level m_{jj} bins i and j , respectively:

$$N_{\text{exp}}^{\text{SR}}(\theta) = \mu(\theta) \cdot \sigma_{\text{theo}}^{\text{tot}} \cdot \mathcal{L} \cdot \sum_i \mathcal{A}_i \cdot \sum_j \mathcal{C}_{ij} + \sum_j N_{\text{bkg},j}^{\text{SR}}(\theta) \quad (5.26)$$

1617 where now the binned versions of \mathcal{A}_i and \mathcal{C}_{ij} are used. This equation can be extended to include all
 1618 the analysis channels by increasing the number of bins i and j . Additionally, it can be shown that
 1619 Equation 5.25 holds for this more complex case as well [40], provided care is taken to ensure that
 1620 all the uncertainties are handled properly.

1621 5.5 Summary of uncertainties

1622 Systematic uncertainties enter the final fit as nuisance parameters which can impact the estimated
 1623 signal and background yields and the shapes of the m_{jj} distributions. These uncertainties can arise
 1624 from the experimental methods or from the theoretical calculations used in the analysis. This section
 1625 summarizes the systematic uncertainties; the experimental uncertainties are detailed in Section 5.5.1,
 1626 and the theoretical uncertainties are covered in Section 5.5.2. The impacts of the systematic uncer-
 1627 tainties on the final cross section measurement are summarized in Table 5.19.

Source	Impact [%]
Reconstruction	± 4.0
Electrons	± 0.5
Muons	± 1.2
Jets and $E_{\text{T}}^{\text{miss}}$	± 2.8
b -tagging	± 2.0
Pileup	± 1.5
Background	± 5.0
Misid. leptons	± 3.9
Charge misrec.	± 0.3
WZ	± 1.3
$W^\pm W^\pm jj$ QCD	± 2.8
Other	± 0.8
Signal	± 3.6
Interference	± 1.0
EW Corrections	± 1.3
Shower, Scale, PDF & α_s	± 3.2
Total	± 7.4

Table 5.19: Impact of various systematic effects on the fiducial cross section measurement. The impact of a given source of uncertainty is computed by performing the fit with the corresponding nuisance parameter varied up or down by one standard deviation from its nominal value.

1628 5.5.1 Experimental uncertainties

1629 Experimental uncertainties include detector effects as well as uncertainties on the background es-
 1630 timation methods. Sources of systematic uncertainty on the measurement of physics objects are
 1631 listed in Table 5.20, grouped by the relevant object type. For backgrounds estimated from MC
 1632 simulations, variations in these sources of uncertainty are propagated through the analysis to obtain
 1633 the corresponding uncertainties on the event yields. Additional experimental uncertainties include
 1634 the integrated luminosity, the photon conversion rate from Section 5.3.2, and the data driven charge
 1635 misidentification and fake lepton background estimations from Sections 5.3.3 and 5.3.4.5, respec-
 1636 tively.

1637 The largest sources of experimental uncertainty on the MC estimations come from the jet-related
 1638 uncertainties and the b -tagging efficiency, while the largest uncertainty on the background estimation
 1639 comes from the fake factor. The effects of the uncertainties on the $W^\pm W^\pm jj$ EWK signal and the
 1640 dominant MC estimated background, WZ , are listed in Tables 5.21 and 5.22, respectively. Since
 1641 the overall contributions from other processes estimated with MC are small, the uncertainties on
 1642 these backgrounds have a lesser impact on the final measurement; these tables can be found in
 1643 Appendix B.1.

Experimental uncertainties	
Electrons	Energy resolution
	Energy scale
	Identification efficiency
	Isolation efficiency
	Reconstruction efficiency
	Trigger efficiency
Muons	Energy scale
	Identification efficiency
	Inner detector track resolution
	Muon spectrometer resolution
	Trigger efficiency
E_T^{miss}	Resolution
	Scale
Jets	Energy resolution
	Energy scale
	JVT cut efficiency
	b -tagging efficiency
Jets from pileup	

Table 5.20: List of sources of experimental uncertainties on the reconstruction of physics objects.

$W^\pm W^\pm jj$ EWK	$e^\pm e^\pm$ % Yield	$\mu^\pm e^\pm$ % Yield	$\mu^\pm \mu^\pm$ % Yield
Jet-related Uncertainties	2.28	2.22	2.28
b-tagging efficiency	1.81	1.76	1.74
Pile-up	0.48	0.97	2.42
Trigger efficiency	0.02	0.08	0.47
Lepton reconstruction/ID	1.45	1.14	1.83
MET reconstruction	0.26	0.17	0.21

Table 5.21: Impact of experimental uncertainties for the $W^\pm W^\pm jj$ EWK processes in all channels.

WZ	$e^\pm e^\pm$ % Yield	$\mu^\pm e^\pm$ % Yield	$\mu^\pm \mu^\pm$ % Yield
Jet-related Uncertainties	9.58	5.03	8.45
b-tagging efficiency	2.49	2.23	2.40
Pile-up	2.99	3.49	3.33
Trigger efficiency	0.03	0.09	0.43
Lepton reconstruction/ID	1.52	1.24	3.07
MET reconstruction	0.93	0.79	1.63

Table 5.22: Impact of experimental uncertainties for the WZ process in all channels.

1644 5.5.2 Theoretical uncertainties

1645 It is also necessary to consider uncertainties on the theoretical predictions in the fiducial region. They
 1646 include the choice of PDF set, the value of the strong coupling constant α_s , the renormalization
 1647 scale μ_R , the factorization scale μ_F , and the parton showering. The size of these uncertainties are
 1648 measured by generating new samples with variations in a chosen parameters and comparing them
 1649 to samples using the nominal choice of the parameter. Internal variations on the PDF sets or using
 1650 a different set entirely results in a relative uncertainty of up to 2.25% on the nominal sample. The
 1651 impact from varying α_s is very small, on the order of < 0.01%. The factorization and renormalization
 1652 scales are independently varied between 0.5-2.0 from their nominal values of 1.0. This results in
 1653 relative uncertainties on the prediction of up to 15%. Finally, varying the parameters in the parton
 1654 showering results in up to 8% uncertainty.

1655 5.5.2.1 Uncertainties from EWK-QCD interference

1656 As mentioned in Section 5.0.2, $W^\pm W^\pm jj$ production consists of both EWK processes. The two
 1657 production modes cannot be naively separated due to cross terms in the matrix element calculation.
 1658 These cross terms are referred to as *interference* terms. Since the $W^\pm W^\pm jj$ EWK production is
 1659 the focus of the analysis, and the signal region is designed to preferentially select those events, it is
 1660 important to measure the size of the EWK-QCD interference contributions.

1661 The interference effects are estimated using the `MadGraph` MC generator, as it has a feature that
 1662 allows direct modelling of the interference term. This allows four samples to be generated:

- 1663 1. Inclusive: All available diagrams are used in the matrix element calculation
 1664 2. EWK only: Only EWK diagrams ($\mathcal{O}(\alpha_{\text{EWK}}) = 4$) are used
 1665 3. QCD only: Only QCD diagrams ($\mathcal{O}(\alpha_s) = 2 \otimes \mathcal{O}(\alpha_{\text{EWK}}) = 2$) are used
 1666 4. Interference: Only the interference terms are used

1667 A minimal set of generator level cuts, listed in Table 5.23, is applied in order to avoid biasing the
 1668 sample towards either production mode. The cross sections for each of the four channels can be
 1669 found in Table 5.24. The size of the interference is found to be approximately 6% of the total cross
 1670 section and is taken as a systematic uncertainty.

Generator level cuts
$\Delta\eta_{jj} < 10$
Jet $p_{\text{T}} > 20$ GeV
$M_{jj} > 10$ GeV

Table 5.23: The set of generator level cuts used for generating the interference samples with `MadGraph`.

Sample	σ (fb)
Inclusive	3.646 ± 0.0012
EWK only	2.132 ± 0.0005
QCD only	1.371 ± 0.0008
Interference	0.227 ± 0.0002

Table 5.24: Cross sections for each different $W^\pm W^\pm jj$ production mode (inclusive, EWK only, QCD only, and interference only) generated using `MadGraph`. The cross sections are calculated using a minimal set of generator level cuts from events where the W decays to a muon.

1671 5.6 Results

1672 After running the full analysis chain, the event yields in the signal region, low- m_{jj} control region,
 1673 and WZ control region as well as associated nuisance parameters representing the uncertainties are
 1674 passed to the maximum likelihood fit. From this fit, the normalization factor for the WZ control
 1675 region μ_{WZ} and the signal strength parameter in the signal region μ_{obs} are determined, and the
 1676 predicted yields in each input bin have been shifted according to the process detailed in Section 5.4.1.

1677 The WZ normalization factor is measured to be:

$$\mu_{WZ} = 0.88^{+0.07}_{-0.07}(\text{stat})^{+0.31}_{-0.21}(\text{theory})^{+0.22}_{-0.11}(\text{sys}) \quad (5.27)$$

1678 and is constrained primarily by the number of data events in the WZ control region. The observed
 1679 signal strength of $W^\pm W^\pm jj$ EWK production, defined in Equation 5.21, is extracted from the fit
 1680 and measured with respect to the prediction of the **SHERPA v2.2.2** MC generator:

$$\mu_{\text{obs}} = 1.45^{+0.25}_{-0.24}(\text{stat})^{+0.06}_{-0.08}(\text{theory})^{+0.27}_{-0.22}(\text{sys}) \quad (5.28)$$

1681 This corresponds to a rejection of the background-only hypothesis with a significance of 6.9σ .

1682 The observed number of data events are compared to the predicted signal and background yields
 1683 in the signal region in Table 5.25 before applying the fit and in Table 5.26 after the fit. The m_{jj}
 1684 distributions for data and prediction are shown in Figure 5.29 after the fit, and the fitted event
 1685 yields in the low- m_{jj} and WZ control regions are shown in Figure 5.30. Additional distributions
 1686 can be found in Appendix B.

	e^+e^+	e^-e^-	μ^+e^+	$\mu^\pm e^\pm m$	$\mu^+\mu^+$	$\mu^-\mu^-$	combined
WZ	1.9 ± 0.6	1.3 ± 0.4	14 ± 4	8.9 ± 2.6	5.5 ± 1.6	3.6 ± 1.1	35 ± 10
Non-prompt	4.1 ± 2.3	2.3 ± 1.7	9 ± 5	6 ± 4	0.57 ± 0.15	0.67 ± 0.25	23 ± 10
e/γ conversions	1.74 ± 0.29	1.8 ± 0.4	6.1 ± 1.6	3.7 ± 0.8	—	—	13.4 ± 2.5
Other prompt	0.17 ± 0.05	0.14 ± 0.04	0.90 ± 0.19	0.60 ± 0.14	0.36 ± 0.10	0.19 ± 0.05	2.4 ± 0.5
$W^\pm W^\pm jj$ QCD	0.38 ± 0.13	0.16 ± 0.05	3.0 ± 1.0	1.2 ± 0.4	1.8 ± 0.6	0.76 ± 0.25	7.3 ± 2.5
Expected background	8.2 ± 2.4	5.7 ± 1.8	33 ± 7	21 ± 5	8.2 ± 1.8	5.3 ± 1.2	81 ± 14
$W^\pm W^\pm jj$ EWK	3.8 ± 0.6	1.49 ± 0.22	16.5 ± 2.5	6.5 ± 1.0	9.1 ± 1.4	3.5 ± 0.5	41 ± 6
Data	10	4	44	28	25	11	122

Table 5.25: Table of the data and prediction event yields in the signal region before the fit. Numbers are shown for the six lepton flavor and charge channels and for all channels combined. Here the WZ background yields are normalized to the data in the WZ control region. The background estimations from the fake factor are included in the “Non-prompt” category, and backgrounds from $V\gamma$ production and electron charge misidentification are combined in the “ e/γ conversions” category. Finally, ZZ , VVV , and $t\bar{t}V$ backgrounds are combined in the “Other prompt” category.

1687 The last ingredient necessary to measure the $W^\pm W^\pm jj$ EWK cross section is the theory predicted
 1688 cross section in the fiducial region defined in Table 5.18. **SHERPA v2.2.2** is used for the calculation,
 1689 and the cross section in the total generator phase space is 40.81 ± 0.05 fb, and the fiducial cross section
 1690 is 2.01 ± 0.02 fb. This corresponds to an acceptance factor of $\mathcal{A} = 0.0493 \pm 0.0002$. Uncertainties on
 1691 the simulation are estimated using variations of the scale, parton shower, and PDF set. The final
 1692 prediction used in the cross section measurement including uncertainties from Section 5.5.2 is:

$$\sigma_{\text{SHERPA}}^{\text{fid}} = 2.01 \pm 0.02(\text{stat})^{+0.29}_{-0.23}(\text{scale})^{+0.16}_{-0.02}(\text{parton shower})^{+0.05}_{-0.03}(\text{PDF}) \text{ fb} \quad (5.29)$$

	e^+e^+	e^-e^-	μ^+e^+	$\mu^\pm e^\pm m$	$\mu^+\mu^+$	$\mu^-\mu^-$	combined
WZ	1.49 ± 0.30	1.10 ± 0.26	11.7 ± 1.7	8.0 ± 1.3	5.0 ± 0.6	3.5 ± 0.6	31 ± 4
Non-prompt	2.2 ± 1.3	1.2 ± 0.7	5.7 ± 2.8	4.5 ± 1.8	0.57 ± 0.06	0.65 ± 0.14	15 ± 6
e/γ conversions	1.6 ± 0.4	1.6 ± 0.5	6.3 ± 1.6	4.3 ± 1.1	—	—	13.8 ± 2.9
Other prompt	0.16 ± 0.04	0.14 ± 0.04	0.90 ± 0.19	0.63 ± 0.13	0.39 ± 0.09	0.22 ± 0.05	2.4 ± 0.5
$W^\pm W^\pm jj$ QCD	0.35 ± 0.13	0.15 ± 0.05	2.9 ± 1.0	1.2 ± 0.4	1.8 ± 0.6	0.76 ± 0.25	7.2 ± 2.4
Expected background	5.8 ± 1.5	4.1 ± 1.1	27 ± 4	18.7 ± 2.6	7.7 ± 0.8	5.1 ± 0.6	69 ± 7
$W^\pm W^\pm jj$ EWK	5.6 ± 1.0	2.2 ± 0.4	24 ± 5	9.4 ± 1.8	13.5 ± 2.5	5.2 ± 1.0	60 ± 11
Data	10	4	44	28	25	11	122

Table 5.26: Table of the data and prediction event yields in the signal region after the fit. Numbers are shown for the six lepton flavor and charge channels and for all channels combined. The background estimations from the fake factor are included in the “Non-prompt” category, and backgrounds from $V\gamma$ production and electron charge misidentification are combined in the “ e/γ conversions” category. Finally, ZZ , VVV , and $t\bar{t}V$ backgrounds are combined in the “Other prompt” category.

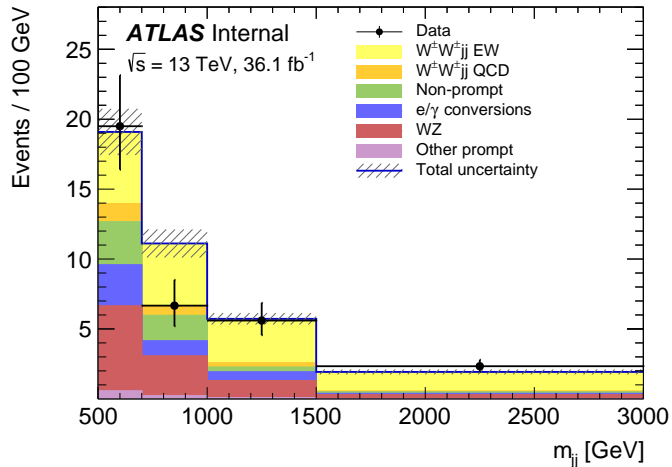


Figure 5.29: The dijet invariant mass m_{jj} distributions for data and predicted signal and background in the signal region after the fit. The shaded band represents the statistical and systematic uncertainties added in quadrature. Note that the bins have been scaled such that they represent the number of events per 100 GeV in m_{jj} . The background estimations from the fake factor are included in the “Non-prompt” category, and backgrounds from $V\gamma$ production and electron charge misidentification are combined in the “ e/γ conversions” category. Finally, ZZ , VVV , and $t\bar{t}V$ backgrounds are combined in the “Other prompt” category.

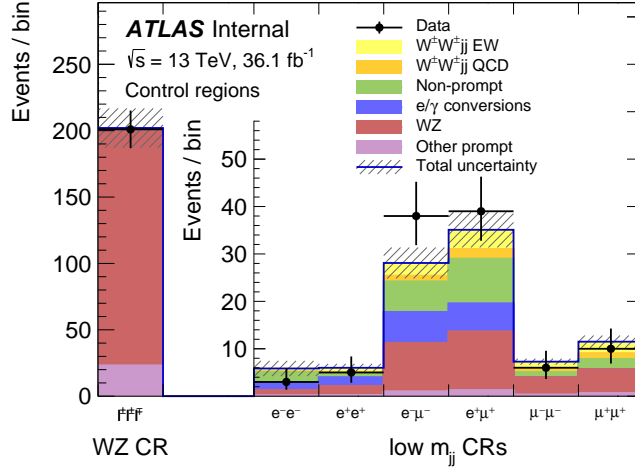


Figure 5.30: The event yields for data and predicted signal and background in the WZ and low- m_{jj} control regions after the fit. The shaded band represents the statistical and systematic uncertainties added in quadrature. The background estimations from the fake factor are included in the “Non-prompt” category, and backgrounds from $V\gamma$ production and electron charge misidentification are combined in the “ e/γ conversions” category. Finally, ZZ , VVV , and $t\bar{t}V$ backgrounds are combined in the “Other prompt” category.

1693 Combining this **SHERPA** prediction with the measured signal strength μ_{obs} from Equation 5.28,
 1694 the measured fiducial cross section $\sigma_{\text{meas}}^{\text{fid}}$ can be calculated using Equation 5.25:

$$\sigma_{\text{meas}}^{\text{fid}} = 2.91^{+0.51}_{-0.47}(\text{stat})^{+0.12}_{-0.16}(\text{theory})^{+0.24}_{-0.23}(\text{sys})^{+0.08}_{-0.06}(\text{luminosity}) \text{ fb} \quad (5.30)$$

1695 A plot comparing the measured fiducial cross section to two theoretical calculations is shown in
 1696 Figure 5.31. The measured value is compared to the **SHERPA v2.2.2** prediction used to calculate
 1697 μ_{obs} as well as to **POWHEG-BOX v2**. As mentioned in Section 5.1.1, this **POWHEG** sample does not
 1698 include the resonant triboson diagrams and is only used here for a visual comparison.

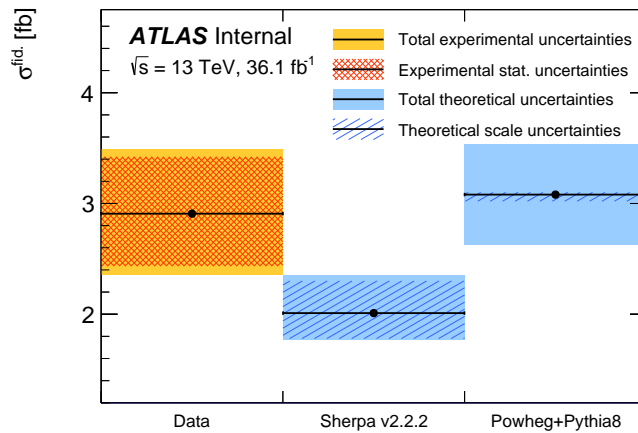


Figure 5.31: Comparison of the measured $W^\pm W^\pm jj$ EWK fiducial cross section with theoretical calculations from **SHERPA v2.2.2** and **POWHEG-BOX v2**. The light orange band represents the total experimental uncertainty on the measured value, and the dark orange hashed band is the statistical uncertainty. For the simulations, the light blue band represents the total theoretical uncertainty, and the dark blue hashed band are the scale uncertainties. The theory predictions do not include the interference between the EWK and QCD production.

CHAPTER 6

Prospects for same-sign WW at the High Luminosity LHC

1702 On December 3, 2018, Run 2 of the LHC officially ended, and the collider was shut down to begin
 1703 the first of two scheduled extended maintenance periods [76]. During these two long shutdowns,
 1704 the Phase-I and Phase-II upgrades of the LHC and ATLAS will occur in order to prepare for the
 1705 High-Luminosity LHC (HL-LHC) which is scheduled to begin operation in 2026 [77].

1706 The HL-LHC is planned to run at a center-of-mass energy of $\sqrt{s} = 14$ TeV with an instantaneous
 1707 luminosity of $\mathcal{L} = 5 \times 10^{34}$ cm $^{-2}$ s $^{-1}$ with up to 200 collisions per beam-crossing. Over the course
 1708 of operation, the HL-LHC is expected to collect a total integrated luminosity of $\mathcal{L} = 3000$ fb $^{-1}$ by
 1709 2035 [78]. **TODO: Compare to current LHC numbers?**

1710 These run conditions will be much harsher than what ATLAS has experienced so far, and there
 1711 are several upgrades planned for the detector to operate in the high luminosity environment. Most
 1712 notably, the entire ID will be replaced with an all-silicon tracker which will extend the coverage from
 1713 $|\eta| \leq 2.7$ up to $|\eta| \leq 4.0$. This will allow for reconstruction of charged particle tracks which can
 1714 in turn be matched to clusters in the calorimeters for electron identification or forward jet tagging
 1715 [79].

1716 The upgraded detector, the higher beam energy, and the increased volume of data to be collected
 1717 provides the opportunity to measure rarer processes with a much higher precision than what was
 1718 possible in Run 1. Same-sign $W^\pm W^\pm jj$ production, is one such process. With greater statistics,
 1719 the accuracy of the cross section measurement can be improved over the 13 TeV analysis detailed in
 1720 Chapter 5, and it also will allow for more detailed physics studies, such as measuring the polarization
 1721 of the W bosons. A measurement of the longitudinal polarization of the scattered W bosons has

not yet been possible, but it remains of great interest due to its sensitivity to electroweak symmetry breaking [80]. The analysis detailed in this chapter is based off of the 2018 ATLAS HL-LHC $W^\pm W^\pm jj$ prospects study [81] which is itself an extension of the 2017 ATLAS study [82]. **TODO:** mention CMS’s study + yellow report?

6.0.1 Analysis Overview

The experimental signature of interest is identical to the 13 TeV analysis: two prompt leptons (either electrons or muons) with the same charge, missing transverse energy, and two high energy, forward jets. These jets are again required to have a large angular separation and a high combined invariant mass to preferentially select EWK- over QCD-produced $W^\pm W^\pm jj$ events.

Background processes are again similar to the 13 TeV analysis and are summarized again here. The dominant source of prompt background from $WZ+jets$ events where both bosons decay leptonically. If the lepton from the Z -decay with opposite charge from the W falls outside of the detector acceptance or is not identified, the remainder could appear to be a $W^\pm W^\pm jj$ signal event. To a lesser extent, $ZZ+jets$ events can enter the signal region in much the same way provided two leptons are “lost”. Other prompt sources include $t\bar{t}+V$ and multiple parton interactions, however these processes do not contribute much. These prompt backgrounds are expected to contribute less than in Run 2 with the addition of forward tracking in the upgraded ATLAS detector. Jets mis-reconstructed as leptons or leptons from hadronic decays (such as $t\bar{t}$ and $W+jets$ production) comprise the non-prompt lepton background. Lastly, events with two prompt, opposite-charge electrons can appear as a same-sign event provided one of the electrons is mis-reconstructed as the wrong charge.

In this analysis, the EWK production of $W^\pm W^\pm jj$ is studied in the context of the planned HL-LHC run conditions and upgraded ATLAS detector. An optimized event selection (referred to as the *optimized selection*) is also explored in an effort to gain increased signal significance over the *default selection*. The cross section of the inclusive EWK production is measured for both the default and optimized selections, and the extraction of the longitudinal scattering significance is measured with the optimized selection.

6.1 Theoretical motivation

The theoretical motivation for studying the ssWW process—and VBS in general—is detailed in Section 5.0.2. Since it is specifically the scattering of *longitudinally polarized* vector bosons that violates

1752 unitarity without a SM Higgs boson, a direct measurement of this cross section will be very useful
 1753 for understanding how the Higgs unitarizes the process [80].

1754 6.1.1 Experimental sensitivity to longitudinal polarization

1755 **TODO:** mention that since there are so many polarization possibilities, a large integrated luminosity
 1756 is needed to measure just one of them individually There are three possible polarization states for
 1757 a massive vector boson: two transverse (+ or -) and one longitudinal (0). Therefore, in a system
 1758 with two W bosons, the overall polarization can be purely longitudinal (00), purely transverse (++,
 1759 --, and +-), or mixed (+0 and -0). The three combinations will be referred to as LL , TT , and
 1760 LT respectively.

1761 In order extract the longitudinal scattering component, it is necessary to find variables that
 1762 distinguish the LL from the TT and LT . Several were studied, and those with the best discriminating
 1763 power between the polarizations are the leading and subleading lepton p_T as well as the azimuthal
 1764 separation ($|\Delta\phi_{jj}|$) of the two VBS jets. The LL events prefer lower p_T for both signal leptons
 1765 (see Figure 6.1), which motivates keeping cuts on these quantities as low as possible in the event
 1766 selection. In the case of $|\Delta\phi_{jj}|$, the LL events generally had a larger dijet separation (see Figure 6.2),
 1767 and this variable is used in a binned likelihood fit to extract the longitudinal scattering significance.

1768 6.2 Monte Carlo samples

1769 As no real HL-LHC data will be available for many years, all signal and background processes are
 1770 modeled using MC simulations generated at $\sqrt{s} = 14$ TeV, with the event yields scaled to the
 1771 anticipated HL-LHC integrated luminosity of $\mathcal{L} = 3000 \text{ fb}^{-1}$. The MC samples used in the analysis
 1772 are generated at particle-level and have not been run through the typical full simulation of the
 1773 ATLAS detector. Instead, smearing functions derived from a **GEANT4** simulation of the upgraded
 1774 ATLAS detector are used to estimate detector effects such as momentum resolution. In addition,
 1775 pileup events are fully simulated. The MC samples used in this analysis are summarized in Table 6.1.

1776 The signal sample consists of both VBS and non-VBS electroweak (EWK) $W^\pm W^\pm jj$ production,
 1777 and it is simulated with the **Madgraph5_aMC@NLO** generator using the NNPDF3.0 PDF set and in-
 1778 terfaced with **PYTHIA v8** [83] for hadronization and parton showering. To study the longitudinal
 1779 polarization more directly, two additional **Madgraph5_aMC@NLO** $W^\pm W^\pm jj$ samples are used: one
 1780 containing only the longitudinal contribution (LL) and a second containing the transverse (TT) and
 1781 mixed (LT) contributions.

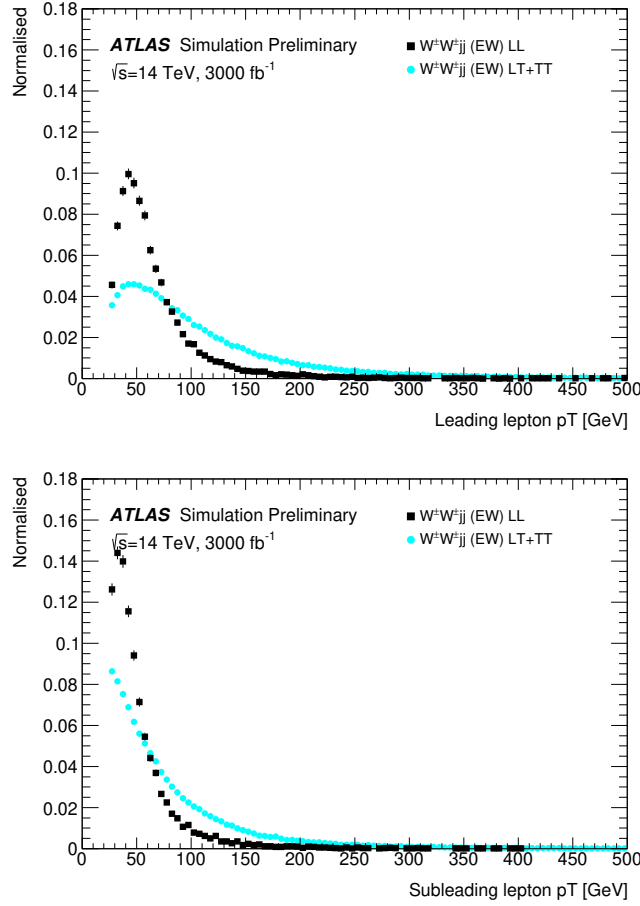


Figure 6.1: Comparison of the leading (top) and subleading (bottom) lepton p_T distributions for purely longitudinal (LL, black) and mixed polarization (LT+TT, cyan) $W^\pm W^\pm jj$ events.

1782 There are many other processes that can produce the same final state as the $W^\pm W^\pm jj$ and
 1783 must also be accounted for using MC simulations. WZ events are generated using **SHERPA v2.2.0**,
 1784 which includes up to one parton at NLO in the strong coupling constant and up to three addi-
 1785 tional partons at LO. Both EWK and QCD production are included in these samples. ZZ and
 1786 triboson VVV ($V = W, Z$) events are generated using **SHERPA v2.2.2** with up to two additional
 1787 partons in the final state. For the triboson backgrounds, the bosons can decay leptonically or
 1788 hadronically. $W+jets$ backgrounds are generated for electron, muon, and tau final states at LO
 1789 with **Madgraph5_aMC@NLO** and the **NNPDF3.0** set with showering from **PYTHIA v8**. $Z+jets$ events are
 1790 produced using **POWHEG-BOX v2** and the **CT10** PDF set interfaced with **PYTHIA v8**. Finally, $t\bar{t}$ and
 1791 single-top events are generated using **POWHEG-BOX** with showering from **PYTHIA v6**.

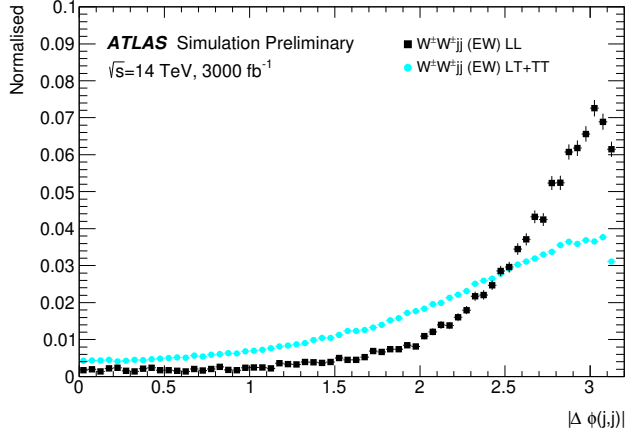


Figure 6.2: Comparison of the azimuthal dijet separation ($|\Delta\phi_{jj}|$) for purely longitudinal (LL, black) and mixed polarization (LT+TT, cyan) $W^\pm W^\pm jj$ events.

Process	Generator	Comments
$W^\pm W^\pm jj$ (EWK)	Madgraph5_aMC@NLO	Signal sample
$W^\pm W^\pm jj$ (QCD)	Madgraph5_aMC@NLO	
$W^\pm W^\pm jj$ (LL)	Madgraph5_aMC@NLO	Pure longitudinal polarization sample
$W^\pm W^\pm jj$ (TT+LT)	Madgraph5_aMC@NLO	Mixed and transverse polarization sample
Diboson	SHERPA v2.2.0	WZ events
	SHERPA v2.2.2	ZZ events
Triboson	SHERPA v2.2.2	
$W+jets$	Madgraph5_aMC@NLO	
$Z+jets$	POWHEG-BOX v2	
$t\bar{t}$	POWHEG-BOX	
Single top	POWHEG-BOS	

Table 6.1: Summary of MC samples used in the analysis.

6.3 Background estimations

In this analysis, all background contributions are estimated using MC simulations. Backgrounds such as electron charge misidentification and fake electrons from jets (which are traditionally estimated using data-driven techniques) are estimated using a set of parameterization functions applied to the MC. These functions calculate the probability that an electron is assigned the wrong charge or a jet is mis-reconstructed as an electron parameterized by the p_T and η of the electron or jet. The probabilities are derived from studies on expected electron performance with the upgraded ATLAS detector [84].

Processes involving two W and Z bosons are grouped together as *diboson* backgrounds, with the

exception of $W^\pm W^\pm jj$ events produced via QCD interactions, which are kept separate. Similarly, all backgrounds with three vector bosons are combined and labeled as *triboson*. Any $W+jets$ or top events that pass selection and do not contain a fake electron, as well as any $Z+jets$ events without an electron identified as having its charge misidentified are combined as *other non-prompt* backgrounds.

6.3.1 Truth-based isolation

To properly calculate particle isolation, it requires information from several detector subsystems including tracking and calorimeter responses. Since the MC samples used in this analysis have not been run through a full detector simulation, it is not possible to construct the canonical isolation variables used in analyses. At truth-level, this is generally not a serious concern as p_T signal leptons tend to be well isolated to begin with. However, isolation is one of the most powerful tools for rejecting leptons from non-prompt sources such as top events, which are produced in association with additional nearby particles from b and c quark decays. In this analysis, with the absence of any sort of isolation requirement, contributions from top backgrounds (including single top, $t\bar{t}$ and $t\bar{t} + V$) are more than an order of magnitude higher than expected.

As a result, it is necessary to find one or more quantities that are comparable to the isolation information that is available in fully-simulated samples. Analogues to track- and calorimeter-based isolation variables are constructed by summing the momentum and energy, respectively, of stable truth particles with $p_T > 1$ GeV within a specified radius of each signal lepton. For the track-based isolation, only charged truth particles are used; both charged and neutral particles (excluding neutrinos) are included for the calorimeter-based isolation. Ultimately, a set of isolation cuts are chosen that are similar to those recommended by ATLAS for Run 2 analyses. The truth-based isolation requirements are listed in Table 6.2.

	Electron Isolation	Muon Isolation
Track-based isolation cone size	$\Delta R < 0.2$	$\Delta R < 0.3$
Track-based isolation requirement	$\sum p_T/p_T^e < 0.06$	$\sum p_T/p_T^\mu < 0.04$
Calorimeter-based isolation cone size	$\Delta R < 0.2$	$\Delta R < 0.2$
Calorimeter-based isolation requirement	$\sum E_T/p_T^e < 0.06$	$\sum E_T/p_T^\mu < 0.15$

Table 6.2: Truth-based isolation requirements for electrons and muons.

The truth-based isolation requirement reduces the top background by over 99%, and the percentage of the total background consisting of top events is reduced from 83% to 2%. Additional details on the truth-based isolation studies are presented in Appendix A.

1826 **6.4 Object and event selection**

1827 **6.4.1 Object selection**

1828 Electrons and muons are preselected to have $p_T > 7$ and 6 GeV, respectively, and $|\eta| \leq 4.0$. The
 1829 likelihood of a given lepton to pass the trigger and identification requirements is estimated by
 1830 calculating an efficiency dependent on the p_T and η of the lepton. The leptons are also required to
 1831 pass the isolation criteria detailed in Table 6.2. Jets that have been tagged as a fake electron by the
 1832 functions described in Section 6.3 are treated as electrons for the purpose of the object selection and
 1833 are subject to the same criteria. In order to be considered a signal lepton, an additional requirement
 1834 of $p_T > 25$ GeV is applied on top of the preselection. The two highest p_T leptons passing this
 1835 selection are chosen to be the leading and subleading signal leptons.

1836 Jets are clustered using the anti- k_t algorithm [67] from final-state particles within a radius of
 1837 $\Delta R = 0.4$ (excluding muons and neutrinos). Jets are required to have $p_T > 30$ GeV and lie within
 1838 $|\eta| < 4.5$, with an additional cut of $p_T > 70$ GeV for jets above $|\eta| \geq 3.8$ in order to suppress jets
 1839 from pileup interactions. Jets overlapping with a preselected electron within $\Delta R(e, j) < 0.05$ are
 1840 removed in order to prevent double counting. The two highest p_T jets are defined as the leading
 1841 and subleading *tag jets*.

1842 **6.4.2 Event selection**

1843 The default event selection is summarized in Table 6.3 and described here. Exactly two signal
 1844 leptons are required with the same electric charge and separated from each other by $\Delta R(l l) > 0.3$.
 1845 In order to suppress contributions from Drell-Yan backgrounds, the two signal leptons must have
 1846 an invariant mass m_{ll} greater than 20 GeV. Additionally, if both signal leptons are electrons, their
 1847 mass must be at least 10 GeV from the Z -boson mass in order to reduce background from Z -boson
 1848 decays¹⁷. The event is required to have at least 40 GeV of missing transverse energy (E_T^{miss}) to
 1849 account for the two neutrinos from the W decays. Events with additional preselected leptons are
 1850 vetoed, which greatly reduces WZ and ZZ backgrounds.

1851 Each event must have at least two jets, and both tag jets are required to not overlap with the
 1852 signal leptons, and there is a veto on events with one or more b -jets. In order to preferentially select
 1853 EWK production, the tag jets are also required to have a large separation between them and a large

¹⁷The electron charge misidentification rate in the upgraded ATLAS detector is estimated to be high enough that contributions from $Z \rightarrow ee$ backgrounds are non-negligible.

1854 invariant mass. Finally, a cut on the lepton centrality¹⁸, ζ , defined in Equation 6.1 enhances the
1855 EWK $W^\pm W^\pm jj$ signal.

$$\zeta = \min[\min(\eta_{\ell 1}, \eta_{\ell 2}) - \min(\eta_{j 1}, \eta_{j 2}), \max(\eta_{j 1}, \eta_{j 2}) - \max(\eta_{\ell 1}, \eta_{\ell 2})] \quad (6.1)$$

Selection requirement	Selection value
Lepton kinematics	$p_T > 25 \text{ GeV}$ $ \eta \leq 4.0$
Jet kinematics	$p_T > 30 \text{ GeV}$ for $ \eta \leq 4.5$ $p_T > 70 \text{ GeV}$ for $ \eta > 3.8$
Dilepton charge	Exactly two signal leptons with same charge
Dilepton separation	$\Delta R_{l,l} \geq 0.3$
Dilepton mass	$m_{ll} > 20 \text{ GeV}$
Z boson veto	$ m_{ee} - m_Z > 10 \text{ GeV}$ (ee -channel only)
E_T^{miss}	$E_T^{\text{miss}} > 40 \text{ GeV}$
Jet selection	At least two jets with $\Delta R_{l,j} > 0.3$
b jet veto	$N_{b\text{-jet}} = 0$
Dijet separation	$\Delta \eta_{jj} > 2.5$
Trilepton veto	No additional preselected leptons
Dijet mass	$m_{jj} > 500 \text{ GeV}$
Lepton-jet centrality	$\zeta > 0$

Table 6.3: Summary of the signal event selection.

1856 6.5 Selection optimization

1857 An upgraded detector along with an increase in center of mass energy and integrated luminosity
1858 provides an opportunity to study whether the event selection can be optimized to improve the signal
1859 to background ratio.

1860 6.5.1 Random grid search algorithm

1861 The chosen method for optimizing the event selection is a cut-based algorithm known as the Random
1862 Grid Search (RGS) [85]. Consider a simple case of two variables x and y chosen to differentiate signal
1863 from background. In order to be considered a signal event, a given event would be required to pass
1864 a set of selection criteria, called a *cut point*: $c = \{x > x_c, y > y_c\}$. A simple method to choose the
1865 optimal cut point (i.e. the “best” values of the cuts x_c and y_c) would be to construct an $n \times m$

¹⁸ ζ is a measurement of whether the two signal leptons lie between the two tagging jets in η , as is preferred by the VBS topology.

1866 rectangular grid in x and y consisting of points $(x_0, y_0), (x_1, y_1), \dots, (x_n, y_m)$, as in Figure 6.3. One
 1867 can then choose a cut point $c_k = \{x > x_i, y > y_j\}$ that maximizes the signal significance as measured
 1868 by a chosen metric. This would be considered a *rectangular grid search*.

1869 While effective in principle, a rectangular grid search comes with two major drawbacks:

- 1870 1. The algorithm scales exponentially as the number of variables to be optimized increases, as
 1871 this is effectively increasing the dimensionality of the grid. In the simple case of a square grid
 1872 with N bins per variable v , the number of cut points to be evaluated grows as N^v .
 1873 2. Signal and background samples are rarely evenly distributed over the entire grid, resulting
 1874 in many cut points being sub-optimal and evaluating them would be a waste of computing
 1875 resources.

1876 To combat these limitations, the RGS algorithm constructs a grid of cut points directly from
 1877 the signal sample itself. In the two-dimensional example, this means that the variables x_i and y_j
 1878 making up the cut point $c_k = \{x > x_i, y > y_j\}$ take their values directly from a given signal event.
 1879 This has the benefit of creating a *random grid* of cut points that is biased towards regions of high
 1880 signal concentration by construction. This reduces the need for exponentially increasing numbers of
 1881 cut points while ensuring that computing resources are not wasted in regions with few to no signal
 1882 events. An example of the the two-dimensional random grid is shown in Figure 6.4.

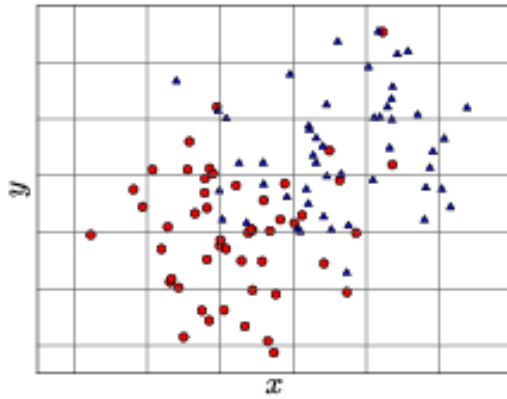


Figure 6.3: A visual representation of a rectangular grid search algorithm. The signal events are the blue triangles, and the red circles are the background events. **TODO: replace with own figure**

1883 Once the random grid of cut points is constructed, the optimal cut point can be chosen using any
 1884 number of metrics, such as signal to background ratio. For the purpose of the $W^\pm W^\pm jj$ upgrade

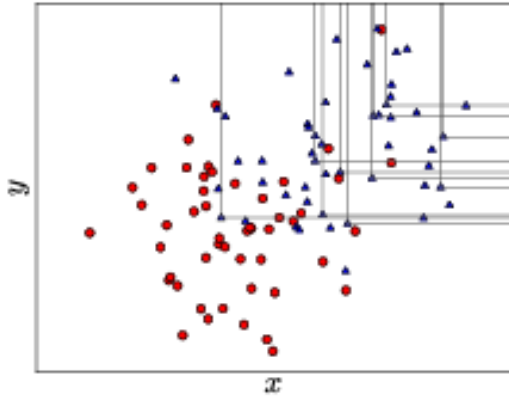


Figure 6.4: A visual representation of a random grid search algorithm. The signal events are the blue triangles, and the red circles are the background events. **TODO: replace with own figure**

1885 study, the optimal cut point is chosen to be the one that maximizes the signal significance Z as
 1886 defined in Equation 6.2 [86].

$$Z = \sqrt{2 \left[(s + b) \ln \left(\frac{s + b}{b_0} \right) + b_0 - s - b \right] + \frac{(b - b_0)^2}{\sigma_b^2}} \quad (6.2)$$

1887 where s and b are the number of signal and background events, respectively, σ_b is the total uncertainty
 1888 on the background, and b_0 is defined as:

$$b_0 = \frac{1}{2} \left(b - \sigma_b^2 + \sqrt{(b - \sigma_b^2)^2 + 4(s + b)\sigma_b^2} \right) \quad (6.3)$$

1889 In the case where the background is known precisely (i.e. $\sigma_b = 0$), Equation 6.2 simplifies to

$$Z = \sqrt{2 \left(b \left[(1 + s/b) \ln(1 + s/b) - s/b \right] \right)} \quad (6.4)$$

1890 which further reduces to the familiar $Z = s/\sqrt{b}$ for the case when $s \ll b$.

1891 6.5.2 Inputs to the optimization

1892 In order to train the RGS, signal and background samples are prepared from events passing the
 1893 event selection outlined in Table 6.3 up through the b -jet veto. The signal sample is chosen to be
 1894 the longitudinally polarized $W^\pm W^\pm jj$ EWK events, and the transverse and mixed polarizations
 1895 are treated as background along with $W^\pm W^\pm jj$ events from QCD interactions and the traditional
 1896 backgrounds listed in Section 6.3. Splitting the inclusive $W^\pm W^\pm jj$ EWK events by polarization

1897 allows the optimization to favor the longitudinally polarized events as much as possible, even though
 1898 they both contribute to the EWK signal.

1899 The following variables are chosen for optimization:

- 1900 • Leading lepton p_T
- 1901 • Dilepton invariant mass (m_{ll})
- 1902 • Leading and subleading jet p_T
- 1903 • Dijet invariant mass (m_{jj})
- 1904 • Lepton-jet centrality (ζ)

1905 Subleading lepton p_T is omitted as it is desirable to keep the cut value as low as possible due to
 1906 its sensitivity to the longitudinal polarization (as discussed in Section 6.1.1). Additionally, the dijet
 1907 separation $\Delta\eta_{jj}$ was included in the optimization originally, however it was dropped from the list due
 1908 to the cut value being motivated by differences between EWK and QCD produced $W^\pm W^\pm jj$ events.

1909 Two additional constraints were imposed when selecting the optimal cut point:

- 1910 1. At least 1000 signal events must survive in order to prevent the optimization from being too
 1911 aggressive and unnecessarily reducing signal statistics.
- 1912 2. The dijet invariant mass may only vary within a 50 GeV range of the default value (from
 1913 450 – 550 GeV) due to the cut being physically motivated by the VBS event topology (see
 1914 Section 5.0.3).

1915 Lastly, the signal significance is calculated without taking into account the uncertainty of the
 1916 background using Equation 6.4. This is due to the fact that the statistical uncertainties of the fake
 1917 electron and charge misidentification backgrounds are quite large, owing to poor MC statistics in a
 1918 few of the samples. If Equation 6.2 were used instead, the optimization will cut unreasonably hard
 1919 against these backgrounds. Since Monte Carlo statistics is not expected to be a limiting factor when
 1920 this analysis is performed at the HL-LHC, it is more realistic to simply ignore these large statistical
 1921 uncertainties for the purpose of the optimization.

1922 6.5.3 Results of the optimization

1923 Ultimately, the random grid is constructed from over 38,000 LL-polarized $W^\pm W^\pm jj$ events in the
 1924 six variables listed above. After applying the constraints, the optimal cut point reduces the total

background from 9900 to 2310 while reducing the signal from 3489 to 2958. This corresponds to an increase in signal significance from $Z = 33.26$ to $Z = 52.63$ as calculated by Equation 6.4. The updates to the event selection are listed in Table 6.4.

The large reduction in the background is primarily a result of the increase in the leading and subleading jet p_T from 30 GeV to 90 GeV and 45 GeV, respectively. As can be seen in Figure 6.7, this increase removes a significant portion of the backgrounds from jets faking electrons and charge mis-ID. Additionally, the loosening of the lepton-jet centrality cut ζ allows more signal events to survive the event selection (see Figure 6.9). Other changes to the event selection are minor and do not individually have a large impact on the signal or background yields.

The full event yields after optimization as well as the cross section measurement are detailed alongside those using the default selection in Section 6.6.

TODO: It's a bit awkward to reference the results of the default/optimized before they're properly presented. Maybe move the sections around? not sure...

Selection requirement	Selection value
Lepton kinematics	$p_T > 28$ GeV (leading lepton only)
Jet kinematics	$p_T > 90$ GeV (leading jet) $p_T > 45$ GeV (subleading jet)
Dilepton mass	$m_{ll} > 28$ GeV
Dijet mass	$m_{jj} > 520$ GeV
Lepton-jet centrality	$\zeta > -0.5$

Table 6.4: Updates to the $W^\pm W^\pm jj$ event selection criteria after optimization. Cuts not listed remain unchanged from the default selection in Table 6.3.

6.6 Results

6.6.1 Event yields

After applying the full event selection, the analysis is broken down into four channels based off of the flavor of the signal leptons: $\mu\mu$, ee , μe , and $e\mu$. The full signal and background event yields are shown in Table 6.5 for each channel separately and combined using the default event selection. 3489 EWK $W^\pm W^\pm jj$ events are expected compared to 9900 background events. The dominant sources of background are jets faking electrons followed by charge misidentification and diboson processes. Triboson events, QCD $W^\pm W^\pm jj$, and other non-prompt sources make up approximately 5% of the total background combined.

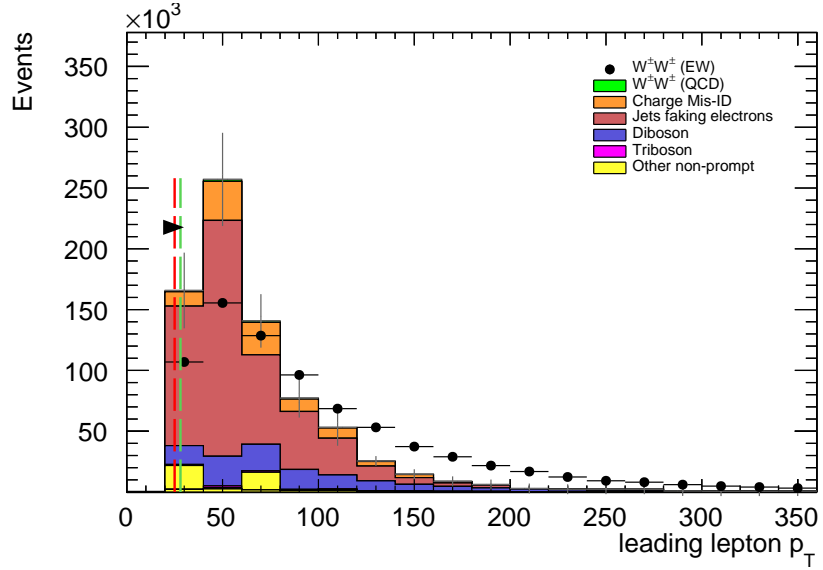


Figure 6.5: Leading lepton p_T distribution. The default and optimized cuts are represented by the red and green dashed lines, respectively. The $W^\pm W^\pm jj$ EWK signal (black points) is normalized to the same area as the sum of the backgrounds (colored histogram). **TODO: Move to appendix or omit**

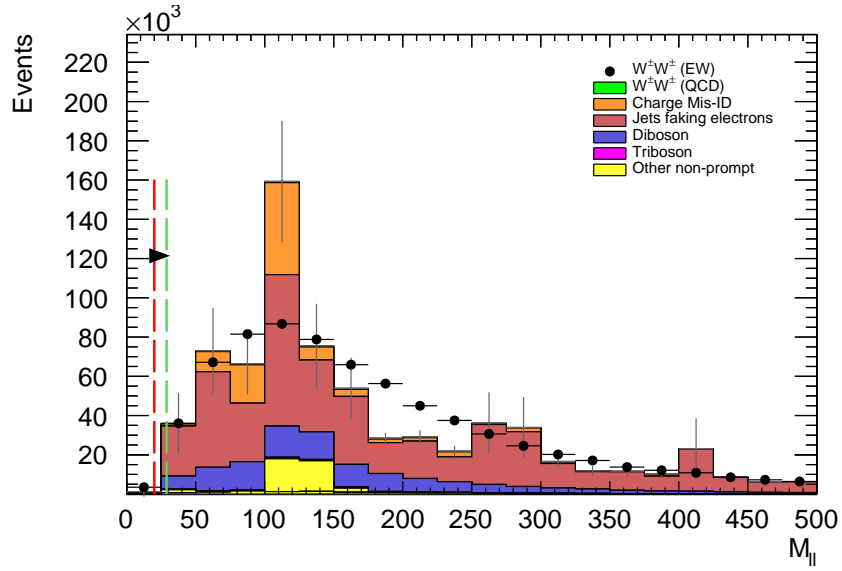


Figure 6.6: Dilepton invariant mass distribution. The default and optimized cuts are represented by the red and green dashed lines, respectively. The $W^\pm W^\pm jj$ EWK signal (black points) is normalized to the same area as the sum of the backgrounds (colored histogram). **TODO: Move to appendix or omit**

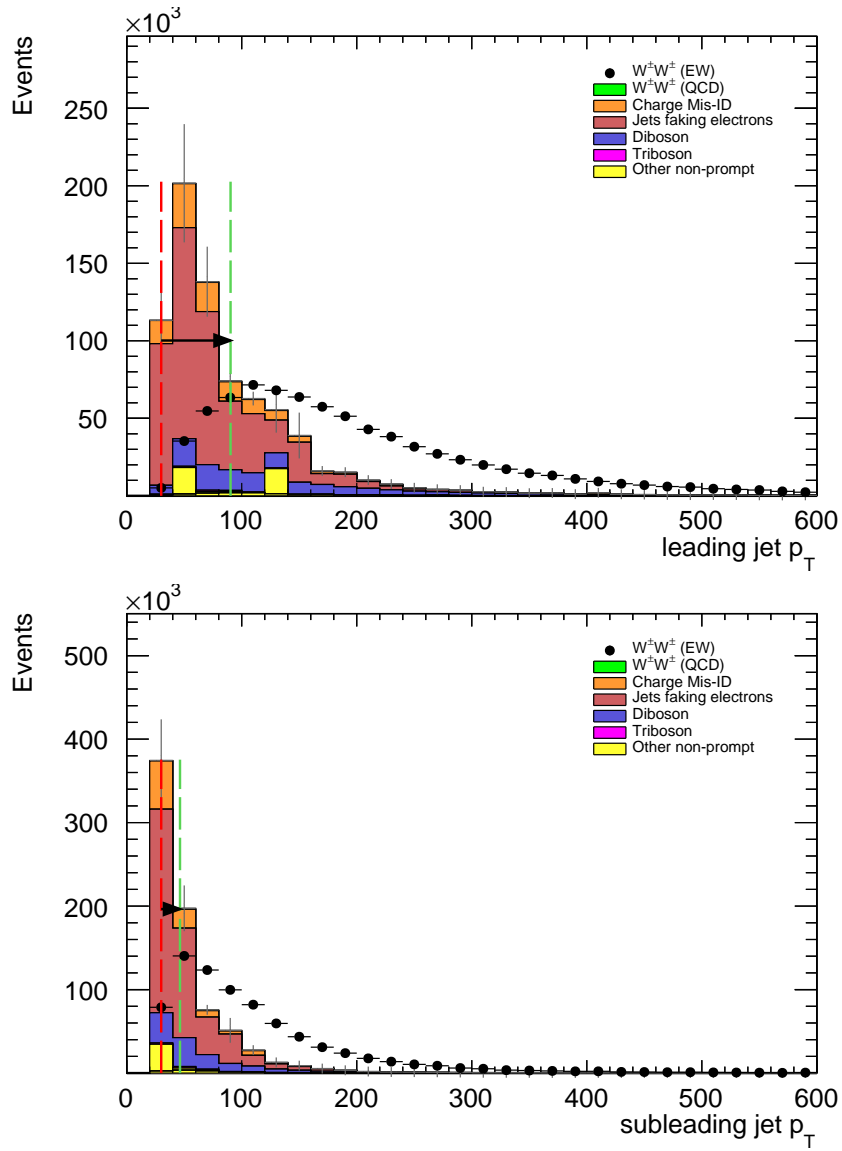


Figure 6.7: Leading (top) and subleading (bottom) jet p_T distributions. The default and optimized cuts are represented by the red and green dashed lines, respectively. The $W^\pm W^\pm jj$ EWK signal (black points) is normalized to the same area as the sum of the backgrounds (colored histogram).

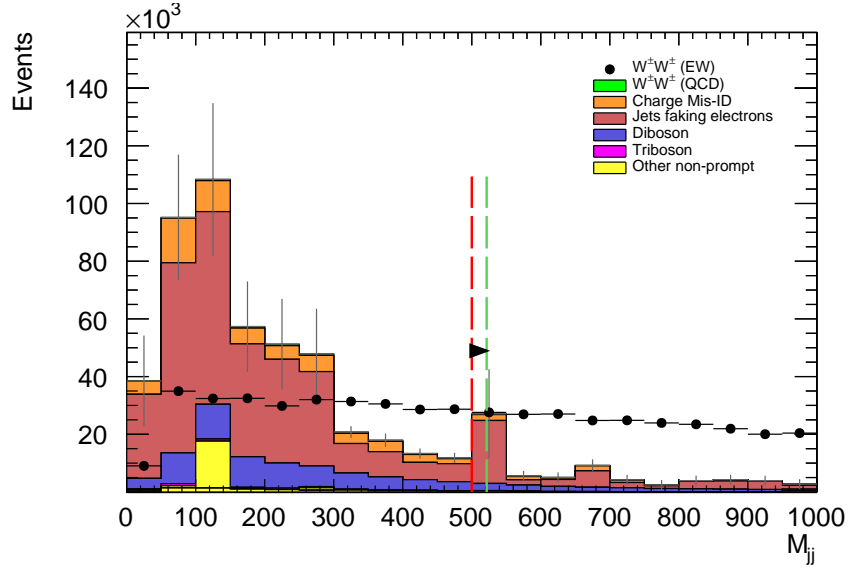


Figure 6.8: Dijet invariant mass distribution. The default and optimized cuts are represented by the red and green dashed lines, respectively. The $W^\pm W^\pm jj$ EWK signal (black points) is normalized to the same area as the sum of the backgrounds (colored histogram). **TODO:** Move to appendix or omit

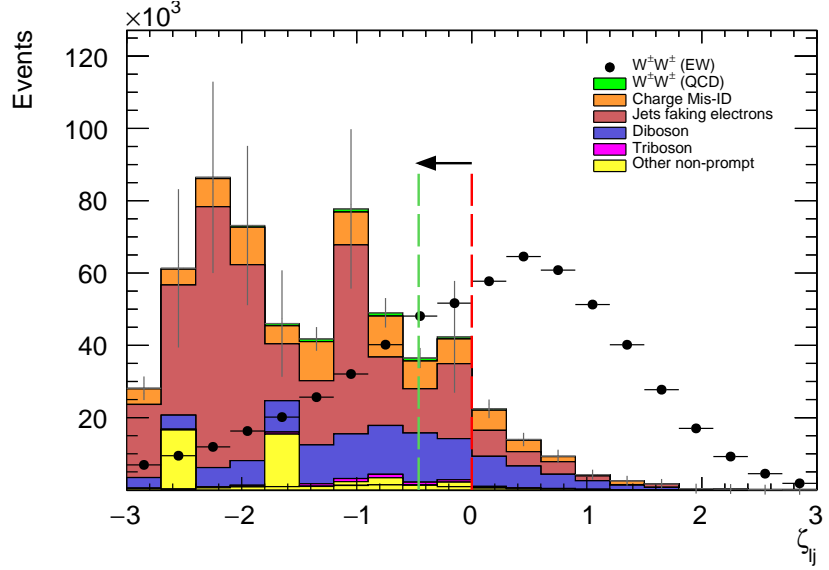


Figure 6.9: Lepton-jet centrality distribution. The default and optimized cuts are represented by the red and green dashed lines, respectively. The $W^\pm W^\pm jj$ EWK signal (black points) is normalized to the same area as the sum of the backgrounds (colored histogram).

	All channels	$\mu\mu$	ee	μe	$e\mu$
$W^\pm W^\pm jj$ (QCD)	206.4	91.1	22.8	38.4	54.1
Charge Misidentification	2300	0.0	2100	90	160
Jets faking electrons	5000	0.0	3400	1200	340
$WZ + ZZ$	2040	500	438	423	680
Tribosons	115	47	15.4	21.6	31.2
Other non-prompt	210	110	20	60	27
Total Background	9900	750	6000	1900	1290
Signal $W^\pm W^\pm jj$ (EWK)	3489	1435	432	679	944

Table 6.5: Signal and background event yields using the default event selection for an integrated luminosity of $\mathcal{L} = 3000 \text{ fb}^{-1}$. Events containing a fake or charge-flipped electron are removed from their respective sources and combined into a single entry each.

1947 The event yields for the optimized selection detailed in Section 6.5.3 are listed in Table 6.6. After
 1948 optimization, 2958 signal events and just 2310 background events are expected. Diboson events are
 1949 now the primary source of background, as the optimization greatly reduces the fake and charge
 1950 misidentification backgrounds. As discussed earlier, the increase in the leading and subleading jet
 1951 p_T cuts as well as the loosening of the centrality cut are most responsible for the changes in the
 1952 signal and background yields; distributions of these quantities using the default and the optimized
 1953 event selections can be found in Figures 6.10, 6.11, and 6.12, respectively.

	All channels	$\mu\mu$	ee	μe	$e\mu$
$W^\pm W^\pm jj$ (QCD)	168.7	74.6	19.7	32.2	42.2
Charge Misidentification	200	0.0	11	30	160
Jets faking electrons	460	0.0	130	260	70
$WZ + ZZ$	1286	322	289	271	404
Tribosons	76	30.1	9.6	15.1	21.6
Other non-prompt	120	29	16.6	50	19
Total Background	2310	455	480	660	710
Signal $W^\pm W^\pm jj$ (EWK)	2958	1228	380	589	761

Table 6.6: Signal and background event yields using the optimized event selection for an integrated luminosity of $\mathcal{L} = 3000 \text{ fb}^{-1}$. Events containing a fake or charge-flipped electron are removed from their respective sources and combined into a single entry each.

1954 It is important to note, however, that the MC sample used to estimate $Z + \text{jets}$ events suffers from
 1955 poor statistics which results in large per-event weights once scaled to $\mathcal{L} = 3000 \text{ fb}^{-1}$. This sample
 1956 contributes heavily to the fake and charge misidentification backgrounds, and a handful of these
 1957 events being cut out by the optimization contributes has a large effect on the dramatic reduction
 1958 of these backgrounds. As a result, these particular optimized results are likely overly optimistic.
 1959 However, given proper MC statistics, it is still expected that the optimization will outperform the

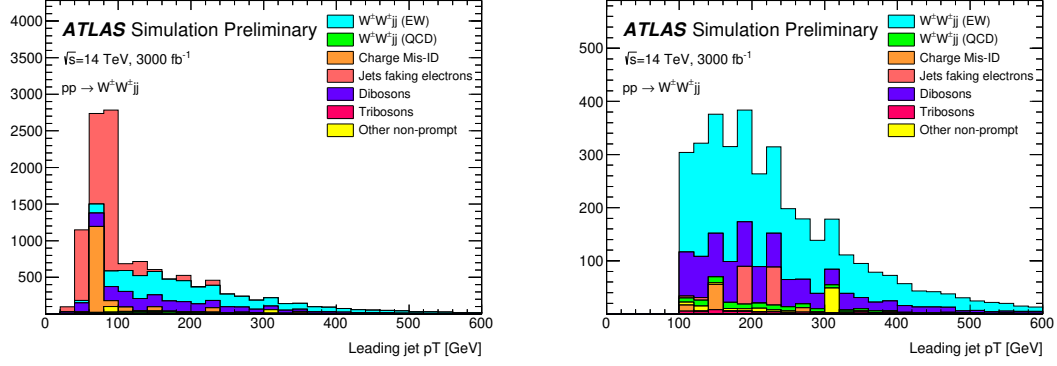


Figure 6.10: p_T distributions for the leading jet using the default (left) and optimized (right) event selections for all channels combined.

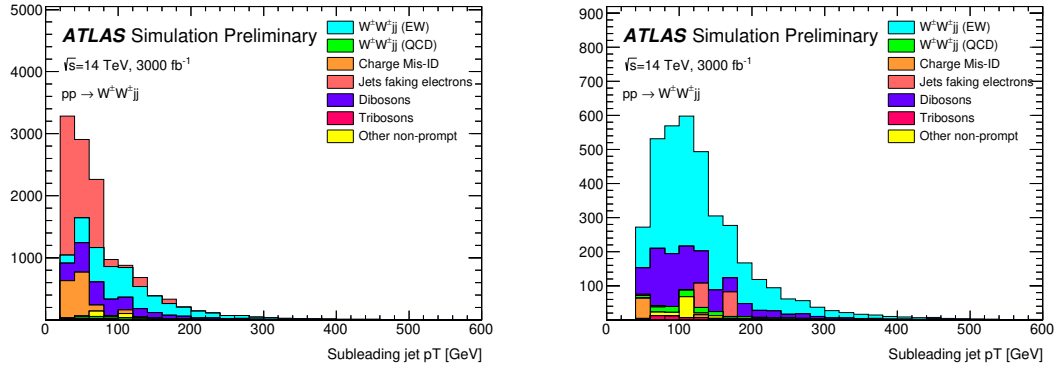


Figure 6.11: p_T distributions for the subleading jet using the default (left) and optimized (right) event selections for all channels combined.

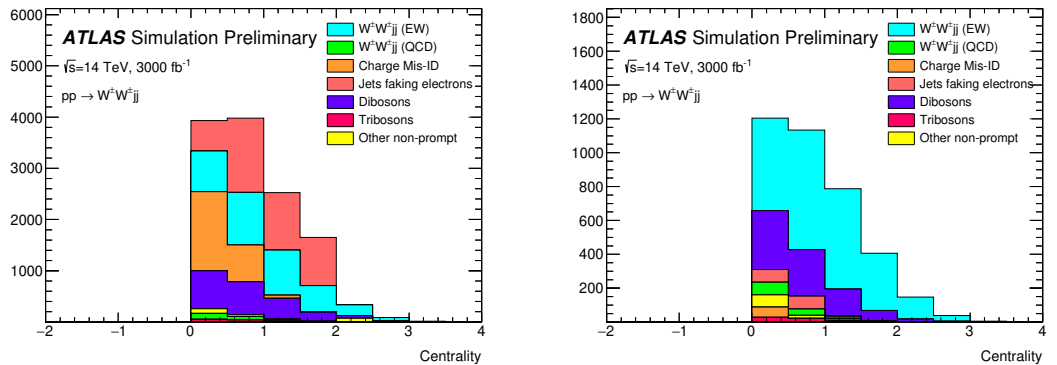


Figure 6.12: p_T distributions for lepton-jet centrality ζ using the default (left) and optimized (right) event selections for all channels combined.

1960 default selection.

1961 6.6.2 Uncertainties

1962 **TODO:** Ask for details on how some of these uncertainties were calculated – specifically the fakes and
 1963 charge mis-ID The uncertainties considered for the analysis are summarized in Table 6.7. Values for
 1964 experimental systematics on the trigger efficiency, lepton and jet reconstruction, and flavor tagging
 1965 are taken directly from the 13 TeV analysis [38]. The rate uncertainties for the background processes
 1966 are halved from the 13 TeV values.

Source	Uncertainty (%)
$W^\pm W^\pm jj$ (EWK)	3
Luminosity	1
Trigger efficiency	0.5
Lepton reconstruction and identification	1.8
Jets	2.3
Flavor tagging	1.8
Jets faking electrons	20
Charge misidentification	25
$W^\pm W^\pm jj$ (QCD)	20
Top	15
Diboson	10
Triboson	15

Table 6.7: Summary of estimated experimental and rate uncertainties.

1967 6.6.3 Cross section measurement

1968 The cross section is calculated using the same method as in the 13 TeV analysis, detailed in Chap-
 1969 ter 5. **TODO: update from chapter reference to subsection reference (once it's written)...** Once
 1970 again, each of the four lepton flavor channels is further split by charge (i.e. $\mu\mu \rightarrow \mu^+\mu^+ + \mu^-\mu^-$),
 1971 as this increases the sensitivity of the analysis. Each channel's m_{jj} distribution is combined in a
 1972 profile likelihood fit to extract the EWK $W^\pm W^\pm jj$ production cross section. The expected cross
 1973 section calculated using the default event selection is:

$$\sigma_{W^\pm W^\pm jj}^{\text{expected}} = 16.89 \pm 0.36 \text{ (stat)} \pm 0.53 \text{ (theory)} \pm 0.84 \text{ (syst)} \text{ fb} \quad (6.5)$$

1974 The expected cross section calculated using the optimized event selection is:

$$\sigma_{W^\pm W^\pm jj}^{\text{expected}} = 16.94 \pm 0.36 \text{ (stat)} \pm 0.53 \text{ (theory)} \pm 0.78 \text{ (syst)} \text{ fb} \quad (6.6)$$

1975 The optimized selection should not change the measured value of the cross section, and indeed both
 1976 are consistent with within uncertainties. The systematic uncertainty is reduced by approximately 7%
 1977 with the optimized selection. Projections of the total uncertainty on the cross section as a function
 1978 of integrated luminosity made by [TODO: how was this made?](#) is shown in Figure 6.13. As the
 1979 integrated luminosity increases past $\mathcal{L} > 3000 \text{ fb}^{-1}$, the statistical uncertainty reduces faster than
 1980 the systematic uncertainties. However, the total uncertainty is expected to reduce by less than a
 1981 percent with increased luminosity past the planned 3000 fb^{-1} .

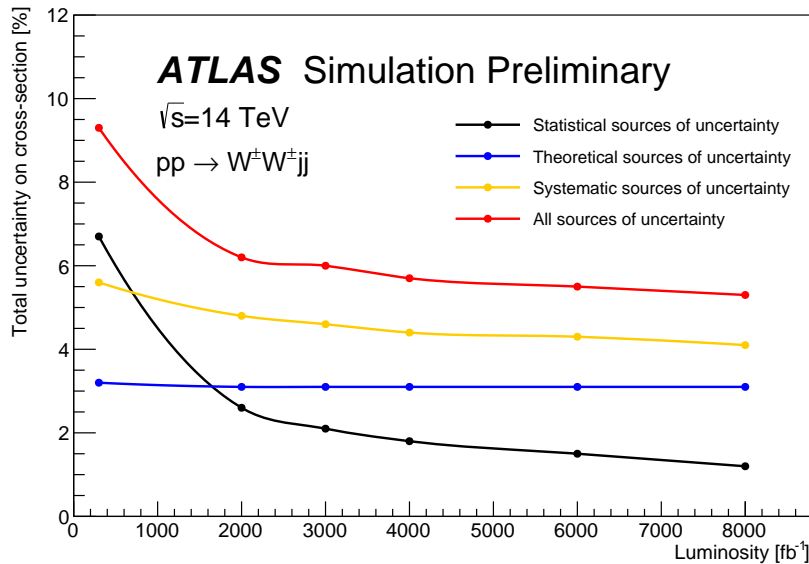


Figure 6.13: Projections of the statistical (black), theoretical (blue), systematic (yellow), and total (red) uncertainties on the measured cross section as a function of integrated luminosity using the optimized event selection.

1982 6.6.4 Longitudinal scattering significance

1983 [TODO: get some details on how this was all done...](#) The longitudinal scattering significance is
 1984 extracted from the $|\Delta\phi_{jj}|$ distribution using a simultaneous binned likelihood fit. In order to increase
 1985 sensitivity, the $|\Delta\phi_{jj}|$ distribution was split into two bins in m_{jj} , and an additional cut on the
 1986 pseudorapidity of the subleading lepton was applied ($|\eta| < 2.5$) to reduce background from fake and
 1987 charge misidentification. The $|\Delta\phi_{jj}|$ distributions used in the fit are shown in Figure 6.14. Due to
 1988 limited statistics, the four lepton flavor channels were not split by charge. The expected significance

¹⁹⁸⁹ of the $W_L^\pm W_L^\pm jj$ process is 1.8σ with a precision of 47% on the measurement. Projections of the
¹⁹⁹⁰ expected significance as a function of integrated luminosity is shown in Figure 6.15.

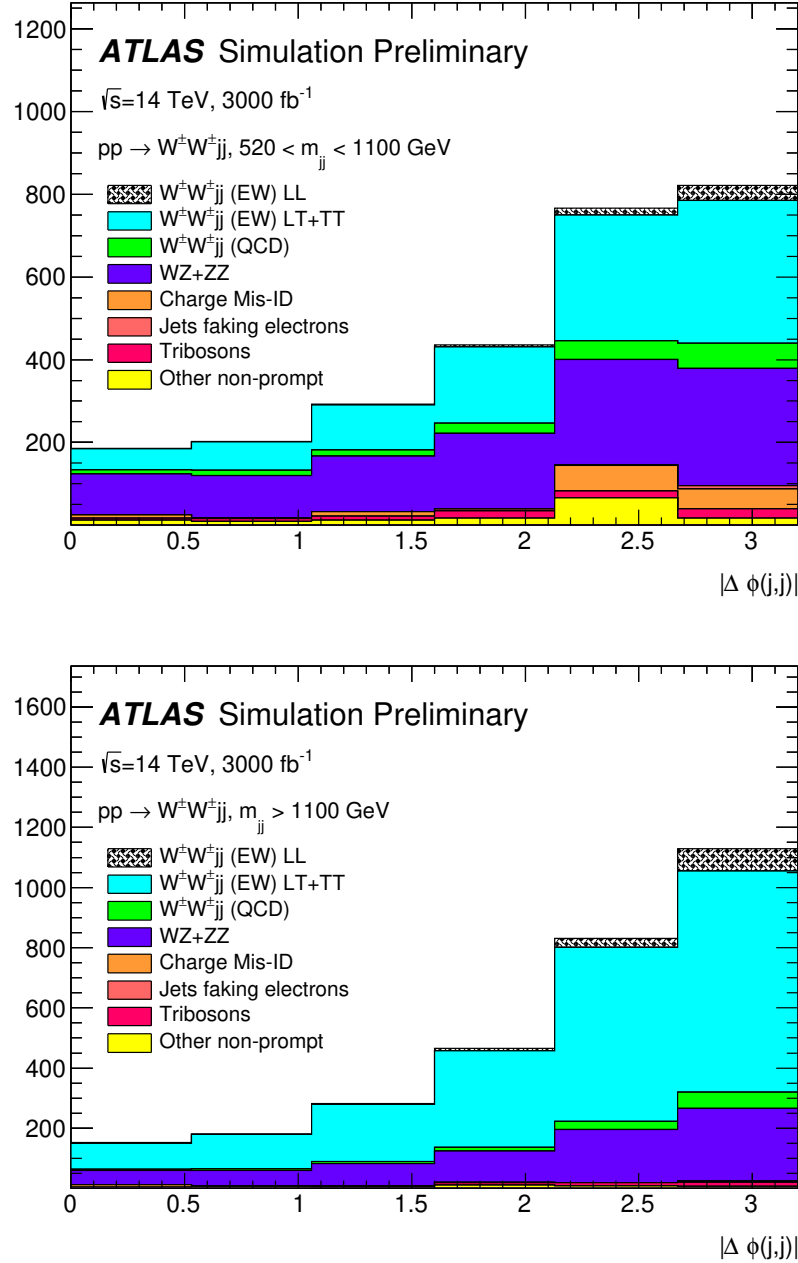


Figure 6.14: Dijet azimuthal separation ($|\Delta\phi_{jj}|$) for the low m_{jj} region ($520 < m_{jj} < 1100 \text{ GeV}$, top) and the high m_{jj} region ($m_{jj} > 1100 \text{ GeV}$, bottom). The purely longitudinal (LL, gray) is plotted separately from the mixed and transverse (LT+TT, cyan) polarizations.

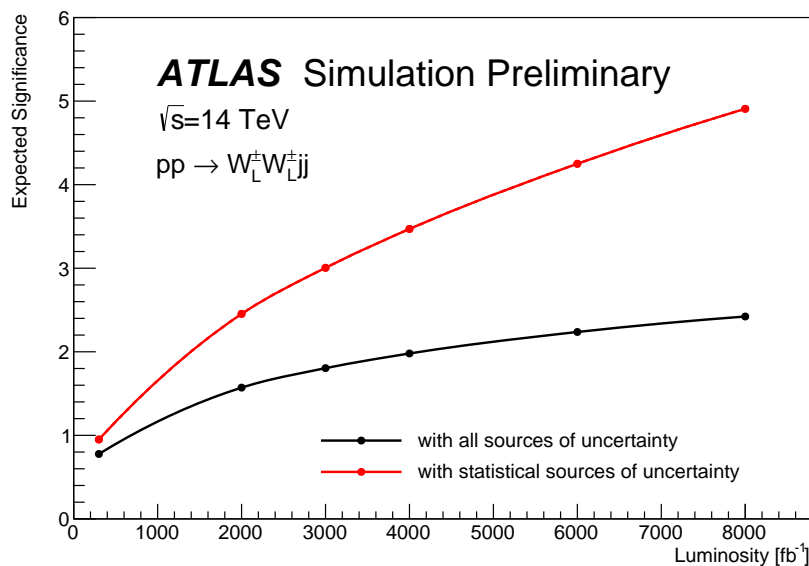


Figure 6.15: Projections of the expected longitudinal scattering significance as a function of integrated luminosity when considering all sources of uncertainties (black) or only statistical uncertainties (red).

1991

CHAPTER 7

1992

Conclusion

1993 Here's where you wrap it up.

1994 **Looking Ahead**

1995

1996 Here's an example of how to have an "informal subsection".

APPENDIX A

Additional material on truth isolation

yields by type	all channels	$\mu\mu$	ee	μe	$e\mu$
signal	4011	1583.2	531.7	793.1	1103.1
ww qcd	252.6	105.8	30.4	48	68.4
charge flip	2528.4	0.0	2075.4	255.1	197.8
fakes	7135.4	0.0	4675.1	1904.3	555.9
diboson	2370.4	581.2	491.8	517.9	779.6
triboson	125.5	49.1	17.8	24.6	34.1
top	90150.5	26618	15301.6	25277.9	22953.1
z+jets	241.2	0.0	0.0	0.0	241.2
w+jets	31.4	3.9	7.6	13.2	6.7
total bkg	102803.9	27354	22592	28027.8	24830.1
signal	4011	1583.2	531.7	793.1	1103.1

Table A.1: Event yields prior to applying any form of truth-based isolation criteria.

yields by type	all channels	$\mu\mu$	ee	μe	$e\mu$
signal	3470.5	1427.3	428.8	675.8	938.7
ww qcd	205.8	90.8	22.7	38.3	54
charge flip	2398.3	0.0	2104.6	95.8	197.9
fakes	4309.7	0.0	3390.6	750.8	168.3
diboson	1552.4	311.3	355.6	346.8	538.7
triboson	115	46.8	15.4	21.6	31.2
top	156.9	42.3	14.8	76.6	23.3
z+jets	0.0	0.0	0.0	0.0	0.0
w+jets	0.3	0.0	0.0	0.3	0.0
total bkg	8738.1	491.3	5903.7	1329.8	1013.4
signal	3470.5	1427.3	428.8	675.8	938.7

Table A.2: Event yields after applying a test version of the truth-based isolation.

2000

APPENDIX B

2001

2002

Additional material on $W^\pm W^\pm jj$ measurement at $\sqrt{s} = 13$ TeV

2003 B.1 Impact of experimental uncertainty on MC background estimations

$W^\pm W^\pm jj$ QCD	ee % Yield	$e\mu$ % Yield	$\mu\mu$ % Yield
Jet-related Uncertainties	3.41	3.04	2.85
b-tagging efficiency	2.56	2.48	2.48
Pile-up	4.99	0.45	0.33
Trigger efficiency	0.02	0.08	0.41
Lepton reconstruction/ID	1.62	1.19	1.89
MET reconstruction	0.41	0.22	0.34

Table B.1: Experimental systematics uncertainties for the $W^\pm W^\pm jj$ QCD processes in all channels.

Triboson	ee % Yield	$e\mu$ % Yield	$\mu\mu$ % Yield
Jet-related Uncertainties	13.09	13.39	16.85
b-tagging efficiency	2.96	3.77	4.95
Pile-up	19.37	24.66	6.87
Trigger efficiency	0.02	0.07	0.47
Lepton reconstruction/ID	1.66	1.27	2.48
MET reconstruction	0.00	0.46	0.00

Table B.2: Experimental systematics uncertainties for triboson process in all channels.

2004

plots go here

$t\bar{t}V$	ee % Yield	$e\mu$ % Yield	$\mu\mu$ % Yield
Jet-related Uncertainties	17.65	11.97	14.27
b-tagging efficiency	15.02	9.04	13.83
Pile-up	8.73	10.69	4.18
Trigger efficiency	0.03	0.08	0.39
Lepton reconstruction/ID	2.57	3.27	2.66
MET reconstruction	1.75	4.16	1.62

Table B.3: Experimental systematics uncertainties for $t\bar{t}V$ processes in all channels.

$W\gamma$	ee % Yield	$e\mu$ % Yield	$\mu\mu$ % Yield
Jet-related Uncertainties	7.05	33.36	—
b-tagging efficiency	1.97	2.94	—
Pile-up	4.11	14.17	—
Trigger efficiency	0.01	0.14	—
Lepton reconstruction/ID	1.40	1.13	—
MET reconstruction	0.00	0.00	—

Table B.4: Experimental systematics uncertainties for the $W\gamma$ process in all channels.

$Z\gamma$	ee % Yield	$e\mu$ % Yield	$\mu\mu$ % Yield
Jet-related Uncertainties	16.22	370.44	—
b-tagging efficiency	1.08	3.10	—
Pile-up	12.57	11.51	—
Trigger efficiency	0.02	0.07	—
Lepton reconstruction/ID	1.26	22.01	—
MET reconstruction	0.00	0.00	—

Table B.5: Experimental systematics uncertainties for the $Z\gamma$ process in all channels.

ZZ	ee % Yield	$e\mu$ % Yield	$\mu\mu$ % Yield
Jet-related Uncertainties	15.71	15.76	35.18
b-tagging efficiency	2.23	2.35	2.89
Pile-up	1.22	3.20	4.58
Trigger efficiency	0.03	0.10	0.36
Lepton reconstruction/ID	3.59	3.10	5.70
MET reconstruction	4.84	3.26	3.24

Table B.6: Experimental systematics uncertainties for the ZZ process in all channels.

Bibliography

- 2006 [1] S. Weinberg, *The Quantum Theory of Fields, Volume 1: Foundations*. Cambridge University Press, 1995. [2.1](#)
- 2007 [2] M. E. Peskin and D. V. Schroeder, *An Introduction to Quantum Field Theory*. Addison-Wesley, 1995. [2.1](#)
- 2008 [3] R. P. Feynman, *Mathematical formulation of the quantum theory of electromagnetic interaction*, *Phys. Rev.* **80** (1950) 440–457. [2.1](#)
- 2009 [4] M. Y. Han and Y. Nambu, *Three-triplet model with double SU(3) symmetry*, *Phys. Rev.* **139** (1965) B1006–B1010. [2.1](#)
- 2010 [5] D. J. Gross and F. Wilczek, *Asymptotically Free Gauge Theories - I*, *Phys. Rev.* **D8** (1973) 3633–3652. [2.1](#)
- 2011 [6] D. J. Gross and F. Wilczek, *ASYMPTOTICALLY FREE GAUGE THEORIES. 2.*, *Phys. Rev.* **D9** (1974) 980–993. [2.1](#)
- 2012 [7] H. D. Politzer, *Reliable Perturbative Results for Strong Interactions?*, *Phys. Rev. Lett.* **30** (1973) 1346–1349. [[274\(1973\)](#)]. [2.1](#)
- 2013 [8] A. Salam and J. C. Ward, *Weak and Electromagnetic Interactions*, *Nuovo Cimento* **11** (1959) 568–577. [2.1](#)
- 2014 [9] S. L. Glashow, *The Renormalizability of Vector Meson Interactions*, *Nucl. Phys.* **10** (1959) 107–117. [2.1](#)
- 2015 [10] ALEPH, DELPHI, L3, OPAL, SLD, LEP Electroweak Working Group, SLD Electroweak Group, SLD Heavy Flavour Group Collaboration, S. Schael et al., *Precision electroweak measurements on the Z resonance*, *Phys. Rept.* **427** (2006) 257–454, [arXiv:hep-ex/0509008 \[hep-ex\]](#). [2.1](#)
- 2016 [11] F. Englert and R. Brout, *Broken symmetry and the mass of gauge vector mesons*, *Phys. Rev. Lett.* **13** (1964) 321–323. [2.1](#)
- 2017 [12] P. W. Higgs, *Broken symmetries, massless particles and gauge fields*, *Physics Letters* **12** (1964) 132–133. [2.1](#)

- 2032 [13] P. W. Higgs, *Broken symmetries and the masses of gauge bosons*, Phys. Rev. Lett. **13** (1964)
2033 508–509. 2.1
- 2034 [14] UA1 Collaboration, G. Arnison et al., *Experimental Observation of Isolated Large Transverse
2035 Energy Electrons with Associated Missing Energy at $s^{**}(1/2) = 540\text{-GeV}$* , Phys. Lett. **B122**
2036 (1983) 103–116. [,611(1983)]. 2.2
- 2037 [15] UA1 Collaboration, G. Arnison et al., *Experimental Observation of Lepton Pairs of Invariant
2038 Mass Around $95\text{-GeV}/c^{**2}$ at the CERN SPS Collider*, Phys. Lett. **B126** (1983) 398–410.
2039 [,7.55(1983)]. 2.2
- 2040 [16] Particle Data Group Collaboration, K. A. Olive et al., *Review of Particle Physics*, Chin.
2041 Phys. **C38** (2014) 090001. 2.2, 2.2
- 2042 [17] L. R. Evans and P. Bryant, *LHC Machine*, JINST **3** (2008) S08001.
2043 <https://cds.cern.ch/record/1129806>. This report is an abridged version of the LHC
2044 Design Report (CERN-2004-003). 3.1
- 2045 [18] ATLAS Collaboration, *The ATLAS Experiment at the CERN Large Hadron Collider*, JINST
2046 **3** (2008) S08003. 3.1
- 2047 [19] ATLAS Collaboration, *ATLAS inner detector: Technical Design Report, Vol. 1*. CERN,
2048 Geneva, 1997. <https://cds.cern.ch/record/331063>. 4
- 2049 [20] P. F. Åkesson, T. Atkinson, M. J. Costa, M. Elsing, S. Fleischmann, A. N. Gaponenko,
2050 W. Liebig, E. Moyse, A. Salzburger, and M. Siebel, *ATLAS Tracking Event Data Model*,
2051 Tech. Rep. ATL-SOFT-PUB-2006-004. ATL-COM-SOFT-2006-005.
2052 CERN-ATL-COM-SOFT-2006-005, CERN, Geneva, Jul, 2006.
2053 <https://cds.cern.ch/record/973401>. 4.1
- 2054 [21] P. Brückman, A. Hicheur, and S. J. Haywood, *Global chi2 approach to the Alignment of the
2055 ATLAS Silicon Tracking Detectors*, Tech. Rep. ATL-INDET-PUB-2005-002.
2056 ATL-COM-INDET-2005-004. CERN-ATL-INDET-PUB-2005-002, CERN, Geneva, 2005.
2057 <https://cds.cern.ch/record/835270>. 4.1, 4.1
- 2058 [22] ATLAS Collaboration Collaboration, *Alignment of the ATLAS Inner Detector Tracking
2059 System with 2010 LHC proton-proton collisions at $\sqrt{s} = 7\text{ TeV}$* , Tech. Rep.
2060 ATLAS-CONF-2011-012, CERN, Geneva, Mar, 2011.
2061 <https://cds.cern.ch/record/1334582>. 4.1, 4.2.3, 4.14
- 2062 [23] R. Härtel and S. Bethke, *Iterative local Chi2 alignment approach for the ATLAS SCT
2063 detector*, Nov, 2005. <http://cds.cern.ch/record/1511044>. Presented 28 Nov 2005. 4.1
- 2064 [24] ATLAS Collaboration Collaboration, P. Brückman de Renstrom, *Alignment strategy for the
2065 Inner Detector of ATLAS*, . <https://cds.cern.ch/record/1047114>. 4.1
- 2066 [25] *Alignment of the ATLAS Inner Detector and its Performance in 2012*, Tech. Rep.
2067 ATLAS-CONF-2014-047, CERN, Geneva, Jul, 2014.
2068 <https://cds.cern.ch/record/1741021>. 4.1, 4.2.1, 4.4
- 2069 [26] J. J. Peña, *Alignment of the ATLAS Inner Detector Upgraded for the LHC Run II*, J. Phys.
2070 Conf. Ser. **664** (2015) no. 7, 072025. 4.1

- 2071 [27] J. Alison and I. J. Kroll, *The Road to Discovery: Detector Alignment, Electron Identification,*
2072 *Particle Misidentification, WW Physics, and the Discovery of the Higgs Boson*, Dec, 2015.
2073 <https://cds.cern.ch/record/1536507>. Presented 08 Nov 2012. 5
- 2074 [28] *ATLAS Inner Detector Alignment Performance with February 2015 Cosmic Rays Data*, Tech.
2075 Rep. ATL-PHYS-PUB-2015-009, CERN, Geneva, Apr, 2015.
2076 <https://cds.cern.ch/record/2008724>. 4.3, 4.2
- 2077 [29] ATLAS Collaboration Collaboration, M. Capeans, G. Darbo, K. Einsweiller, M. Elsing,
2078 T. Flick, M. Garcia-Sciveres, C. Gemme, H. Pernegger, O. Rohne, and R. Vuillermet, *ATLAS*
2079 *Insertable B-Layer Technical Design Report*, Tech. Rep. CERN-LHCC-2010-013.
2080 ATLAS-TDR-19, Sep, 2010. <https://cds.cern.ch/record/1291633>. 4.2
- 2081 [30] *Alignment of the ATLAS Inner Detector with the initial LHC data at $\sqrt{s} = 13$ TeV*, Tech.
2082 Rep. ATL-PHYS-PUB-2015-031, CERN, Geneva, Jul, 2015.
2083 <https://cds.cern.ch/record/2038139>. 4.2
- 2084 [31] *Study of the mechanical stability of the ATLAS Insertable B-Layer*, Tech. Rep.
2085 ATL-INDET-PUB-2015-001, CERN, Geneva, Jun, 2015.
2086 <https://cds.cern.ch/record/2022587>. 4.2.1
- 2087 [32] *Common Framework Implementation for the Track-Based Alignment of the ATLAS Detector*,
2088 Tech. Rep. ATL-SOFT-PUB-2014-003, CERN, Geneva, Mar, 2014.
2089 <https://cds.cern.ch/record/1670354>. 4.2.1
- 2090 [33] ATLAS Collaboration Collaboration, *Study of alignment-related systematic effects on the*
2091 *ATLAS Inner Detector track reconstruction*, Tech. Rep. ATLAS-CONF-2012-141, CERN,
2092 Geneva, Oct, 2012. <https://cds.cern.ch/record/1483518>. 4.4, 4.4, 4.4.1.1, 4.4.1.2
- 2093 [34] S. Marti-Garcia, S. Camarda, T. Golling, M. Danninger, N. A. Styles, J. Wollrath, W. K.
2094 Di Clemente, S. Henkelmann, J. Jimenez Peña, O. Estrada Pastor, A. K. Morley, H. Oide,
2095 A. T. Vermeulen, P. Butti, E. Ricci, F. M. Follega, and R. Iuppa, *Studies of radial distortions*
2096 *of the ATLAS Inner Detector*, Tech. Rep. ATL-COM-INDET-2018-010, CERN, Geneva, Mar,
2097 2018. <https://cds.cern.ch/record/2306724>. 4.4
- 2098 [35] ATLAS Collaboration Collaboration, *Electron and photon energy calibration with the ATLAS*
2099 *detector using data collected in 2015 at $\sqrt{s} = 13$ TeV*, Tech. Rep. ATL-PHYS-PUB-2016-015,
2100 CERN, Geneva, Aug, 2016. <https://cds.cern.ch/record/2203514>. 4.4.1
- 2101 [36] ATLAS Collaboration, ATLAS Collaboration, *Evidence for Electroweak Production*
2102 *of $W^\pm W^\pm jj$ in pp Collisions at $\sqrt{s} = 8$ TeV with the ATLAS Detector*, Phys. Rev. Lett. **113**
2103 (2014) no. 14, 141803, arXiv:1405.6241 [hep-ex]. 5
- 2104 [37] CMS Collaboration, V. Khachatryan et al., *Study of vector boson scattering and search for*
2105 *new physics in events with two same-sign leptons and two jets*, Phys. Rev. Lett. **114** (2015)
2106 no. 5, 051801, arXiv:1410.6315 [hep-ex]. 5
- 2107 [38] ATLAS Collaboration Collaboration, *Observation of electroweak production of a same-sign W*
2108 *boson pair in association with two jets in pp collisions at $\sqrt{s} = 13$ TeV with the ATLAS*
2109 *detector*, Tech. Rep. ATLAS-CONF-2018-030, CERN, Geneva, Jul, 2018.
2110 <https://cds.cern.ch/record/2629411>. 5, 5.8, 6.6.2

- 2111 [39] CMS Collaboration, CMS Collaboration, *Observation of electroweak production of same-sign*
 2112 *W boson pairs in the two jet and two same-sign lepton final state in proton-proton collisions*
 2113 *at $\sqrt{s} = 13$ TeV*, arXiv:1709.05822 [hep-ex]. 5
- 2114 [40] C. Bittrich, W. K. Di Clemente, et al., *Support note for measurement of electroweak*
 2115 *$W^\pm W^\pm jj$ production at $\sqrt{s} = 13$ TeV*, Tech. Rep. ATL-COM-PHYS-2018-252, CERN,
 2116 Geneva, Mar, 2018. <https://cds.cern.ch/record/2309552>. 5, 5.3.3, 2, 4, 5.4.3
- 2117 [41] B. W. Lee, C. Quigg, and H. B. Thacker, *The Strength of Weak Interactions at Very*
 2118 *High-Energies and the Higgs Boson Mass*, Phys. Rev. Lett. **38** (1977) 883–885. 5.0.2
- 2119 [42] S. D. Rindani, *Strong gauge boson scattering at the LHC*, in *Physics at the Large Hadron*
 2120 *Collider*, A. Datta, B. Mukhopadhyaya, A. Raychaudhuri, A. K. Gupta, C. L. Khetrapal,
 2121 T. Padmanabhan, and M. Vijayan, eds., pp. 145–155. 2009. arXiv:0910.5068 [hep-ph]. 5.0.2
- 2122 [43] A. Alboteanu, W. Kilian, and J. Reuter, *Resonances and Unitarity in Weak Boson Scattering*
 2123 *at the LHC*, JHEP **11** (2008) 010, arXiv:0806.4145 [hep-ph]. 5.0.2, 5.1
- 2124 [44] ATLAS Collaboration, *Observation of a new particle in the search for the Standard Model*
 2125 *Higgs boson with the ATLAS detector at the LHC*, Phys. Lett. B **716** (2012) 1,
 2126 arXiv:1207.7214 [hep-ex]. 2.1, 5.0.2
- 2127 [45] CMS Collaboration, *Observation of a new boson at a mass of 125 GeV with the CMS*
 2128 *experiment at the LHC*, Phys. Lett. B **716** (2012) 30, arXiv:1207.7235 [hep-ex]. 2.1, 5.0.2
- 2129 [46] J. M. Campbell and R. K. Ellis, *Higgs Constraints from Vector Boson Fusion and Scattering*,
 2130 JHEP **04** (2015) 030, arXiv:1502.02990 [hep-ph]. 5.0.2, 5.0.3
- 2131 [47] M. Szleper, *The Higgs boson and the physics of WW scattering before and after Higgs*
 2132 *discovery*, arXiv:1412.8367 [hep-ph]. 5.0.2
- 2133 [48] E. Accomando, A. Ballestrero, A. Belhouari, and E. Maina, *Isolating Vector Boson Scattering*
 2134 *at the LHC: Gauge cancellations and the Equivalent Vector Boson Approximation vs complete*
 2135 *calculations*, Phys. Rev. **D74** (2006) 073010, arXiv:hep-ph/0608019 [hep-ph]. 5.0.2
- 2136 [49] P. Anger, B. Axen, et al., *Same Sign $W^\pm W^\pm$ Production and Limits on Anomalous Quartic*
 2137 *Gauge Couplings*, Tech. Rep. ATL-COM-PHYS-2013-990, CERN, Geneva, Jul, 2013.
 2138 <https://cds.cern.ch/record/1561731>. Internal note for approved paper STDM-2013-06.
 2139 5.0.3, 5.1, 5.7
- 2140 [50] J. Almond, L. Bianchini, et al., *Search for heavy neutrino, W_R and Z_R gauge bosons in events*
 2141 *with two high- P_T leptons and jets with the ATLAS detector in pp collisions at $\sqrt{s} = 8$ TeV*,
 2142 Tech. Rep. ATL-COM-PHYS-2013-810, CERN, Geneva, Jun, 2013.
 2143 <https://cds.cern.ch/record/1555805>. Supporting note for EXOT-2012-24, published as
 2144 JHEP07 (2015) 162. 5.0.4
- 2145 [51] ATLAS Collaboration, M. Aaboud et al., *Luminosity determination in pp collisions at $\sqrt{s} =$*
 2146 *8 TeV using the ATLAS detector at the LHC*, Eur. Phys. J. **C76** (2016) no. 12, 653,
 2147 arXiv:1608.03953 [hep-ex]. 5.1
- 2148 [52] G. Avoni et al., *The new LUCID-2 detector for luminosity measurement and monitoring in*
 2149 *ATLAS*, JINST **13** (2018) no. 07, P07017. 5.1

- 2150 [53] ATLAS Collaboration, G. Aad et al., *The ATLAS Simulation Infrastructure*, Eur. Phys. J. C70 (2010) 823–874, arXiv:1005.4568 [physics.ins-det]. 5.1.1
- 2151
- 2152 [54] S. Agostinelli et al., *GEANT4 - a simulation toolkit*, Nucl. Instrum. Meth. A506 (2003) 250–303. 5.1.1
- 2153
- 2154 [55] T. Sjostrand, S. Mrenna, and P. Skands, *A Brief Introduction to PYTHIA 8.1*, Comput. Phys. Commun. 178 (2008) 852–867, arXiv:0710.3820 [hep-ph]. 5.1.1
- 2155
- 2156 [56] T. Gleisberg et al., *Event generation with SHERPA 1.1*, JHEP 02 (2009) 007, arXiv:0811.4622 [hep-ph]. 5.1.1
- 2157
- 2158 [57] S. Schumann and F. Krauss, *A parton shower algorithm based on Catani-Seymour dipole factorization*, JHEP 03 (2008) 038, arXiv:0709.1027 [hep-ph]. 5.1.1
- 2159
- 2160 [58] S. Höche, F. Krauss, S. Schumann, and F. Siegert, *QCD matrix elements and truncated showers*, JHEP 05 (2009) 053, arXiv:0903.1219 [hep-ph]. 5.1.1
- 2161
- 2162 [59] R. D. Ball et al., *Parton distributions for the LHC Run II*, JHEP 04 (2015) 040, arXiv:1410.8849 [hep-ph]. 5.1.1
- 2163
- 2164 [60] S. Alioli, P. Nason, C. Oleari, and E. Re, *A general framework for implementing NLO calculations in shower Monte Carlo programs: the POWHEG BOX*, JHEP 06 (2010) 043, arXiv:1002.2581 [hep-ph]. 5.1.1
- 2165
- 2166
- 2167 [61] A. Ballestrero et al., *Precise predictions for same-sign W-boson scattering at the LHC*, Eur. Phys. J. C78 (2018) no. 8, 671, arXiv:1803.07943 [hep-ph]. 5.1.1
- 2168
- 2169 [62] J. Alwall, R. Frederix, S. Frixione, V. Hirschi, F. Maltoni, O. Mattelaer, H. S. Shao, T. Stelzer, P. Torrielli, and M. Zaro, *The automated computation of tree-level and next-to-leading order differential cross sections, and their matching to parton shower simulations*, JHEP 07 (2014) 079, arXiv:1405.0301 [hep-ph]. 5.1.1
- 2170
- 2171
- 2172
- 2173 [63] H.-L. Lai, M. Guzzi, J. Huston, Z. Li, P. M. Nadolsky, J. Pumplin, and C. P. Yuan, *New parton distributions for collider physics*, Phys. Rev. D 82 (2010) 074024, arXiv:1007.2241 [hep-ph]. 5.1.1
- 2174
- 2175
- 2176 [64] T. Sjostrand, S. Mrenna, and P. Skands, *PYTHIA 6.4 physics and manual*, JHEP 05 (2006) 026, arXiv:0603175 [hep-ph]. 5.1.1
- 2177
- 2178 [65] ATLAS Collaboration, G. Aad et al., *Muon reconstruction performance of the ATLAS detector in protonproton collision data at $\sqrt{s} = 13$ TeV*, Eur. Phys. J. C76 (2016) no. 5, 292, arXiv:1603.05598 [hep-ex]. 5.2.1.1, 11
- 2179
- 2180
- 2181 [66] ATLAS Collaboration Collaboration, *Electron efficiency measurements with the ATLAS detector using the 2015 LHC proton-proton collision data*, Tech. Rep. ATLAS-CONF-2016-024, CERN, Geneva, Jun, 2016.
- 2182
- 2183
- 2184 <https://cds.cern.ch/record/2157687>. 5.2.1.2
- 2185
- 2186 [67] M. Cacciari, G. P. Salam, G. Soyez, *The anti- k_t jet clustering algorithm*, JHEP 04 (2008) 063, arXiv:0802.1189 [hep-ph]. 5.2.1.3, 6.4.1
- 2187
- 2188 [68] ATLAS Collaboration, M. Aaboud et al., *Jet energy scale measurements and their systematic uncertainties in proton-proton collisions at $\sqrt{s} = 13$ TeV with the ATLAS detector*, Phys. Rev. D96 (2017) no. 7, 072002, arXiv:1703.09665 [hep-ex]. 5.2.1.3
- 2189

- 2190 [69] *Tagging and suppression of pileup jets with the ATLAS detector*, Tech. Rep.
 2191 ATLAS-CONF-2014-018, CERN, Geneva, May, 2014.
 2192 <http://cds.cern.ch/record/1700870>. 5.2.1.3
- 2193 [70] D. Adams, C. Anastopoulos, et al., *Recommendations of the Physics Objects and Analysis
 2194 Harmonisation Study Groups 2014*, Tech. Rep. ATL-PHYS-INT-2014-018, CERN, Geneva,
 2195 Jul, 2014. <https://cds.cern.ch/record/1743654>. 5.2.1.4
- 2196 [71] ATLAS Collaboration, M. Aaboud et al., *Measurement of the cross-section for producing a W
 2197 boson in association with a single top quark in pp collisions at $\sqrt{s} = 13$ TeV with ATLAS*,
 2198 *JHEP* **01** (2018) 063, arXiv:1612.07231 [hep-ex]. 5.2.1.4
- 2199 [72] ATLAS Collaboration, M. Aaboud et al., *Performance of missing transverse momentum
 2200 reconstruction with the ATLAS detector using proton-proton collisions at $\sqrt{s} = 13$ TeV*, *Eur.
 2201 Phys. J.* **C78** (2018) no. 11, 903, arXiv:1802.08168 [hep-ex]. 5.2.2
- 2202 [73] ATLAS Collaboration, M. Aaboud et al., *Measurements of b-jet tagging efficiency with the
 2203 ATLAS detector using $t\bar{t}$ events at $\sqrt{s} = 13$ TeV*, *JHEP* **08** (2018) 089, arXiv:1805.01845
 2204 [hep-ex]. 5.2.2
- 2205 [74] J.-F. Arguin, J. Claude, G. Gonella, B. P. Kersevan, K. Koneke, K. Lohwasser, K. Mochizuki,
 2206 M. Muskinja, C. Piaulet, and P. Sommer, *Support Note for Electron ID: charge
 2207 mis-identification*, Tech. Rep. ATL-COM-PHYS-2017-1014, CERN, Geneva, Jul, 2017.
 2208 <https://cds.cern.ch/record/2273365>. 5.3.3
- 2209 [75] C.-H. Kom and W. J. Stirling, *Charge asymmetry in $W + \text{jets}$ production at the LHC*, *Eur.
 2210 Phys. J.* **C69** (2010) 67–73, arXiv:1004.3404 [hep-ph]. 5.4
- 2211 [76] R. Steerenberg, *LHC Report: Another run is over and LS2 has just begun...*,
 2212 [https://home.cern/news/news/accelerators/
 2213 lhc-report-another-run-over-and-ls2-has-just-begun](https://home.cern/news/news/accelerators/lhc-report-another-run-over-and-ls2-has-just-begun), 2018. Accessed: 2018-12-14. 6
- 2214 [77] *Letter of Intent for the Phase-I Upgrade of the ATLAS Experiment*, Tech. Rep.
 2215 CERN-LHCC-2011-012. LHCC-I-020, CERN, Geneva, Nov, 2011.
 2216 <http://cds.cern.ch/record/1402470>. 6
- 2217 [78] G. Apollinari, I. Bjar Alonso, O. Brning, M. Lamont, and L. Rossi, *High-Luminosity Large
 2218 Hadron Collider (HL-LHC): Preliminary Design Report*. CERN Yellow Reports: Monographs.
 2219 CERN, Geneva, 2015. <https://cds.cern.ch/record/2116337>. 6
- 2220 [79] ATLAS Collaboration Collaboration, ATLAS Collaboration, *ATLAS Phase-II Upgrade
 2221 Scoping Document*, Cern-lhcc-2015-020, Geneva, Sep, 2015.
 2222 <http://cds.cern.ch/record/2055248>. 6
- 2223 [80] D. Espriu and B. Yencho, *Longitudinal WW scattering in light of the “Higgs boson”
 2224 discovery*, *Phys. Rev. D* **87** (2013) 055017, arXiv:1212.4158 [hep-ph]. 6, 6.1
- 2225 [81] ATLAS Collaboration Collaboration, *Prospects for the measurement of the $W^\pm W^\pm$ scattering
 2226 cross section and extraction of the longitudinal scattering component in pp collisions at the
 2227 High-Luminosity LHC with the ATLAS experiment*, Tech. Rep. ATL-PHYS-PUB-2018-052,
 2228 CERN, Geneva, Dec, 2018. <http://cds.cern.ch/record/2652447>. 6

- 2229 [82] ATLAS Collaboration Collaboration, *Studies on the impact of an extended Inner Detector*
2230 *tracker and a forward muon tagger on $W^\pm W^\pm$ scattering in pp collisions at the*
2231 *High-Luminosity LHC with the ATLAS experiment*, Tech. Rep. ATL-PHYS-PUB-2017-023,
2232 CERN, Geneva, Dec, 2017. <https://cds.cern.ch/record/2298958>. 6
- 2233 [83] T. Sjöstrand, S. Ask, J. R. Christiansen, R. Corke, N. Desai, P. Ilten, S. Mrenna, S. Prestel,
2234 C. O. Rasmussen, and P. Z. Skands, *An Introduction to PYTHIA 8.2*, *Comput. Phys.*
2235 *Commun.* **191** (2015) 159–177, [arXiv:1410.3012 \[hep-ph\]](https://arxiv.org/abs/1410.3012). 6.2
- 2236 [84] ATLAS Collaboration Collaboration, *Expected performance for an upgraded ATLAS detector*
2237 *at High-Luminosity LHC*, Tech. Rep. ATL-PHYS-PUB-2016-026, CERN, Geneva, Oct, 2016.
2238 [http://cds.cern.ch/record/2223839](https://cds.cern.ch/record/2223839). 6.3
- 2239 [85] P. C. Bhat, H. B. Prosper, S. Sekmen, and C. Stewart, *Optimizing Event Selection with the*
2240 *Random Grid Search*, *Comput. Phys. Commun.* **228** (2018) 245–257, [arXiv:1706.09907](https://arxiv.org/abs/1706.09907)
2241 *[hep-ph]*. 6.5.1
- 2242 [86] G. Cowan, K. Cranmer, E. Gross, and O. Vitells, *Asymptotic formulae for likelihood-based*
2243 *tests of new physics*, *Eur. Phys. J.* **C71** (2011) 1554, [arXiv:1007.1727 \[physics.data-an\]](https://arxiv.org/abs/1007.1727).
2244 [Erratum: *Eur. Phys. J.* C73,2501(2013)]. 6.5.1